



5-2007

Modeling Coordinate Measuring Machine Scanning Operations

Pamela Murray Moor
University of Tennessee - Knoxville

Follow this and additional works at: https://trace.tennessee.edu/utk_graddiss



Part of the [Mechanical Engineering Commons](#)

Recommended Citation

Moor, Pamela Murray, "Modeling Coordinate Measuring Machine Scanning Operations. " PhD diss., University of Tennessee, 2007.
https://trace.tennessee.edu/utk_graddiss/408

This Dissertation is brought to you for free and open access by the Graduate School at TRACE: Tennessee Research and Creative Exchange. It has been accepted for inclusion in Doctoral Dissertations by an authorized administrator of TRACE: Tennessee Research and Creative Exchange. For more information, please contact trace@utk.edu.

To the Graduate Council:

I am submitting herewith a dissertation written by Pamela Murray Moor entitled "Modeling Coordinate Measuring Machine Scanning Operations." I have examined the final electronic copy of this dissertation for form and content and recommend that it be accepted in partial fulfillment of the requirements for the degree of Doctor of Philosophy, with a major in Mechanical Engineering.

William R. Hamel, Major Professor

We have read this dissertation and recommend its acceptance:

Gary V. Smith, Jay Frankel, Lynne E. Parker

Accepted for the Council:

Carolyn R. Hodges

Vice Provost and Dean of the Graduate School

(Original signatures are on file with official student records.)

To the Graduate Council:

I am submitting herewith a dissertation written by Pamela Murray Moor entitled “Modeling Coordinate Measuring Machine Scanning Operations.” I have examined the final electronic copy of this dissertation for form and content and recommend that it be accepted in partial fulfillment of the requirements for the degree of Doctor of Philosophy, with a major in Mechanical Engineering.

William R. Hamel

Major Professor

We have read this dissertation
and recommend its acceptance:

Gary V. Smith

Jay Frankel

Lynne E. Parker

Acceptance for the Council:

Carolyn Hodges

Vice Provost and Dean of the Graduate School

(Original signatures are on file with official student records.)

MODELING
COORDINATE MEASURING MACHINE
SCANNING OPERATIONS

A Dissertation
Presented for the
Doctor of Philosophy
Degree
The University of Tennessee, Knoxville

Pamela Murray Moor
May 2007

Acknowledgments

I would like to thank Dr. Hamel for his guidance during my graduate studies. I would also like to thank my committee members for their suggestions on my research. Thanks to all my colleagues, especially Alan Smelcer, Bill Rasnick, and Bill Barkman, for their support of this work. I would like to thank my husband, Andrew Moor, for his insights on signal processing. Finally, I would like to thank my husband and my parents, Bill and Patricia Murray, for their love, support, and encouragement.

This material is based upon work supported under a National Science Foundation Graduate Research Fellowship. Any opinions, findings, conclusions or recommendations expressed in this publication are those of the author and do not necessarily reflect the views of the National Science Foundation.

Abstract

International standards require that dimensional inspection operations include an assessment of measurement uncertainty. Scanning coordinate measuring machines (CMMs) are frequently used to measure part surfaces and features, and there is a continuing need to improve their performance for high precision measurement applications. This research provides a mechanism for minimizing the uncertainty of measurements made with a CMM in scanning mode by developing a model of CMM scanning that allows selection of optimum scanning parameters.

The method for selecting scanning parameters is based on models developed from measurements of a ring with a constant five micrometer amplitude swept sine wave machined on the inner and outer diameters. The inputs to the model are the scanning force, scanning speed, low-pass filter cut-off frequency, rotary table action, probe tip diameter, and ring orientation. The methods used in this work are based on techniques developed for point-to-point probing. The first phase of research develops a calibration method for the ring artifact and determines the calibration measurement uncertainty. The second phase develops models of CMM scanning operations based on measurements of the wavy ring. The final phase generates a measurement protocol to select scanning parameters based on these models.

The primary significance of this research is that it provides a method to develop and validate a model of probe/workpiece interaction for a scanning CMM. Additionally, a method is provided to select the scanning parameters such as probe tip diameter, filters, scanning speed, and probing force to minimize measurement uncertainty. Finally, this work establishes a framework for future modeling of precision scanning operations. The methodology used is applicable to other precision metrology applications. This work will reduce uncertainty in scanning measurements and will minimize the number of measurement operations required to measure part features as well as surface texture. Therefore, this research has extended the capabilities of CMMs.

Table of Contents

1. Introduction.....	1
2. Literature Review.....	3
2.1. New CMM measurement uncertainty drivers.....	3
2.2. Sources of measurement uncertainty	4
2.3. Method of determining CMM measurement uncertainty	8
2.4. Existing methods of reducing CMM measurement uncertainty	11
2.4.1. Measuring environment	11
2.4.2. Software and calculations	14
2.4.3. CMM geometry.....	15
2.4.4. CMM probe.....	17
2.5. New method of reducing CMM measurement uncertainty.....	25
3. Calibration of the Wavy Ring Artifact.....	26
3.1. Description of artifact	26
3.2. Basis for calibration	28
3.3. Calibration development.....	29
3.3.1. Determination of measurand.....	29
3.3.2. Desired measurement uncertainty.....	32
3.3.3. Machine selection	33
3.3.4. Point spacing.....	35
3.4. Calibration procedure.....	39
3.4.1. Probe selection.....	40
3.4.2. Fixturing method.....	43
3.4.3. Calibration steps.....	43
3.5. Primary standard calibration results.....	49
4. Experimental Work.....	52
4.1. Experimental parameter selection.....	52
4.1.1. Probe tip diameter	52
4.1.2. Rotary table.....	53
4.1.3. Probing force.....	55
4.1.4. Artifact orientation.....	56
4.1.5. Environmental parameters	57
4.1.6. Scanning speed.....	61
4.1.7. Filter characteristics.....	61
4.2. Experimental setup.....	62
4.3. Experimental Procedure.....	65
4.3.1. Setup procedure	66
4.3.2. Measurement procedure.....	68
4.4. Experimental results.....	68
4.5. Experimental data analysis	69
4.5.1. Scanning speed effects.....	69
4.5.2. Filtering effects.....	77

5. Modeling	80
5.1. Modeling of filtering effects	81
5.1.1. Desired filter parameters to derive.....	81
5.1.2. Mathematical methodology for filter modeling.....	82
5.1.3. Theoretical filter modeling results	85
5.1.4. Digital filter modeling results	88
5.1.5. Use of models to select filter	94
5.2. Modeling of Scanning Speed Effects.....	96
5.2.1. Modeling objectives.....	96
5.2.2. Modeling the combined effects of scanning speed and probe head natural frequency	98
5.2.3. Modeling the effect of scanning speed on measurement uncertainty	101
5.2.4. Use of models to select scanning speed.....	112
5.3. Experimental plan for scanning parameter selection	113
6. Contributions and Future Work	114
6.1. Contributions.....	114
6.2. Future work.....	116
List of References	118
Appendices.....	124
Vita.....	165

List of Tables

3.1	Hours required for calibration as a function of points per wave.....	38
3.2	Components of ring uncertainty statement	50
4.1	Range of frequencies based on scanning speed and wavelength.....	62
4.2	Speeds and filter cut-off frequencies tested.....	65
5.1	Digital filter coefficients.....	93
5.2	Data transformations to unify reference data.....	103

List of Figures

3.1	Wavy ring artifact	26
3.2	Swept sine wave.....	27
3.3	Toleranced drawing of measurand.....	31
3.4	Machines considered for calibration.....	34
3.5	Moore M-48 at NIST	35
3.6	Constant number of calibration points per wavelength	36
3.7	Probe configuration.....	41
3.8	Radius of curvature.....	42
3.9	Probe calibration.....	44
3.10	Ring fixturing.....	45
3.11	Ring orientation and fixture post locations.....	46
3.12	Manual set-up probing point to determine center of ring	47
3.13	Manual set-up probing points to determine angular reference location	47
3.14	NIST calibration data.....	49
3.15	Uncertainty region for a probed point.....	51
4.1	Probe used in experimentation.....	53
4.2	Rotary table.....	54
4.3	Probe head natural frequency in x-direction.....	59
4.4	Leitz CMM.....	63
4.5	Experimental results per scan	70
4.6	Roundness from slow scanning speed	71
4.7	Roundness from medium scanning speed.....	72
4.8	Roundness from fast scanning speed.....	72
4.9	Inside calibrated waveform shown as deviations off of best fit radius.....	74
4.10	Force and deviations vs. angular position for slow scanning speed	75
4.11	Force and deviations vs. angular position for medium scanning speed.....	75
4.12	Force and deviations vs. angular position for fast scanning speed.....	76
4.13	Roundness with low frequency cut-off.....	77
4.14	Roundness from mid-range cut-off frequency.....	78
4.15	Roundness from high cut-off frequency	78
5.1	Schematic of modeling concept.....	80
5.2	Filtering parameters	82
5.3	Analytical separation of waves and marking of maxima and minima.....	83
5.4	Experimental filtering results – no filtering apparent.....	84
5.5	Experimental filtering results – filtering apparent.....	85
5.6	Input and output data for theoretical filter characterization.....	86
5.7	Measured and simulated filter output	88
5.8	MATLAB™ Digital filter specifications.....	89
5.9	Digital filter design in MATLAB™	91
5.10	Pole/zero plot for digital filter.....	91

5.11	Comparison of digital filter model to experimental filtering results	94
5.12	Experimental data showing noise beyond data range	95
5.13	Comparison of filtering with different cut-off frequencies.....	96
5.14	Servo loop	97
5.15	Natural frequency effects in experimental data sets	99
5.16	Combined effect of natural frequency and scanning speed on scanning performance	100
5.17	Graphical representation of the error between measured and calibrated values..	104
5.18	Error vs. angular position.....	105
5.19	Histogram of errors showing standard deviation and bias.....	106
5.20	Uncertainty versus speed	108
5.21	Uncertainty bands	109
5.22	Uncertainty bands for a single speed	110
5.23	3-D plot of uncertainty vs. wavelength and all scanning speeds	111
5.24	3-D plot of uncertainty vs. wavelength and slower speeds.....	112

Nomenclature

a	Positive real number
A	Constant amplitude of sine wave = 0.005 mm
b	Bias between the measured and calibrated values
d	Linear modulation parameter = 200
$dev_{bestfit_slow2005}$	Deviations from experimental data best-fit to slowest scan radius and center from 2005 (mm)
$dev_{bestfit_slow2006}$	Deviations from experimental data best-fit to slowest scan radius and center from 2006 (mm)
dev_{ori_cal}	Deviations off of best-fit calibrated radius (mm)
d_{ph}	Deflection of probe head (mm)
\bar{e}	Average normal distance between scanned points and calibrated spline (mm)
e_i	Normal distance between scanned point i and calibrated spline (mm)
e_s	Error signal
f	The function that relates the measurand to the input quantities and relates the output estimate and input estimates
F	Scanning force (Newtons)
f_b	Base frequency (Hz) = 10 Hz
F_d	Nominal scanning force
f_i	Input frequency (Hz)
F_m	Scanning force (g)

f_s	Sampling frequency (Hz)
$G(s)$	Filter transfer function in Laplace domain
h_f	Filter coefficients
i	Integer number of waves per quadrant
k	Coverage factor
K	Theoretical filter scaling factor
k_{sc}	Spring constant (Newtons/mm)
k_{scm}	Spring constant (185 g/mm)
l	Arc length (mm)
L	$\frac{2\pi R}{4}$ = length of one quadrant of circumference (mm)
m	Integer number of points in one quadrant of circumference for calibration
n	Positive integer
N	Number of points measured during experimental scan
n_f	Order of filter
R	Radius of a circle (mm)
R	Radius of curvature at a point (mm)
r_{cal}	Calibrated radius (mm)
r_{exp}	Radius of experimental data (mm)
R_i	Inner radial value at a given angular location (mm)
R_{f_i}	The least squares best fit average of all inside data points (mm)

R_{f_o}	The least squares best fit average of all outside data points (mm)
R_o	Outer radial value at a given angular location (mm)
$r_{slow2005}$	Best-fit radius from slowest scan speed in 2005 (mm)
$r_{slow2006}$	Best-fit radius from slowest scan speed in 2006 (mm)
R_{theor}	Theoretical inner or outer radius of ring (mm)
t	Vector of distance samples varying from 0 to L (mm)
t	Time since impulse (sec)
Td	Time delay coefficient
T_d	Damped period (sec)
t_f	Time increment (sec)
Tp3	Coefficient for third theoretical filter pole
Tw	Coefficient for theoretical filter pole
Tz	Coefficient of theoretical filter zero
U	Expanded uncertainty of output estimate y
u	Commanded position
$u(x_i)$	The standard uncertainty of the i^{th} input estimate x_i
$u_c(y)$	Combined standard uncertainty of output estimate y
u_{cal}	Calibration standard uncertainty from the calibration certificate
U_{cal}	Expanded calibration uncertainty
$u_i(y)$	The i^{th} component of the combined standard uncertainty $u_c(y)$ of the measurement result y
u_p	Standard uncertainty due to the measurement strategy

v	Scanning speed (mm/s)
$X(s)$	Input to filter in Laplace domain
x_{cal}	Estimate of the calibrated value (mm)
x_f	Filter sample
x_i	Estimate of input quantity X_i
X_i	The i^{th} input quantity
x_{mach}	x-axis of machine coordinate system
x_{part}	x-axis of part coordinate system
x_{ph}	Deflection of probe head in x-direction (mm)
y	The measurement result; estimate of Y ; output estimate
Y	Measurand
y	Deviations off of nominal circle (mm)
\bar{y}	Average measured value (mm)
$Y(s)$	Output of filter in Laplace domain
y_b	Deflection boundary curve (mm)
Y_f	Filter output
y_{mach}	y-axis of machine coordinate system
y_o	Actual measured position
y_{part}	y-axis of part coordinate system
y_{ph}	Deflection of probe head in y-direction (mm)
Zeta	Damping factor
z_{mach}	z-axis of machine coordinate system

z_{part}	z-axis of part coordinate system
z_{ph}	Deflection of probe head in z-direction (mm)
$\frac{\partial f}{\partial x_i}$	The sensitivity coefficient that describes how the output y varies with changes in the input quantity x_i
ζ	Damping ratio
θ	Angular location (rad)
κ	Curvature (1/mm)
λ	Wavelength (mm)
ϕ	Tangential angle (rad)
ω_d	Damped frequency (rad/sec)
ω_n	Natural frequency (rad/sec)

1. Introduction

Coordinate measuring machines, or CMMs, are used to collect three-dimensional coordinates on workpiece surfaces. With the first hard probes and later touch trigger probes, this collection consisted of a limited number of points that was used for calibration, inspection, process control, or engineering development. Today, scanning probes collect data at a much faster rate allowing CMMs not only to measure parts more quickly but also to be able to analyze “a product’s physical characteristics in greater detail than is normally articulated in an engineering drawing [1, p. 1].” This capability allows CMMs to measure a part’s surface down to the level of surface roughness. To achieve this level of detail, the density of data on the workpiece surface must be higher than that needed for conventional inspection activities, and the measurement uncertainty of the results should be as low as is reasonably achievable. New methods to estimate and then lower CMM task specific measurement uncertainties must be developed because existing techniques have limited capability and utility.

This research provides foundational work that will lead to lower measurement uncertainties in CMM pre-defined path scanning operations. Previous research has provided a thorough understanding of touch trigger probing and of methods to compensate for individual scanning errors. However, the complex interactions at the probe/surface interface of factors such as the probing force, scanning speed, data filters, and surface characteristics are not well understood. This research will model these

effects and provide an empirical model of scanning performance. This model will be used to develop an experimental method for selecting parameters such as probe tip diameter, data filter characteristics, scanning speed, and probing force to enable the reduction of measurement uncertainty. This work will quantify the utility of using CMMs to make short wavelength measurements. This capability is useful because it potentially eliminates the need for separate roundness testers. The methods developed in this research will be applicable to other precision metrology applications.

The second chapter provides background information on the new measurement uncertainty needs in metrology. An overview of the CMM system and measurement process is provided in order to highlight contributing factors to CMM measurement uncertainty, and the method to evaluate measurement uncertainties is given. Relevant previous work is then reviewed to show the existing techniques and tools that can be applied to this topic as well as the open problems which must be addressed.

The next three chapters describe the three main parts of this research: the calibration of the wavy ring artifact, the experimental work, and the modeling, data analysis and evaluation of those results. The final chapter outlines the conclusions from this research, suggests future work, and reviews the fundamental contributions of this project.

2. Literature Review

2.1. New CMM measurement uncertainty drivers

According to Swift [1], product inspection tests whether a part's features are within the tolerances given on the engineering drawing. The tolerances are defined according to ANSI Y14.5, and the sparse data gathered can be used to determine the form, location, profile, or orientation of part features. In contrast, dense data is needed to determine the roughness, waviness, or lay of the part surface. When parts are certified to be within tolerance, engineers can be assured that the manufacturing process is functioning properly.

Many companies that inspect products are adopting international standards, such as ISO 17025, that require an assessment of measurement uncertainty. In order to be accredited according to ISO 17025, "testing laboratories shall have and shall apply procedures for estimating uncertainty of measurement [2, p. 14]." In the case of CMMs, this is an especially challenging task due to the many types of measurements made on these machines which each require a unique uncertainty budget. Therefore, an array of measurement uncertainty techniques is needed. The traceability of measurements defined in the Guide to the Expression of Uncertainty in Measurement [3,4] also requires a statement of measurement uncertainty. ASME B89.7.5 [5] explains the requirements for this traceability and gives examples of traceability for various applications.

Additionally, ISO 14253-1 [6] and ASME B89.7.3.1 [7] put forth decision rules for accepting and rejecting parts. ISO has a stringent acceptance and relaxed rejection zone which reduces the upper and lower acceptance specifications by a guard band that is 100% of the uncertainty by default. Large measurement uncertainties drastically reduce the allowable manufacturing tolerance and can therefore dictate the inspection plan including the choice of equipment. Therefore, companies want to develop methods for establishing reasonably low measurement uncertainty values for their measurements [8].

In order to be economically competitive, the metrologist must measure the part as fast as possible while maintaining the acceptable level of uncertainty. Information is needed as to how various process parameters affect the measurement capability of a CMM. This research will focus on providing this type of information. Then, if the process parameters cannot be adjusted to meet the manufacturing and metrology requirements, the measurement uncertainties could be lowered by investments in better equipment or more stable environments.

2.2. Sources of measurement uncertainty

A CMM has both hardware and software components that contribute to the machine's performance. The hardware components include the probe head, the CMM platform, and the control circuitry. The software includes the operator interface software, the evaluation software, and the controller software. The operator interface software allows

the operator to create a measurement plan. The evaluation software interprets the collected data and provides an assessment of the workpiece dimensions. The operator creates the typical measurement plan on a PC and then transfers it to the controller. The controller software interfaces with the CMM mechanical systems to collect the desired data. The data are then passed through the controller back to the PC where the evaluation schemes selected by the operator interpret the data and return the results to the user.

The CMM hardware contributes most to a CMM's ability to make scanning measurements. Specifically, the probe head must have a "wide linear control range with low damping permitting highly dynamic contour following [9, p. 79]." The next most important characteristics are that the mechanical system must be rigid and that the control system must be capable of commanding the axes to travel to the proper positions with a high accuracy. The filtering implemented in the software system is also important. CMM scanning measurements can also be significantly impacted by the environment in which the measurements are taken. Temperature and vibration are two of the most important environmental factors to be controlled.

Measurement uncertainty is defined in the International Vocabulary of Basic and General Terms in Metrology [10] as "a parameter, associated with the result of a measurement that characterizes the dispersion of the values that could reasonably be attributed to the measurand [4, p. 34]." ISO 14253-2 [11], lists ten primary contributors to the uncertainty of a measured characteristic:

1. Environment

2. Reference element of measurement equipment
3. Measuring equipment
4. Measuring setup
5. Software and calculations
6. Metrologist
7. Measuring object
8. Definitions of the measurand
9. Measuring procedure
10. Physical constants.

Environmental sources of measurement uncertainty include the temperature, humidity, dirt, and vibrations present at the time of the measurement. The reference element of measurement equipment refers to the scales that are used by the CMM to determine location. The material of the scale, its fixturing, and calibration all can introduce measurement uncertainty. The measuring equipment itself is a source of measurement uncertainty since no piece of equipment is constructed with perfect geometry. Additionally, the probe configuration used can contribute uncertainty [8].

The measuring setup refers to the fixturing, how stable the part is, and whether it is distorted by the fixture. All of these are sources of uncertainty. The software used is another source of uncertainty. The algorithms used in the software can also be incorrect and lead to uncertainty in a measurement. The metrologist can create uncertainty by causing thermal expansion of the setup from body heat.

The object to be measured introduces uncertainty because it will never be perfectly clean, and it may be subject to deformation from the probe tip or fixturing. The definition of the measurand can also produce uncertainty. For example, with point to point probing, every point in a circle cannot be measured. If the measurand is then defined as the minimum circumscribed circle, some uncertainty will exist because the measurand requires the measurement of every point [12]. The measuring procedure includes the uncertainty introduced by the choice of equipment, fixturing, and measurement procedure. The final source of uncertainty described in ISO 14253-2 is the uncertainty in the knowledge of physical constants such as the coefficient of thermal expansion.

Determination of CMM measurement uncertainty is complex due not only to the variations in these contributing factors but also to the many different measurands measured on CMMs including dimensions, locations, and form. In ISO terminology [3], all of these contributors to measurement uncertainty are called influence quantities. An influence quantity is defined as a factor “that is not the measurand but that affects the result of the measurement [4, p. 32].” A quantity influences a measurement when the condition is imperfectly corrected for or when its effects are imperfectly approximated [8]. The influence of these quantities must be determined in the uncertainty evaluation. Once this information is known, methods can be developed to lower the influence of these quantities on the measurand. A nice discussion of influence quantities can be found in Phillips et al [13].

2.3. Method of determining CMM measurement uncertainty

Researchers must understand how CMM measurement uncertainty is evaluated before they can work to reduce it. According to Phillips [8], there are the following basic steps of uncertainty evaluation when the Guide to the Expression of Uncertainty in Measurement [3,4] is followed. Worked examples using this method are found in B89.7.3.2 [14]. This method is useful when a mathematical representation of the measurement is known.

1. Specify the measurand and the values of all influence quantities

This specification should exactly describe the measurand and measurement procedure in such a way as to produce a repeatable measurement result.

2. State the validity conditions

The validity conditions are the values of the influence quantities given in the specification of the measurand and are the conditions for which the uncertainty statement will be valid. An extended set of validity conditions can also be given for the range of values of influence quantities expected during the use of a given measuring process.

3. List the influence quantities

The influence quantities or uncertainty sources are given in the previous section. These uncertainty sources are classified into two categories: Type A and B based on the method used to determine them. Type A components are calculated by

statistical methods while Type B components are determined by non-statistical means.

4. Determine the input quantities

The measurand, Y , can be defined according to Equation 2.1 where X_i is the i^{th} input quantity and f is the function that relates the two. An input quantity may be a combination of several related influence quantities. Influence quantities are grouped according to the way in which their influence is quantified, whether by analytic equation, procedure, algorithm, or expert opinion; namely,

$$Y = f(X_1, X_2, \dots, X_i, \dots, X_N). \quad (2.1)$$

5. Evaluate the standard uncertainty of each input quantity

The i^{th} component of the combined standard uncertainty of the measurement result y is $u_i(y)$ which is calculated according to Equation 2.2 where $u(x_i)$ is the standard uncertainty of the i^{th} input quantity and $\frac{\partial f}{\partial x_i}$ is the sensitivity coefficient [4] that describes how the output y varies with changes in the input quantity x_i , as

$$u_i(y) = \frac{\partial f}{\partial x_i} u(x_i). \quad (2.2)$$

The method used to calculate u_i depends on the function f . For analytic functions, calculus can be used to determine u_i . When f is a procedure, experimentation is used to find u_i by varying x_i and noting the resulting variations in y . Examples of these

methods are found in Phillips et al [15] which evaluates the uncertainty of simple ring gauge measurements made on a CMM using both analytic and experimental representations of the uncertainty. Rasnick et al [16] gives a more complex example of experimental determination of uncertainty. In this case, a combination of simple experimental results is used to evaluate the measurement uncertainty of complex features such as gear profiles when they are measured on a CMM. For algorithm based functions, Monte Carlo simulations can be used that vary the x_i within the probability distribution and calculate y repeatedly to determine the standard deviation of y . Phillips et al [17] used a Monte Carlo based simulation by constraints method to calculate CMM task specific measurement uncertainty.

6. Combine the input quantities and calculate u_c

The combined standard uncertainty, u_c , is “one standard deviation of the probability distribution centered around the measurement result, y [8, p. 54].”

Typically, the input quantities are uncorrelated, and the combined standard uncertainty is found from Equation 2.3 as

$$u_c(y) = \sqrt{\sum_{i=1}^N u_i^2(y)}. \quad (2.3)$$

7. Use the coverage factor to obtain the expanded uncertainty U

Often, companies desire to report an interval that contains more than one standard deviation (68%) for normally distributed measurement results. Then, a coverage factor k can be used to calculate the expanded uncertainty, $U = k \cdot u_c(y)$. The

coverage factor, k , is typically 2 or 3 which for normally distributed measurement results, gives a 95 or 99.73% level of confidence that the true value of the measurand actually lies within the interval $y \pm U$.

8. Employ the uncertainty statement in a subsequent measurement

Once the uncertainty has been determined, the uncertainty can then be reported on a calibration certificate or used in the decision rules for inspecting products.

In many cases, a mathematical model of the measurement does not exist, and the above method must be modified. In these situations, expert judgment, experimental techniques, or computer simulations can be used to determine the task specific measurement uncertainty [18].

2.4. Existing Methods of Reducing CMM Measurement Uncertainty

Researchers must develop methods to reduce the uncertainty in a measurement. This section will review existing methods for reducing CMM measurement uncertainty in three of the categories given in Section 2.2: the environment, software and calculations, and measuring equipment characteristics such as the CMM geometry and probe. These categories are of particular interest because in these areas the user selects parameters which determine the measuring performance of the CMM.

2.4.1. Measuring environment

The machine bulk temperature and/or the thermal gradients within the CMM, part, and environment can have a drastic influence on CMM measurement uncertainty. Thermal

variations can be both spatial and temporal, so the transient temperature effects must be addressed carefully because they can add significant measurement uncertainty.

Temperature increases cause thermal expansion and distortion of both part and machine.

The machine errors caused by the expansion are determined by the assembly and materials of the CMM as well as the thermal gradients within the machine structure.

Thermal errors from part expansion can be prevented by thermally soaking the part.

Errors from machine expansion can be prevented by operating the CMM in the narrow temperature range at which the CMM was error mapped and by correcting within that range according to the thermal error index method described in national standards [19].

This also requires the elimination of intermittent thermal disturbances due to sources such as personnel, lighting, etc. Alternatively, some CMMs are equipped with a real-time temperature compensation system. Researchers have used finite element analysis to study the thermal errors [20].

Vibrations in CMM system performance can result from environmental vibrations, vibrations induced within the CMM such as those due to accelerations or from air bearing instabilities, or from the contact of the probe with the workpiece. Rivin [21] studied the benefits of passive versus active damping for environmental vibrations and determined that passive damping is suitable in most cases. A dynamic model of a precision machine is presented that can be used to determine the sensitivity of machine parameters to vibrations. Singhose et al [22] demonstrated how to improve CMM performance by decreasing acceleration induced vibrations through the use of input shaping. Although this study was conducted on touch trigger probes operated in the point-to-point mode, this

method of active damping would be applicable to the scanning induced accelerations as well. Van Vliet and Schellekens [23] studied the bouncing that can occur when the probe contacts the workpiece. These vibrations lead to inaccurate measurements or can even cause the probe to lose contact with the workpiece which then requires recovery time and decreases throughput. The recommendation is for a probe with high internal damping to reduce the bouncing.

CMM and probe manufacturers also continue to develop ways to reduce vibrations in CMM systems. Browne and Sharpe [24] patented passive dampers positioned to reduce vibrations caused by the motor and gearing. Additionally, they patented passive dampers located in the legs of a CMM to compensate for acceleration induced vibrations [25]. Leitz [26] patented an active vibration damping system that includes a vibration sensor, control system, and actuator to provide the active damping to compensate for acceleration induced vibrations. Renishaw [27] developed a method to reduce probe vibrations by measuring the accelerations with accelerometers and then integrating the signals to velocities which are then used in a velocity feedback control loop to reduce changes in probe deflection due to accelerations. This method can compensate for vibrations due to drive motors, external vibrations, air bearing instabilities, and kinematics. Past work cited in this patent describes other methods to reduce these vibrations such as to “reduce the overall feedback gain of the position and velocity servo loops [27, p. 3]” to use a notch filter in the velocity loop, or to characterize the elastic bending of the CMM.

2.4.2. Software and calculations

This section examines methods used to reduce the measurement uncertainty caused by the CMM data filtering and analysis methods. Data filtering first occurs due to the interaction between the probe tip and the workpiece and is influenced by factors such as probe size, shape, and friction. Secondly, the inspection data are filtered by the probe head dynamics. If the probe cannot follow the form quickly enough, data will be lost. Finally, the software filters the data using filters that are described in national standards [9]. These filters can be used to eliminate noise in the data caused by vibrations or to eliminate certain segments of roughness, waviness, or form.

After data have been filtered, they can then be fitted to an ideal geometry. The results produced by data fitting algorithms are tied to the sampling strategy used to gather the data. The selections of the algorithm and sampling strategy must be made considering the purpose of the parts and the information needed from the measurement. For example, algorithms for evaluating circular data include least-squares, minimum zone, maximum inscribed, and minimum circumscribed. Each algorithm provides different information about the circular feature under study.

Bourdet et al [28] describes how the least-squares algorithm used during probe calibration to determine the center and radius of the sphere is impacted by whether the radius of the calibration sphere is fixed or is included in the minimization within the least-squares optimization. The influence of the number of points and the arc of the

sphere measured during probe calibration on the algorithm were also evaluated. Dowling et al [29] provides a comprehensive review from a statistical perspective of how various fitting algorithms such as least-squares and minimum zone are related to design intent and how the sampling strategy affects the results of fitting algorithms. Finite sampling always affects the results from the fitting algorithms because when a finite number of data points are collected for a measurement, the sampling strategy determines what components of part geometry can be detected, and this leads to measurement uncertainty. Any calculation of measurement uncertainty must include the contributions of the software and sampling strategy selected [19].

2.4.3. CMM geometry

CMM geometry errors are linked to the machine tables, guide ways, bearings, and drives and do not include errors in the computer systems or probing system. The CMM geometry is prone to rigid body errors, structural distortions, and dynamic errors. A typical CMM has three axes and twenty-one rigid body errors. Each axis contributes a scale error, two mutually orthogonal straightness errors, and three rotational errors (roll, pitch, and yaw). Additionally, three squareness errors exist between pairs of axes. CMM manufacturers attempt to reduce these errors by producing well-designed and carefully fabricated mechanical platforms. Software based error compensation techniques are also used to reduce repeatable errors [19].

CMM performance evaluation techniques are used to evaluate how the remaining errors contribute to the machine's measurement uncertainty. Standards such as the ISO 10360 series [30] and ASME B89.4.1 [31] provide standardized tests and methods of evaluating CMM performance. These standards require significant time to complete, and a large suite of interim testing methods and artifacts have been developed to provide alternate, less time consuming testing options that can be performed on a more frequent basis, typically several times a year. A thorough review of these techniques is presented in Miguel et al [32].

The CMM is not a rigid body and is subject to structural distortions. When these distortions are repeatable, they can be reduced through error compensation techniques. However, structural distortions due to thermal gradients in the environment or due to the variable weight of different parts that may be loaded on a machine in different locations are more difficult to predict. Thermally induced geometry errors can be avoided by maintaining strict temperature control in the environment or compensated for if the CMM has temperature sensors and a reliable temperature compensation model [19].

The errors described above may be described as static errors because they exist when the machine is in a stationary condition. An additional source of CMM geometry errors are the dynamic motion errors that occur while the machine is moving from one location to another. Machine dynamic error sources are related to speeds, accelerations, and the relative location of the CMM axes during measurements. Large CMMs and scanning CMMs are especially prone to dynamic errors. In scanning, the CMM is usually

accelerated while probing, and scanning path errors related to the machine servo system degrade the measurement accuracy. These errors can be avoided by holding the probe in a fixed position during the scan and rotating the part instead. Some CMMs can compensate for these dynamic errors in the error map [19].

2.4.4. CMM probe

The CMM probe is a major source of measurement uncertainty, but many techniques exist for reducing these effects. The probe related error sources include dynamic probe errors, the stylus ball size, probe lobing, multiple styli effects, and probe changing issues. The stylus ball size and probe lobing are related to the calibration procedure which will be described later in this section. The use of multiple styli such as on a star probe can produce an additional error source because errors occur in locating each probe tip relative to the other probe tips. Additionally, when probe changers are used, the repeatability of the changing system can be a primary source of error unless each probe is re-calibrated after a probe change [19].

This research focuses on errors in scanning probes and includes the assessment of their performance. Continuous scanning probes maintain contact with a part surface during a measurement in contrast to touch trigger probes which make contact with the workpiece only at the discrete points where data are collected. Most scanning probes and some point to point probes are analog transducers that produce an output signal that is proportional to the displacement of the probe. The size of the linear region of the scanning probe limits

the probe accuracy for a given probing speed. A larger linear region allows the probe to more accurately respond to rapid changes in the part surface.

The advantage of the scanning probe technology is that the scanning process yields ten to fifty times as much data over a given time period [33]. For this reason, scanning probes are well suited for measuring form and contours of surfaces. The additional data density also results in a lower measurement uncertainty. Since the probe remains in contact with the surface, performance depends on the roughness, discontinuities, and lubricity of the workpiece/stylus interface.

Scanning can be done in a closed-loop or open-loop mode and with a pre-defined path or a not pre-defined path. In closed-loop scanning, the probe maintains contact with an unknown surface by maintaining a constant deflection. Closed-loop scanning is more demanding on the controller and therefore speeds are lower than for open-loop scanning. Open-loop scanning drives the probe along a known path normal to the surface nominal [33]. In pre-defined path scanning, the probing system motion is directed along a pre-defined line of intended contact points. This sometimes involves a mixture of open- and closed-loop control. In not pre-defined path scanning, feedback from the probing system directs the motion of the probing system [3,4].

Metrology companies such as Brown and Sharpe, Renishaw, and Mitutoyo are actively developing new scanning technology to reduce measurement uncertainty. However, little technical information is available in the open literature except for patent descriptions and

product descriptions. For example, the state-of-the-art scanning technologies available from Renishaw [34] are the SP25M and the SP80 probes which are lightweight, passive (not motored), with a high natural frequency, measure deflections optically, use dynamic error compensation from Renscan technology to compensate for inertia, and can be used at speeds of over 500 mm/s.

The calibration routines being developed by these companies are some of the most significant advances in reducing uncertainty in scanning measurements. The purpose of the calibration routine is to allow the location of the workpiece surface to be determined based on the center of the probe tip which is the point known by the probe as data are taken. Therefore, the calibration registers the offset between the center of the probe tip and the point of contact. Calibration routines are typically performed by measuring a very round sphere. Renishaw [34] measures this sphere with a series of bi-directional scans. Then, during scanning, splines are created that shift the data by the probe radius. Renishaw's latest calibration routines [35] generate a transformation matrix that includes consideration of misalignment between the probe axes and the CMM axes, non-orthogonality among the probe axes, and scaling errors. The new calibration method is also not sensitive to slipping at the probe/workpiece interface.

Renishaw [36] now error maps the probe deflections to improve probing accuracy. The error map includes compensation for friction which was determined to have a significant impact on measuring performance. This has improved radial measuring errors to sub-micrometer level. Additionally, Renishaw's [36] latest dynamic calibration routines

correct for errors in both the CMM and probe caused by different accelerations generated by different scanning speeds. This is not a probe calibration routine but a scanning system calibration routine. The result is that faster scanning speeds can be used.

Another method of reducing measurement uncertainty due to probing is to conduct performance tests on the probe and model the effects of user selectable parameters. Miguel et al [37] reviews the techniques that have been used in the past for touch trigger probe performance testing. Additionally, Feng and Pandey [38] report the effects of travel speed, pitch value, probe angle, probe size, and feature size on measurement uncertainty for a CMM using a touch trigger probe determined by fractional factorial experimentation. Some of the testing procedures reviewed by Miguel would be valid for analog scanning probe tests though the results would not be applicable since the research was conducted on analog touch trigger probes. Relatively little research has been done with scanning probes. Tang and Sun [39] did conduct a study using a scanning probe and studied the effects of sample size, speed, stylus deflection, internal vs. outer diameter, and feature size.

The performance evaluation standard for scanning is ISO 10360-4 [30]. This standard measures a nominally 25 mm diameter calibrated sphere with a surface roughness of less than 0.05 micrometers. The scan performance is quantified by the range of radii calculated and the deviation of the best fit radius from the calibrated value. Since this surface is almost perfectly smooth, this is a test of scanning long wavelength features. This test allows additions to the surface introduced by the CMM to be seen, but it does

not show what data has been removed by the CMM. The mode selected, whether low or high point density and predefined or not predefined scanning, impacts the results [40].

A two-axis static and dynamic force characterization device was developed at UNC-Charlotte. Pereira [41] used this device to measure the forces on a probe during a scanning measurement and then to develop a model that compensates for the errors induced by centripetal acceleration when measuring ring gauges of various sizes and multiple scanning speeds in open loop mode. This research only considers the effects on the long wavelengths represented by the entire ring gauge diameter.

Other research at UNC-Charlotte [40] evaluated how specific variables such as speed, radius of curvature, stylus stiffness, scanning mode, and machine stiffness affected the form measurement of a ring gauge. The authors note that the dynamics of the probe head have a strong influence on scanning capability. Additionally, work was done using a grid plate to separate machine and probe head errors. A method for verifying the dynamic natural frequency of a probe head was also developed that measures a hole with a constant wavelength, constant amplitude sinusoid at increasing speeds. The analysis notes that a step increase in form occurs at the natural frequency.

By using artifacts with waves on the surface, additions as well as subtractions from the surface data can be observed. UNC-Charlotte [42] has developed scanning artifacts with wavelengths of 5-20 mm. These artifacts have a constant wavelength sine wave machined on either a linear or disc artifact with an amplitude of 2 mm for the 10 and 20

mm wavelengths, and an amplitude of 10 μm for the 5 mm wavelength. Two methods of analyzing the data are presented. Either the data is fit to a theoretically perfect sine wave of fixed frequency or to a reference wave measured at a slow scan speed. The degradation at increasing speeds is then noted.

Several research groups have created systems that simulate the measurement of artifacts with shorter wavelengths. This method uses a piezo to excite the probe head and does not involve the measurement of an actual surface. As a result, these studies do not include the effects of friction or the probe tip and workpiece interaction. They also do not provide a way to quantify the effects of scanning using the machine axes as measuring an actual artifact would allow.

A wave with a wavelength of approximately 2 mm and amplitude of 100 μm was simulated using a piezotranslator stage in Poland [43]. The results generated by the probe when vibrated by the piezotranslator can then be compared to the reference characteristic signal that was to be generated by the piezotranslator and measured independently using a laser interferometer. As the author concludes, the most sensitive region is that of the shortest simulated wavelength features.

PTB [44] developed a similar methodology for examining dynamic probe performance. A piezo vibration platform was used to generate waveforms including sinusoids, square, triangle, swept sinusoids, and arbitrary waveforms. The authors show how the device can be used for traceable, dynamic probe calibration of form testers and plan to use it to study

the amplitude-frequency response of a variety of probes. The advantage of this system is the flexibility of input waveform. The disadvantage is that the generated waveform does not always match the theoretical waveform due to hysteresis of the piezo.

Two similar Dutch systems are described by Haitjema and Kotte [45]. The open-loop system operates at higher frequencies but is less repeatable than the closed-loop piezo system. The use of the system to determine the frequency response of a system is shown. These systems are lab based instruments at a National Metrology Institute that require precise laser interferometers and complex set-ups and are therefore not suitable for industrial use.

As previously mentioned, the piezo systems just described do not fully represent the effects of scanning surfaces that contain short wavelengths because the probe tip interaction with the surface is not included. An artifact with short wavelengths would be required to obtain this information. This information is important to CMM users because actual parts are not smooth and contain defects of various sizes that can be represented by these short wavelengths. It would be desirable to model the effects of scanning these wavy surfaces in order to determine parameters that would reduce the measurement uncertainty.

PTB [46] has manufactured multi-wave standards for the calibration of form measuring machines. These artifacts contain superimposed sinusoidal waves of varying amplitude and frequency that are machined with a fast tool servo onto a nickel plated aluminum

disk. The analysis of measured data is performed in frequency space by examining how well a form machine detects the correct amplitude for wavelengths between 0.5 mm and 50 mm. The amplitudes vary from 1-5 μm . While the artifact is appropriate for the calibration of form testers, it is not as applicable to CMMs which measure spatial profiles instead of frequencies and amplitudes. It would be difficult to relate the Fourier analysis of data back to the capability of the CMM to make a given measurement because the averaging that occurs in determining the amplitude at a given frequency eliminates much of the localized information generated during the measurement. However, these multi-wave standards have been used to provide a measure of CMM scanning performance by comparing the spectral amplitudes for given frequencies and the roundness to that determined by a form tester [47].

Based on this need for a CMM scanning artifact that can be used to model the effects of scanning and thereby lower measurement uncertainty for short wavelength measurements, North Carolina State University [48] designed and fabricated a ring with a swept sine wave machined with a fast tool servo onto the inner and outer diameters. The swept sine wave has an amplitude of five micrometers and a wavelength that varies from approximately 0.5-6 mm. The wavy ring was fabricated with a stainless steel substrate with nickel plating for durability. A simulated data analysis concept is reported in which an air-bearing capacitance gauge was excited using the Fast Tool Servo to simulate the measurement of the ring with a CMM probe. Differences in cap gauge response with and without filtering were observed [49]. No measurements or analysis of measurements

from a scanning CMM were reported. The wavy ring artifact is used in this dissertation to develop a new method for reducing scanning CMM measurement uncertainty.

2.5. New method of reducing CMM measurement uncertainty

This research builds on the understanding of drivers for measurement uncertainty research, the sources of measurement uncertainty in CMM scanning, the method of calculating measurement uncertainty, and existing methods of lowering measurement uncertainty. Specifically, this research models the complex interactions at the interface of the probe and workpiece surface. Implicitly included in this model are the surface position, normal force, scanning speed, gravity, the non-linear friction force which is determined from the surface normal to the probe tip, the surface contact patch, and the mass, spring, and damping characteristics of the probe. The models presented provide information on scanning parameter choices that can lower the measurement uncertainty.

3. Calibration of the Wavy Ring Artifact

3.1. Description of artifact

In order to test the capability of a CMM to scan short wavelength features, a new artifact was developed and manufactured at North Carolina State University [48]. This artifact termed the “wavy ring” and used in this research is shown in Figure 3.1. The ring has an inner diameter of 152 mm, an outer diameter of 203 mm, and a thickness of 25 mm. The ring is 17-4 PH stainless steel that was heated treated for dimensional stability. An electroless nickel plating was added not only to provide durability but also to give a non-ferrous surface which would be suitable for machining with a diamond tool. The bore holes can be used to establish the angular positioning for the ring. The faces were diamond turned.



Figure 3.1: Wavy ring artifact

As can be seen in Figure 3.1, a band of swept sine waves was machined on the inner and outer circumferences of the ring using a Fast Tool Servo. Details of the manufacturing process can be found in Folkert [48]. The swept sine wave provides a constantly changing wavelength that simulates a range of surface conditions. The swept sine wave is shown in Figure 3.2, and the formula is given in Equation 3.1 [48]. This equation produces wavelengths varying in length from 0.531 mm to 6.24 mm for the inner radius given by

$$y = A \sin \left[\frac{2\pi}{L^2} (dt^2 + f_b Lt) \right] \quad (3.1)$$

where

y = deviations off of nominal circle (mm),

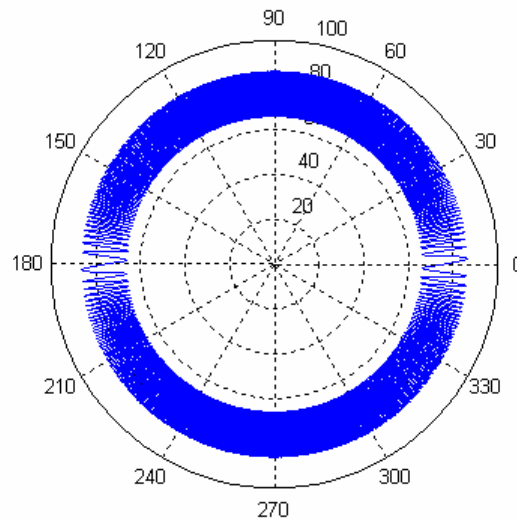


Figure 3.2: Swept sine wave

$A =$ constant amplitude of sine wave = 0.005 mm,

$$L = \frac{2\pi R_{\text{theor}}}{4} = \text{length of one quadrant of circumference (mm)},$$

$R_{\text{theor}} =$ theoretical inner or outer radius of ring (mm),

$f_b = 10 =$ base frequency (Hz),

$d = 200 =$ linear modulation parameter, and

$t =$ vector of distance samples varying from 0 to L (mm).

To generate the waveform for either the inner or outer surface, R_{theor} is defined as the theoretical inner or outer radius, respectively. In Figure 3.2, the waves are amplified by a factor of 2000. In this application, the sine wave sweeps from a long wavelength at zero degrees to a short wavelength at 90 degrees and then increases from that short wavelength back to the long wavelength over 180 degrees. The wave is then completed by decreasing back to a short and then increasing again to a long wavelength as the wave comes back to complete the circle.

3.2. Basis for calibration

The International Vocabulary of Basic and General Terms in Metrology [10] defines a calibration as a “set of operations that establish, under specified conditions, the relationship between values of quantities indicated by a measuring instrument or measuring system, or values represented by a material measure or a reference material, and the corresponding values realized by standards [13, p. 371].” The first note for this

definition says that “the result of a calibration permits either the assignment of values of measurands to the indications or the determination of corrections with respect to the indications [13, p. 372].” In order to achieve traceability to metrological standards, a calibration must be accompanied by an uncertainty statement.

The calibration of the artifact is necessary for determination of uncertainty of later measurements of the artifact. In this research, the calibration of the artifact will allow traceable measurements of the artifact to be made. These measurements can be used to quantify the performance of the CMM when scanning. Traceability refers to the unbroken chain of comparisons back to the international standard of length.

Artifact calibrations can be primary, secondary, or working. Primary calibrations refer to calibration of a standard which is used as the basis for secondary standards. The secondary and working standard calibrations will always have a higher uncertainty because they are based on the primary calibration and then have added uncertainty from the subsequent measurement steps.

3.3. Calibration development

3.3.1. Determination of measurand

The measurand is that which is being measured and is defined by a set of specifications that describe the conditions for measurement. The measurand should be precisely defined so that the measurement results provide the desired information [13]. The

measurement uncertainty components vary based on the selection of the measurand. Therefore, a measurand for a standard should be selected that includes the measurement uncertainty components of interest. The measurand selected for the wavy ring artifact is shown in Figure 3.3 and was based on these criteria.

If the measurand were defined as a profile off of the center location, the measurement uncertainty would likely be 2-3 micrometers which would be significant in comparison to the 5 micrometer amplitude wave. The majority of this uncertainty would be due to the ability of the CMM to measure the radius instead of the waves. Instead, the measurand can be defined as deviations from a best fit circle. This eliminates the measurement uncertainty component of measuring radius that is not critical to the purpose of the artifact.

The measurand shown in Figure 3.3 is a profile tolerance. A profile tolerance as defined in Y14.5M “may control form, orientation, size, and location depending on how it is applied [50, p. 157].” The tolerance shown in Figure 3.3 gives the profile by means of an equation which defines the profile, R_i , as

$$R_i = R_{f_i} + 0.005 \sin\left(\frac{1600\theta^2}{\pi} + 40\theta\right)mm \quad (3.2)$$

and R_o as

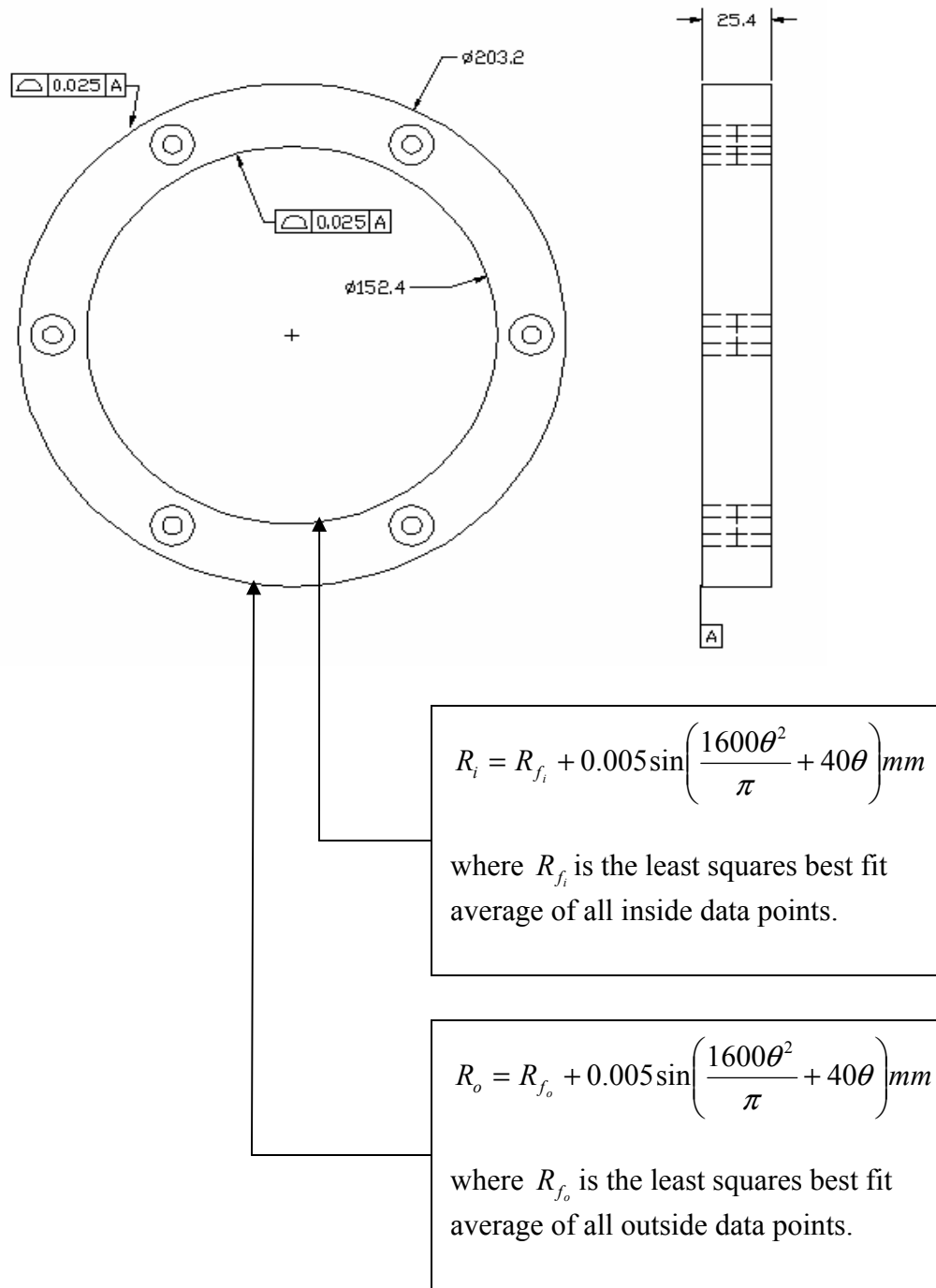


Figure 3.3: Toleranced drawing of measurand

$$R_o = R_{f_o} + 0.005 \sin\left(\frac{1600\theta^2}{\pi} + 40\theta\right)mm \quad (3.3)$$

where at each angular location, θ , the profile is the superposition of the best fit radius, R_{f_i} or R_{f_o} , and the waveform given in Equation 3.1. The argument of the sine function is simplified by substituting $t=R_{\text{theor}}\theta$ and the values of f_b , d , and L . When calculating t for the inner or outer wave, R_{theor} is defined as the inner or outer theoretical radius, respectively.

The profile is referenced to the datum on the top of the artifact as shown in the datum reference frame. The profile tolerance generates a 0.025 mm wide boundary divided evenly on either side of the true or mathematically defined profiles, R_i and R_o . By this definition, the profile measurement includes the angular location of the waveform and the waveform itself. Referencing the waveform to either the best fit inner radius, R_{f_i} , or the best fit outer radius, R_{f_o} , instead of the nominal radius prevents manufacturing errors that affected the best fit radius from contributing to the uncertainty.

3.3.2. Desired measurement uncertainty

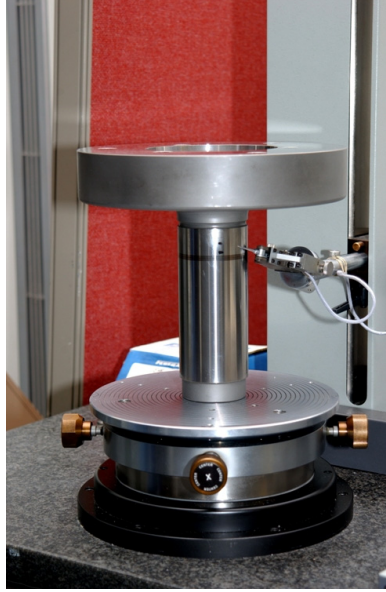
The calibration methodology will in large part be based on the required measurement uncertainty of the experimental work. This requirement will dictate not only the type of equipment required, but also the machine selection, the number of points, the density of points, and the calibration procedure. Since this is a new area of research, it is desired that the uncertainty of the artifact calibration be as low as reasonably achievable, so that

the widest possible range of performance indices can be explored. Once the scanning models are selected, calculations could then show whether a higher artifact uncertainty would be acceptable. A low uncertainty is also needed because only one ring will be calibrated as a primary standard. This ring will later be used to calibrate a secondary standard ring which will have a higher uncertainty than the primary ring. In each case, the uncertainty in the calibration results will include the positioning capability of the rotary table, the ability to measure a length from the center of the rotary table, and the ability of the CMM to measure the wave pattern.

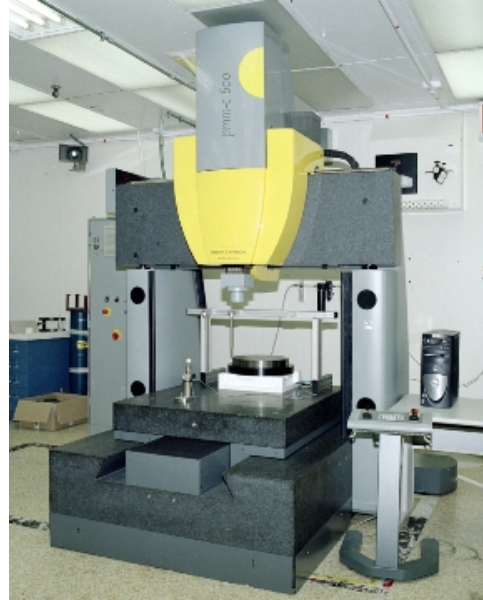
The 4:1 and 10:1 rule commonly used in industry says that the measurement uncertainty should be less than one-fourth to one-tenth of the tolerance [19]. In this research, the ring does not have a specified tolerance for acceptance of measurement results. However, since the peak-to-valley deviations are 10 micrometers, the desired uncertainty would be less than one micrometer so that the data is not completely uncertain. A lower measurement uncertainty will exist in the long wavelength sections due to the slower changes in slope in the wave which are more easily measured. Therefore, an uncertainty band could be generated that varies with wavelength.

3.3.3. Machine selection

Two classes of equipment were considered for the calibration of the artifact as shown in Figure 3.4: (a) roundness machines and (b) CMMs. The purpose of a roundness machine is to measure deviations from perfect roundness. Spherical and cylindrical workpieces



Federal Formscan 3200
(a) Roundness Machine



Leitz PMM-C
(b) CMM

Figure 3.4: Machines considered for calibration

can be measured on these machines. The advantage of the roundness machine is that it can provide a low uncertainty in measuring roundness parameters. However, these machines would not calibrate the size of the ring which is necessary for the study of a surface profile. If the ring were to be calibrated on a roundness machine, separate calibrations of size would also be required. As mentioned previously, the size uncertainty would then dominate the measurement uncertainty.

A CMM can calculate the size as well as the roundness and is therefore the preferred calibration platform. Unlike the roundness machines with its stationary probe that maintains contact with a rotating part, the CMM probe is typically moved on guides both vertically and horizontally. This can introduce geometry errors. In order to eliminate this error source, a rotary table was used in the calibration.

Once the class of machine had been selected, the specific machine for calibration was chosen. NIST was selected to perform the calibration because their National Metrology Institute standing gives ultimate credence to the calibration and subsequent use of the artifact in the development of national scanning standards. The NIST M-48 located in Gaithersburg, Maryland, is shown in Figure 3.5. The M-48 has a rotary table and can perform the desired calibration with the very low uncertainty that is expected from the National Measurement Institute, NIST.

3.3.4. Point spacing

The calibration data for the swept sine waveform can be considered as sampled data points on a continuous sine wave. The point spacing must select the proper distribution of points on the waveform. Past practice spaces probing points at equal angular



Figure 3.5 Moore M-48 at NIST

distributions. This distribution does not account for the varying wavelength. Therefore, an algorithm was created that would vary the point spacing with wavelength. This would allow each wave to theoretically have the same number of calibration points.

According to Shannon's sampling theorem, the minimum sampling rate for each wave should be the Nyquist rate which is defined as twice the maximum frequency in the signal [51]. In order to recreate the sine wave with higher fidelity, each wave should be sampled with 2^n samples per wave where n is greater than or equal to two to maintain the conditions required by Shannon's sampling theorem. By using 2^n samples per wave, each wave will be sampled at equal divisions of the wave. The resulting sampling for $n=2, 3,$ and 5 are shown in Figure 3.6.

(a) 4 points

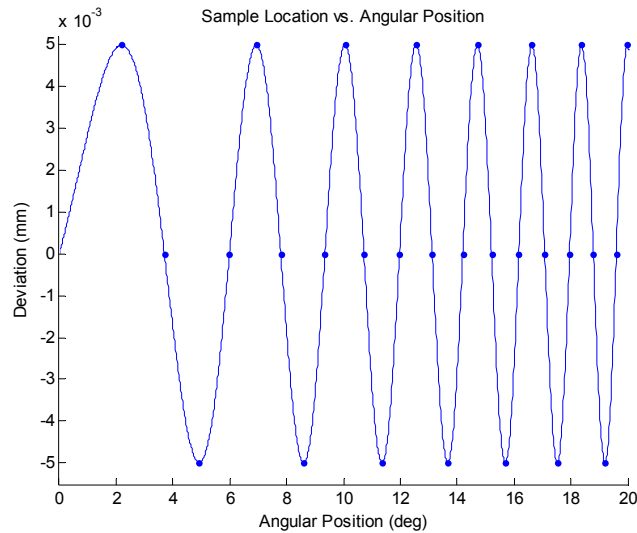
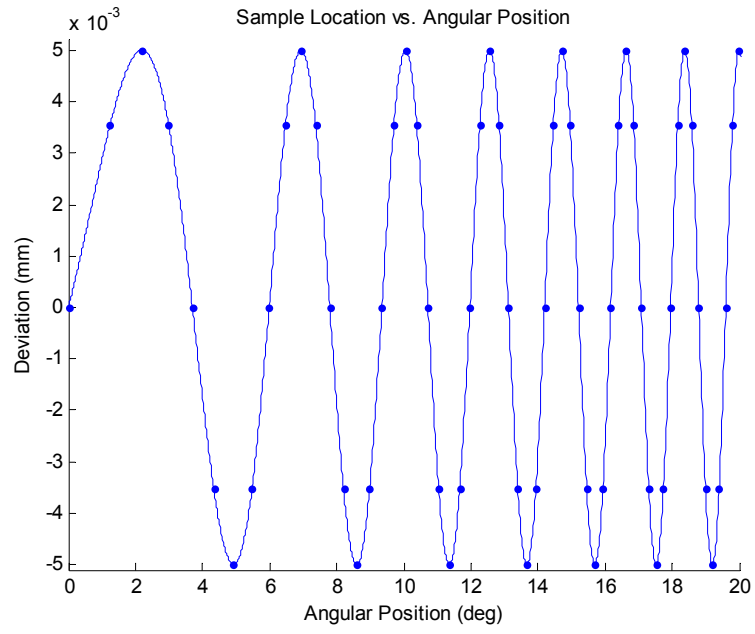


Figure 3.6: Constant number of calibration points per wavelength

(b) 8 points



(c) 32 points

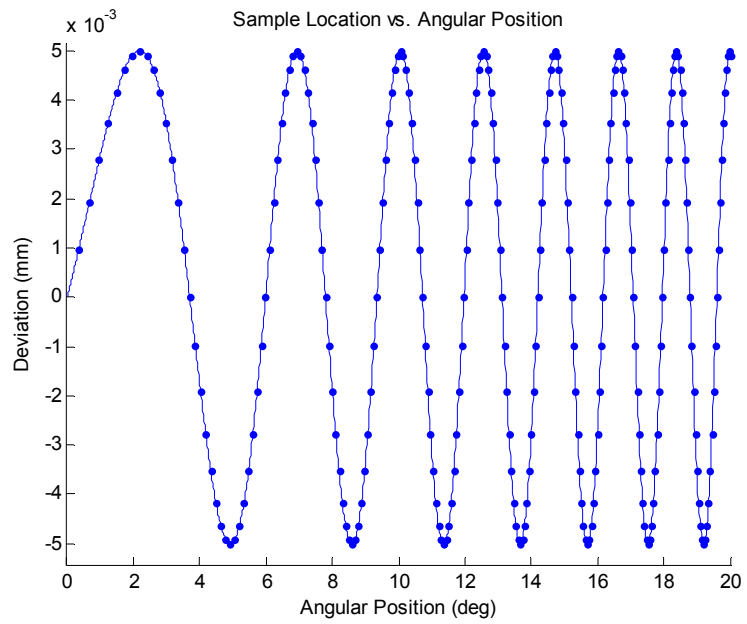


Figure 3.6: Continued

As shown in Figure 3.6, increasing n increases the density of the sampling at the maximums and minimums of the wave. Since this information will degrade during scanning and will be critical in measurements of the ring and modeling scanning performance, it is desired to have the largest n that will be feasible during the calibration measurement. There are 840 waves on the circumference of the ring. The M-48 takes 11 seconds to measure one point. Therefore, measurement time limits the calibration. Based on previous experience, it is unreasonable to expect the measurement environment to stay within specification continuously for more than a few days. Table 3.1 lists the number of points per wave and the time that would be required for calibration of the inside or outside surface. As shown in Table 3.1, with 32 points per wave, the measurement of each circumference will take 82.4 hours or 3.4 days. Thirty-two points per wave was selected as the maximum achievable density. As shown in Figure 3.6c, this density also provides excellent sampling coverage of each wave and will allow satisfactory reconstruction.

Mathematically, this can be achieved for a quadrant of the ring by setting the inner argument of the sine function in Equation 3.1 equal to the incremental length as shown in Equation 3.4, namely

Table 3.1: Hours required for calibration as a function of points per wave

Points per wave	Time for inside or outside calibration (hrs)
4	10.3
8	20.6
16	41.2
32	82.4
64	164.8

$$dt^2 + f_b Lt = aL^2 \quad (3.4)$$

where

$$a = 0, \frac{1}{2^n}, \frac{2}{2^n}, \dots, (i - \frac{1}{2^n})$$

and i = integer number of waves in one quadrant.

The positive root of this polynomial is the circumferential length location of the sampling point. Equation 3.5 can be used to convert this length to an angular location, θ , given by

$$\theta = \frac{t}{R_{\text{theor}}}, \quad (3.5)$$

where R_{theor} = theoretical inner or outer radius of the ring.

The MATLABTM program that executes this algorithm and generates the angular locations of the calibration points for the inner and outer surfaces is given in Appendix 1. The portion of code in this program that defines the theoretical waveform given in Equation 3.1 was developed by North Carolina State University [48]. MATLABTM is a matrix based mathematical software package.

3.4. Calibration procedure

A calibration procedure was developed to measure the wavy ring per the drawing given in Figure 3.3. This section will detail the calibration procedure. The required equipment

includes the wavy ring artifact, the probe configuration, epoxy and cotton swabs for application, three posts, and the calibration sphere.

3.4.1. Probe selection

Two probes are required for calibration of the wavy ring artifact because both the top of the ring, Datum A, and the waves on the outer and inner surfaces of the ring must be measured. Because of the low uncertainty desired in the measurement of the waves, a probe oriented normal to the surface is desired. Yet this horizontal probe configuration would not allow Datum A to be probed. An indexable probe should not be used in this application due to the introduction of repeatability errors and the extra flexibility that exists in the joints of this probe type. Instead it is desired to have two probe tips on one probe configuration. The two most common probe materials are tungsten carbide and industrial ruby. The advantage of the ruby tip is that it generally has a better roundness. However, this tip must be glued on to the probe shaft and is therefore not as durable. The tungsten carbide tip and shaft are ground as an integral component thus providing more durability. In both the calibration and the later experimentation with the ring, the probe will remain in the same nominal location while the ring turns on the rotary table. During the calibration, only a small spherical arc of the probe surface will contact the part, and the durability advantage of the tungsten carbide outweighs the roundness disadvantage. A small 0.4 mm diameter tip probe will be used for calibration of the waves, while a larger 3 mm diameter probe tip will be acceptable for measurement of Datum A. The probe configuration selected is shown in Figure 3.7.

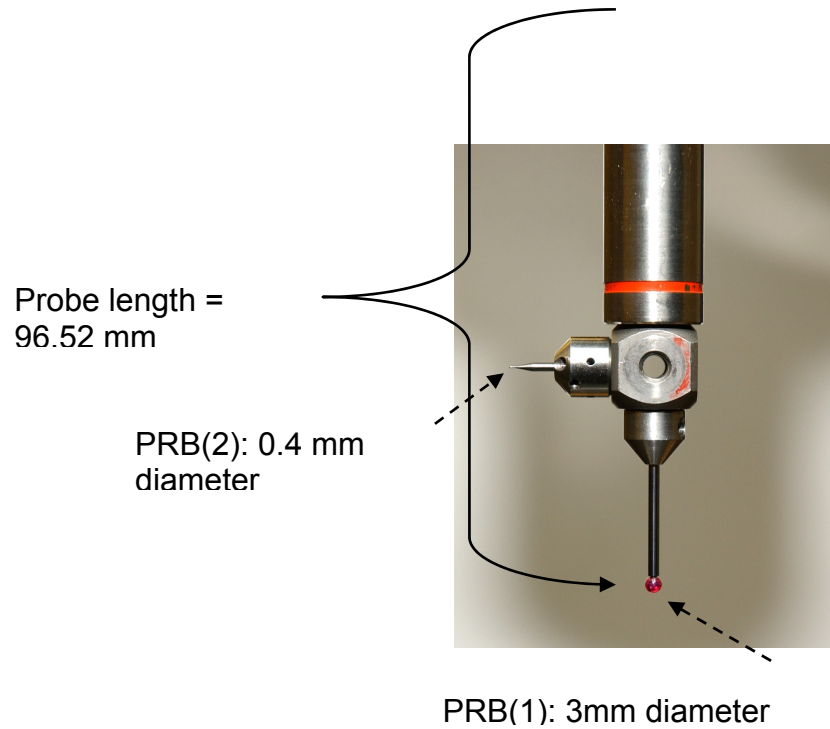


Figure 3.7: Probe configuration

The small horizontally mounted probe tip is desired to be as large as possible for durability yet small enough to fit into the shortest wavelength wave. Mathematically this means that the probe radius must be smaller than the radius of curvature at every point.

For each point on the ring, the radius of curvature R is defined by Equation 3.6; namely,

$$R = \frac{1}{\kappa}, \quad (3.6)$$

with the curvature κ defined by

$$\kappa = \frac{d\phi}{dl} = \lim_{\Delta l \rightarrow 0} \frac{\Delta\phi}{\Delta l}, \quad (3.7)$$

where ϕ is the tangential angle and l is the arc length as shown in Figure 3.8 [52].

Therefore,

$$\phi = \arctan\left(\frac{\Delta l}{\Delta t}\right) \quad (3.8)$$

where Δt is the incremental distance between calibration points and

$$\Delta l = \frac{L}{m} \quad (3.9)$$

where L is the length of one quadrant of the ring and m is the number of points in one quadrant assuming points are equally distributed about the circumference instead of distributed equally per wave. The results show that the minimum radius of curvature is

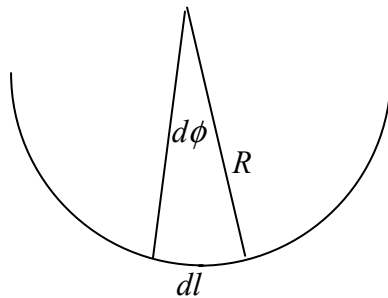


Figure 3.8: Radius of curvature

theoretically 0.4396 mm. Therefore, a 0.4 mm diameter tip with a 0.2 mm radius will be appropriate for calibration.

3.4.2. Fixturing method

The fixturing method must assure that no stresses are induced that would deform the ring. Therefore, an adhesive bond is preferred to bolting the ring to a fixture. A quick-setting epoxy was selected that is easily removed. Additionally, epoxy should only be applied to the edges of the adjoining surfaces and not between them because that would introduce a non-flat surface that would not yield a stable measurement surface.

3.4.3. Calibration steps

The first step is to clean the ring and probes with alcohol and a dust-free cloth. Alcohol is used as a cleaning agent because it evaporates quickly and will not create thermal gradients in the artifact. A dust-free cloth is required because at this level of accuracy, dust on the probes or artifact will be visible in the measurement results.

The probe calibration routine is pre-programmed such that only one clearance point is required before taking one probing point at the top of the calibration sphere with the 3 mm tip. The calibration program is given in Appendix 2. The calibration for the 0.4 mm tip is also pre-programmed to run automatically. The calibration requires a 15.875 mm diameter calibration sphere as shown in Figure 3.9. For this program, the calibration

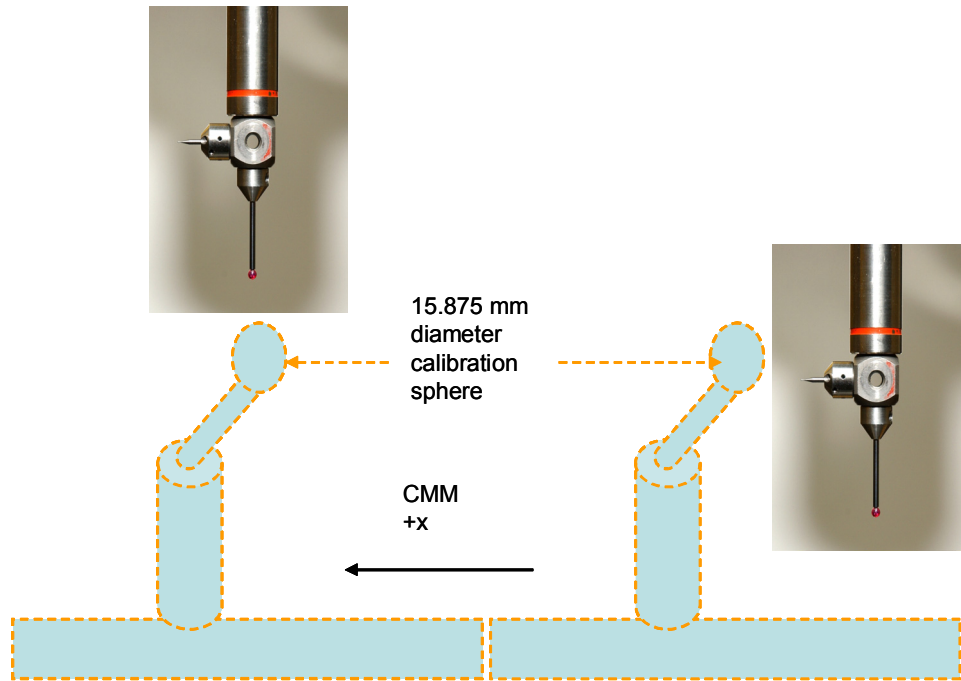


Figure 3.9: Probe calibration

sphere and probes must be configured as shown in Figure 3.9. Next, the rotary table must be calibrated. This calibration measures a calibrated sphere at multiple angular positions of the rotary table in order to establish a coordinate system based on the center of rotation of the rotary table.

The manual set-up must then be conducted to determine an initial coordinate system based on the actual location of the ring. The ring was fixtured as shown in Figure 3.10 with glue at the top and bottom of the three posts. In order to take advantage of the symmetry of the ring, it was centered within 50 micrometers radial run-out on the rotary table. The epoxy must set for 45 minutes before the calibration can continue. The posts should be mounted approximately 120 degrees apart as shown in Figure 3.11 for

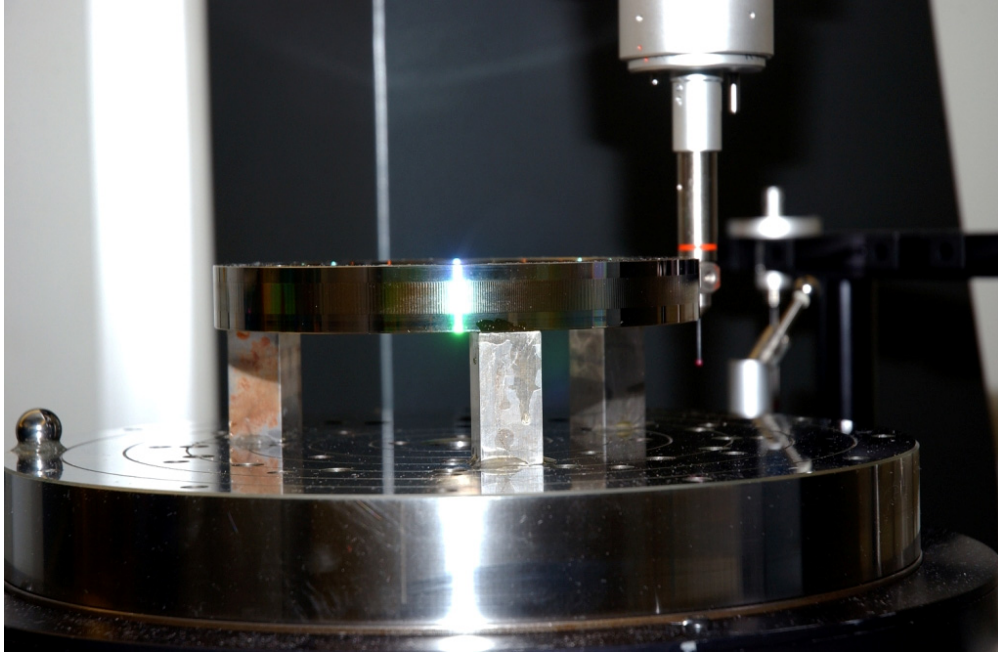


Figure 3.10 Ring fixturing

maximum stability. The orientation of the ring on the fixture is important for the establishment of the coordinate system. It is conceptually simpler if the coordinate system on the ring is nominally in agreement with the directions of the axes of the rotary table coordinate system when the rotary table is at zero degrees. This consistency allows the calibration program to be re-usable instead of being re-written for a randomly selected ring orientation.

The initial ring coordinate system has the x -axis of the part, x_{part} , directed from the center of the ring through the angular reference location “2” shown in Figure 3.11 with the positive z -axis, z_{part} , normal to the top of the ring and pointing up. The orientation of the part coordinate system axes are approximately the same as the orientation of the machine coordinate system axes. Only the origins of the coordinate systems differ significantly.

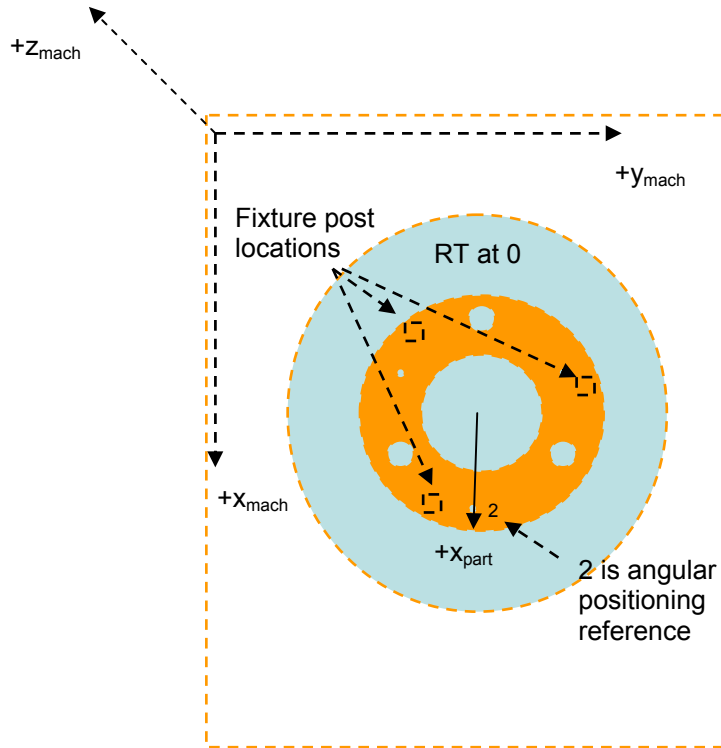


Figure 3.11: Ring orientation and fixture post locations

To obtain the necessary data to establish this part coordinate system, three probing points are first taken on the top of the ring with the 3 mm tip. To establish the center of the ring and the origin of the coordinate system, three probing points are taken on the smooth inside diameter of the ring between the top and wavy surfaces as shown in Figure 3.12. To determine the position of the angular reference location “2”, four points are taken inside the 6.35 mm bore hole next to the etched 2 as shown in Figure 3.13.

Next, the part coordinate system is refined by automatically re-measuring the same features. In order to execute the automatic part coordinate system, the probe only needs to be moved to any position over the ring because the location of the features of the ring have been determined to a reasonable level of accuracy through the manual part

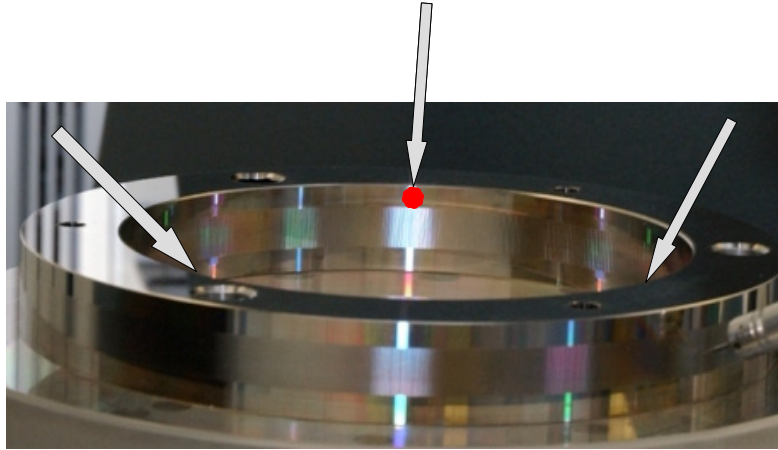


Figure 3.12: Manual set-up probing point to determine center of ring

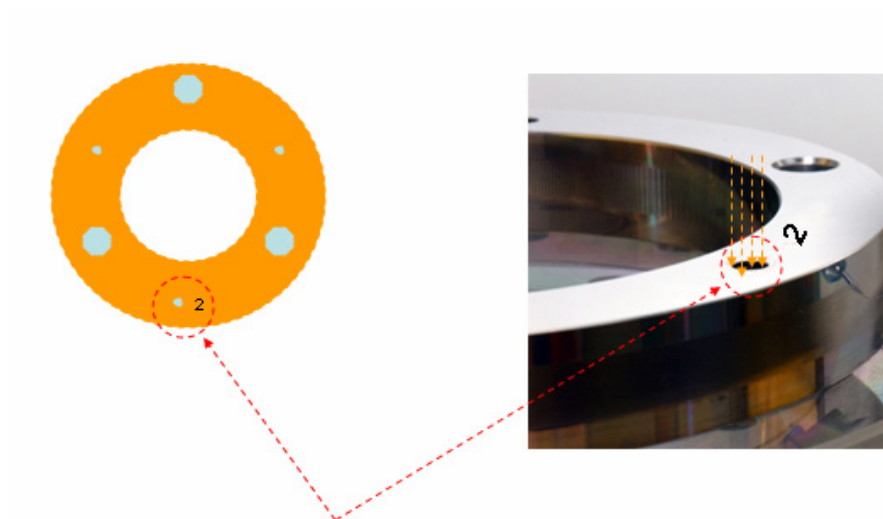


Figure 3.13: Manual set-up probing points to determine angular reference location

coordinate system measurements. The automatic part coordinate system must be of the lowest uncertainty, so the epoxy must cure for a total of two hours from application before the automatic part coordinate system determination can begin.

Both Cartesian and cylindrical coordinate systems are established automatically on the ring. The calibration measurement is made in the cylindrical coordinate system. First, the inside circumference is measured. The 0.4 mm tip is used for this actual calibration of the waveform.

The location of the waveform given in Figure 3.2 was experimentally determined with respect to the angular reference location. It was measured to be 8.7974 degrees from the reference location for the inside surface and 6.6549 degrees from the reference location for the outer surface for Ring 2. Ring 2 is the ring being used as the primary standard. For Ring 1 which will later be used as a secondary standard, different rotations are required to agree with the waveform machined on Ring 1. The cylindrical coordinate system is then rotated by this amount so that the 0 angle aligns with the beginning of the longest wavelength on the ring as shown in Figure 3.2.

The angular locations that will allow 32 points to be measured on each wave as shown in Figure 3.6c are now imported. There are 840 waves on the circumference of the ring which therefore requires 26880 points to be measured during the calibration nominally along a circular path. The calibration points are then established 12.5 mm down from the top of the ring. The measurement of the ring to establish the calibrated values is then

made, and the data is saved. The process is repeated for the outside circumference yielding all the data required for the calibration. A sample of the calibration data points is shown in Figure 3.14.

3.5. Primary standard calibration results

NIST collected this data using the method described in Section 3.4. NIST made one modification to the calibration program which rotated the coordinate system by 180 degrees about z_{part} . Therefore, the NIST data must be rotated 180 degrees to match the theoretical waveform. Once the raw data was collected, it was corrected by NIST to account for atmospheric pressure fluctuations and a closure error that occurred during the

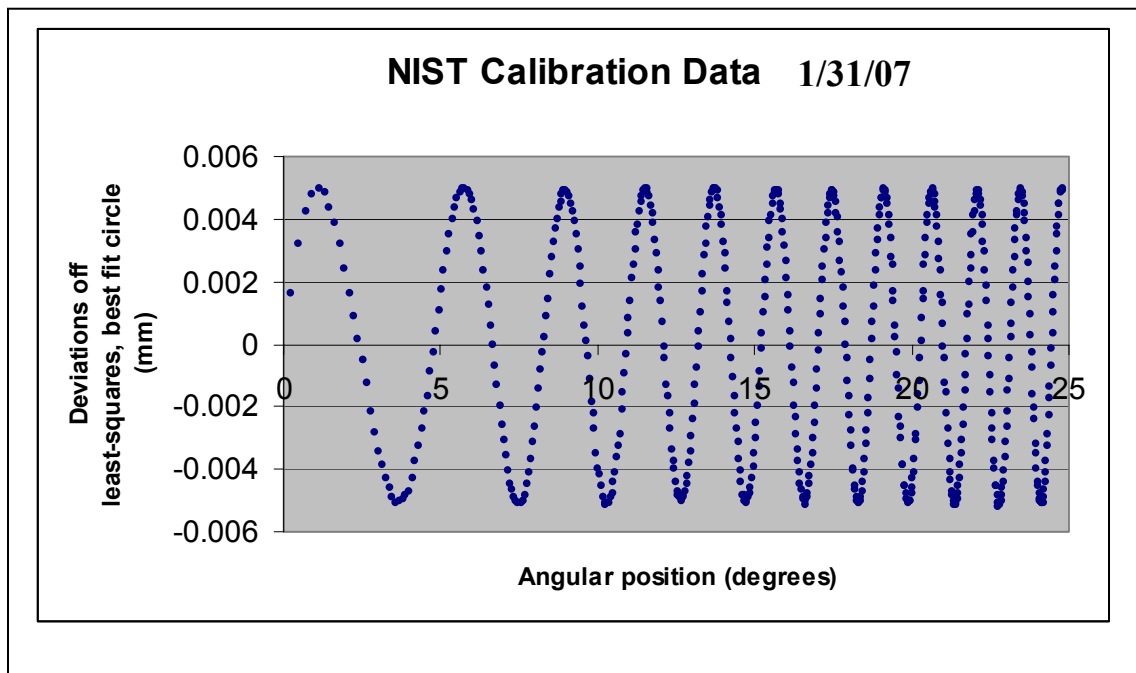


Figure 3.14: NIST calibration data

measurement. This gave an inner radius of 76.11564 mm and an outer radius of 101.71266 mm. Then a circle was re-fit to the corrected data which yields a final calibrated inner radius of 76.116036 mm and a calibrated outer radius of 101.71315 mm. Then, the calibration data is reported as the deviation from this best fit circle at a given angular location. The uncertainty in this measurement result is given in the official NIST calibration report shown in Appendix 3.

The uncertainty was calculated by the method described in the Guide to the Expression of Uncertainty in Measurement [3,4]. The expanded uncertainty, U , with a coverage factor of $k=2$ was calculated to be $\pm 0.382 \mu\text{m}$. As described in the calibration report, this uncertainty accounts for eight primary error sources as shown in Table 3.2. The profile toleranced in Figure 3.3 coupled with the uncertainty statement provided by NIST yields a region in which each point is expected to lie with 95% certainty as shown in Figure 3.15. It should be noted that the choice of measurand eliminates differences between the

Table 3.2: Components of ring uncertainty statement

Item	Description
1	Machine positional and laser scale uncertainty
2	Historical length reproducibility of calibrated artifacts
3	Laser wavelength compensation
4	Thermal expansion coefficient and thermometer reading
5	Difference in contact deformation between probe and calibration sphere and probe and artifact
6	Uncorrected atmospheric pressure fluctuations during data collection
7	Closure error for 360 degree rotational data sets due to drift
8	Rotary table mechanical errors and length errors from radial positioning uncertainty

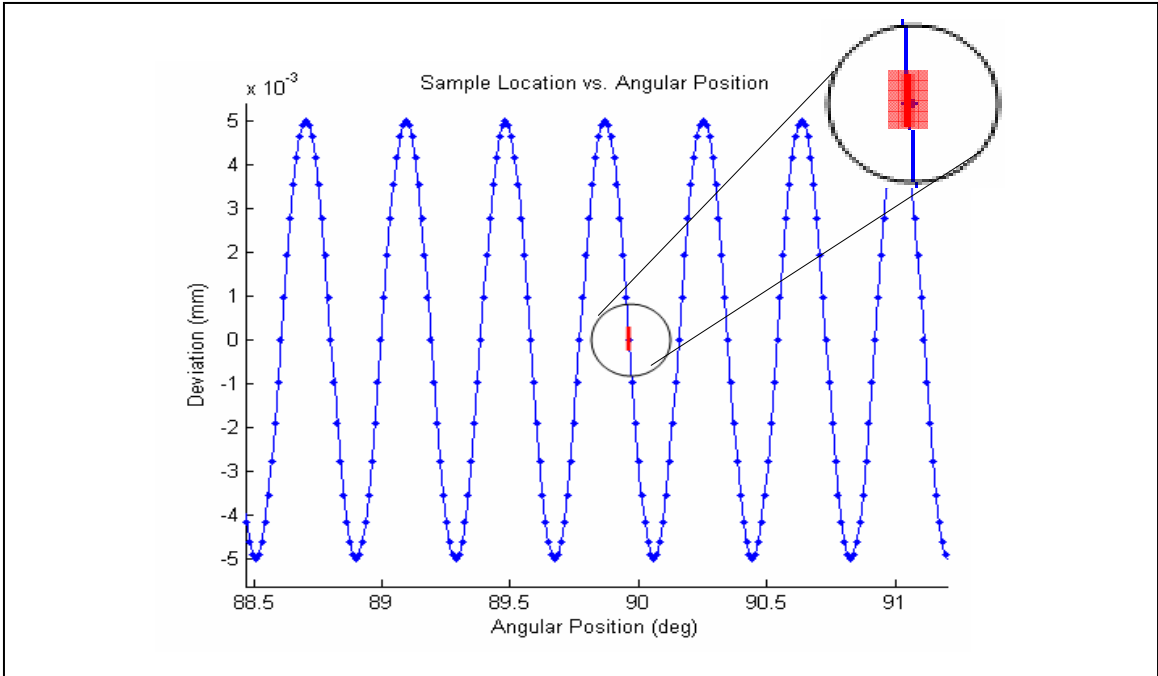


Figure 3.15: Uncertainty region for a probed point

mathematical definition of the waveform and the manufactured waveform as a source of uncertainty.

As shown in Figure 3.15, the uncertainty is more significant in the direction of the deviation since the bounds of the deviations are $\pm 5 \mu\text{m}$. In contrast, the uncertainty is less significant along the angular positioning axis since the length of a half degree segment of the inner radius is $664 \mu\text{m}$. This is the reason that the square uncertainty region appears as a line when drawn to scale in Figure 3.15. The resulting uncertainty region is highlighted in the circle in Figure 3.15 for a probing point in the highest frequency area of the wave.

4. Experimental Work

The purpose of the experimental work is first to isolate the key parameters that influence CMM scanning performance and then to provide data that can be used to generate and validate a model, or characterization, of a CMM. This model will then be used to select appropriate scanning parameters for a given application.

4.1. Experimental parameter selection

Based on the literature and industrial practice, the following factors are known to be of primary influence in scanning CMM measurements: probe tip diameter, the use of a rotary table, probing force, artifact orientation, filter characteristics, and scanning speed. The goal of this project is to provide a means of selecting appropriate values for these parameters. This section describes the parameters which can be selected. The following section describes the experimental setup including the specific parameter values used in this project.

4.1.1. Probe tip diameter

During a scan, the probe tip should remain in contact with the surface of the artifact at all times. Therefore, the probe tip diameter must be selected based on the level of detail to be measured. As described in Section 3.4, the probe radius must be less than the minimum radius of curvature of the surface which is 0.4396 mm in order to allow

measurement of the shortest wavelength. Therefore, a 0.5 mm diameter tip, shown in Figure 4.1, was selected because the tip radius of 0.25 mm is within the radius of curvature limits. A 0.5 mm diameter tip made of industrial ruby was used in the experiments because during the experimental scans unlike during the calibration, a large area of the probe tip will contact the surface during the scan since each scanned point is not measured normal to the surface. Therefore, the roundness provided by the industrial ruby tip is important. The 0.5 mm diameter tip is the smallest ruby tip that is commonly used in industry because the glue that holds the tip to the stylus is fragile due to a contact area of only 0.071 mm^2 . The tip breaks off easily with smaller diameter tips.

4.1.2. Rotary table

A rotary table provides a rotational axis to a CMM and is computer controlled with the other axes. Precision rotary tables are used to increase the precision of the measurement of an axisymmetric workpiece. The advantage of a rotary table is that when a workpiece is placed on the table, the measurement capability is improved by eliminating the motion of machine translational axes. This is accomplished by leaving the probe in a fixed

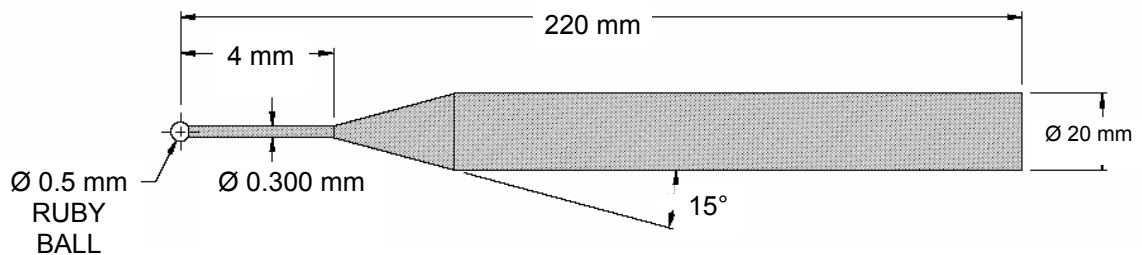


Figure 4.1: Probe used in experimentation (used with permission of Carbide Probes)

position and rotating the workpiece to reach the next measurement location. One measure of the accuracy of a rotary table is the total indicator run-out. The total indicator run-out is the difference in the maximum and minimum deviations measured from the least-squares best fit circle. This test measures how well the center of the rotary axis can be found. Precision rotary tables are constructed of stainless steel, weigh hundreds of pounds, and use air bearing spindles in both the radial and thrust planes. The accuracy that can be realized is due not only to the mechanical accuracy of the table itself, which can have a radial error as low as 0.0508 micrometers, but also to the precision of the rotary table calibration, which determines the orientation of the axis of rotation and the location of the center of rotation. Since this application is of the highest precision, a rotary table was used in all experiments as shown in Figure 4.2.

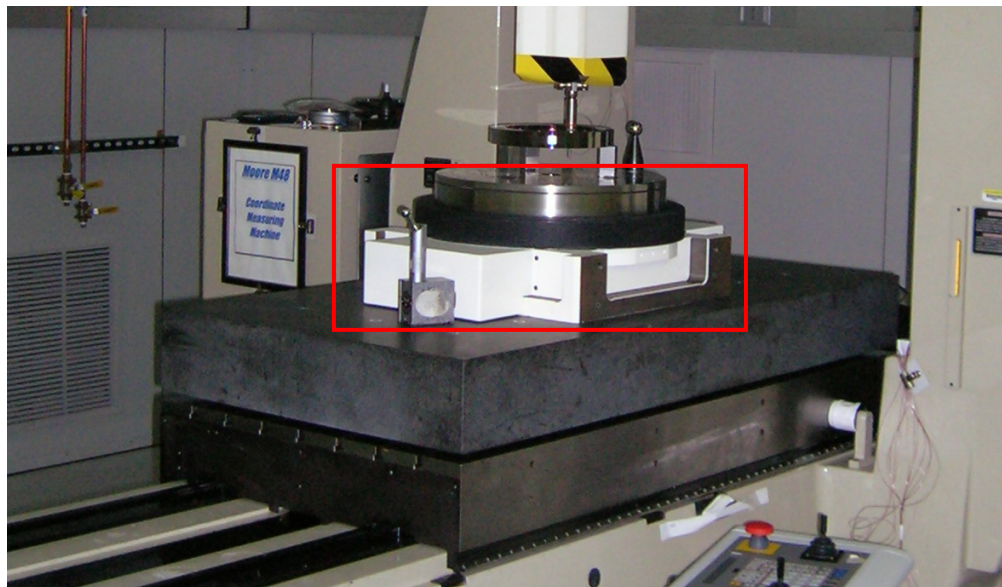


Figure 4.2: Rotary table

4.1.3. Probing force

During scanning, the control system attempts to maintain the probing force at a set point. This set point is selected based on the measurement application. The control system actually monitors the deflection of the probe from its nominal position via linear variable displacement transducers (LVDTs). This deflection can be converted to a force through the spring equation

$$F = k_{sc} d_{ph} , \quad (4.1)$$

where

F = scanning force (Newtons),

k_{sc} = spring constant (Newtons/mm), and

d_{ph} = deflection of probe head (mm).

The system monitors this deflection during measurements and will present a system error if the deflection boundaries are exceeded. This error would indicate that a constant scan has not been achieved. For scanning, a low force set point, corresponding to small deflections, is desired because the system would not respond quickly enough to all the waves encountered on the ring if the force were set higher. CMM manufacturers typically provide several parameter sets with differing scanning force set points. The lowest force parameter set available that allows for reasonably fast scanning was selected for this application.

4.1.4. Artifact orientation

Artifact orientation is a key parameter in influencing scanning measurements. The orientation of the workpiece with respect to the CMM determines which axes are used during a measurement. Commonly, artifacts are oriented along machine axes to facilitate interpretation of results, but many orientations are physically achievable. For high precision measurements, it is desirable to minimize the axes used. As described in Section 4.1.2, a rotary table, which must be placed flat on the graphite surface plate of the CMM, minimizes the motion of the machine axes. In order to allow for the use of the rotary table as the only motion during measurement, the artifact must be placed in the plane of the face of the rotary table in a horizontal orientation. The horizontal orientation also allows the entire ring to be scanned with a single probe tip. Other configurations, such as a vertical orientation, would not meet these criteria and also would not allow for the use of a rotary table but would instead require movement of the translational axes. Based on this information, the horizontal orientation was selected for all experiments with the wavy ring.

The ring is ideally centered with the center of the rotary table. This positioning will allow the probe to stay within the deflection boundaries described in Section 4.1.3 while measuring all the waves. The experimental methods and data analysis techniques developed with the ring in a horizontal orientation are applicable for tests conducted with the artifact in other orientations as well.

This orientation also minimizes the fixturing required as the ring can be placed directly on the faceplate with no fixturing. Fixturing is not required because the ring and faceplate of the rotary table are so flat that they can be wrung together. Wringing is possible due to the adhesion of the thin film layer of moisture between surfaces and the molecular attraction of the surfaces [53]. Fixturing could induce stresses and deform the ring. If the ring were fixtured in a vertical orientation, fixturing errors could also lead to movement of the ring during measurements and to invalid results.

4.1.5. Environmental parameters

The purpose of these experiments is to determine how to select scanning parameters for scanning measurements made in a well-controlled environment. It is assumed that the inspection area in which high precision measurements would be made would have environmental parameters that are conducive to good measurements. Specifically, the temperature and vibration should be well controlled. It is assumed that any variation in environmental parameters that are within operating bounds would not impact the results of scanning the wavy ring.

Temperature variations lead to thermal expansion based on the coefficient of thermal expansion. The coefficient of thermal expansion for the ring, which is made of 17-4 PH stainless steel, is $10.8 \mu\text{m}/\text{m}\cdot^{\circ}\text{C}$ [48]. Therefore, in the analysis of the deviations of the surface from the best-fit circle, the $10 \mu\text{m}$ peak-to-valley would experience an increase of

$10.8 \times 10^{-5} \mu\text{m}$ for a 1°C increase in temperature. A typical operating range is $20^\circ\text{C} \pm 1^\circ\text{C}$, so the effect on the waves is negligible.

The CMM is designed so that resonance frequencies are not excited under typical measurement conditions. System vibrations are tested for during CMM certification tests performed at regular intervals. During these tests, the scanning performance of a CMM is typically validated using a smooth artifact. If the data is smooth, then vibrations are not confounding the scanning results.

In order to determine whether the waves will excite vibrations in the system, unidirectional tests that had been previously conducted on the probe head to determine the natural frequency of the probe head were studied. Since the wavy ring experiments were conducted with the head probing in the x-direction, this plot is shown in Figure 4.3. This plot was generated by inputting an impulse to the system and watching the movement of the LVDT until it settles. From Figure 4.3, the natural frequency can be calculated as described below. The damped period, T_d , can be calculated from the plot as 0.117 seconds. This data can then be used to calculate the damped frequency given by

$$\omega_d = \frac{2\pi}{T_d} = 53.7024 \frac{\text{rad}}{\text{sec}}, \quad (4.2)$$

where

ω_d = the damped frequency (rad/sec) and

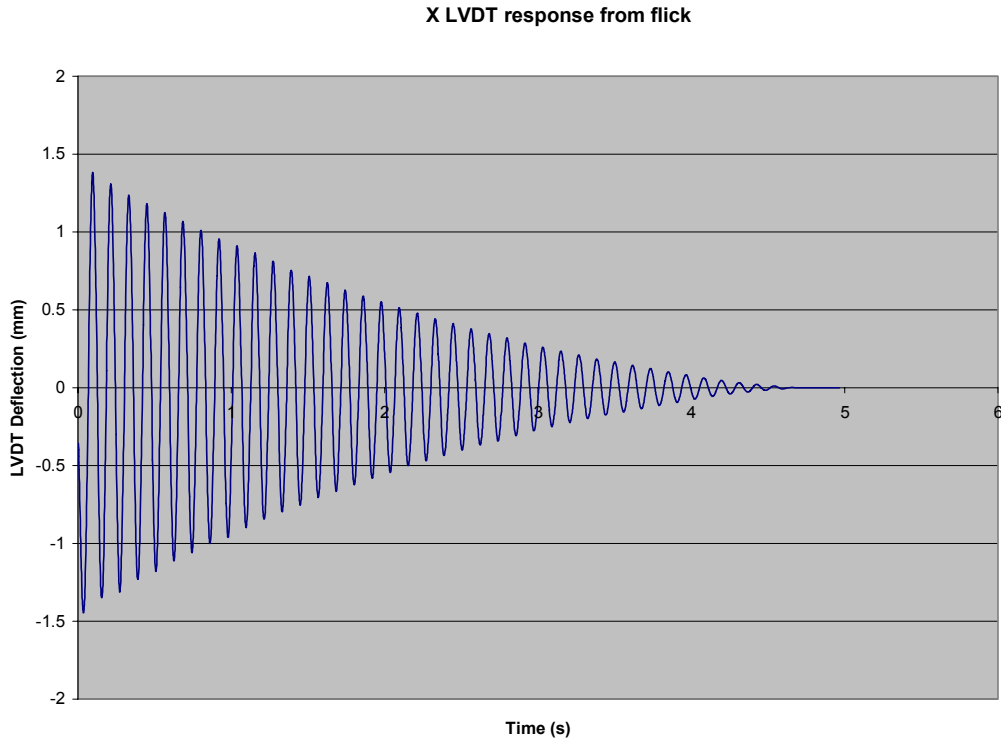


Figure 4.3: Probe head natural frequency in x-direction

T_d = the damped period (sec).

The LVDT can be approximated as a second-order mass-spring-damper system. It is known that the decay curves for the impulse response of this system type [54] are bounded by curves given by

$$y_b = 1.5 \cdot \exp\left(\frac{-\zeta \omega_d t}{1 - \zeta^2}\right), \quad (4.3)$$

where

y_b = deflection boundary curve (mm),

ζ = damping ratio,

t = time since impulse (sec), and

where the 1.5 mm amplitude is determined from the initial conditions as shown in Figure 4.3. The damping ratio is defined as the ratio of actual damping to critical damping.

The coordinates of the experimental data point at the first peak were extracted as $(t, y_b) = (0.09638 \text{ sec}, 1.38073 \text{ mm})$. After some algebraic manipulation, Equation 4.3 can be solved to yield a damping ratio, $\zeta = 0.016$. This value in conjunction with the damped frequency can be used to solve for the natural frequency, ω_n , of the system via Equation 4.4, and given as

$$\omega_n = \frac{\omega_d}{1 - \zeta^2} = \frac{53.7024 \frac{\text{rad}}{\text{sec}}}{1 - 0.016^2} = 53.7162 \frac{\text{rad}}{\text{sec}}. \quad (4.4)$$

In cycles per second, this is 8.55 Hz. Ideally, this frequency should be avoided during scanning measurements. However, if this frequency is expected based on the surface characteristics, this vibration must be considered as a possible source of disturbance in the data. If the wavy ring data are not noisy, it can be determined that these vibrations are not an issue. Regions of noisy data outside the probe head natural frequency could also be due to the interaction of the probe tip and the surface generating noise in the system.

4.1.6. Scanning speed

Scanning speed is measured in mm/s and describes the linear speed of the probe relative to the workpiece. This speed can affect the measurement result if the speed exceeds the following capability of the control system for the feature being measured. This project seeks to determine an experimental means of determining a maximum scanning speed. Therefore, in these experiments the speed was varied from a low of 0.5 mm/s to the maximum speed achievable for the wavy ring, which was experimentally determined to be 11 mm/s.

4.1.7. Filter characteristics

A digital filter is used to process raw scanning data. This filtering is critical because it can remove or obscure information that is actually on the workpiece surface. This filter is often proprietary but must be characterized in order to correctly select filter parameters and understand these filtering effects. Therefore, during these experiments, the user selectable low-pass filter cut-off frequency is varied in order to accomplish these goals. The range of cut-off frequencies that should be considered must be selected based on the expected wavelengths on the surface of a workpiece and the range of scanning speeds as shown in Equation 4.5; namely, the input frequency f_i is given by

$$f_i = \frac{v}{\lambda}. \quad (4.5)$$

When the scanning speed, v , is given in mm/s and the wavelength, λ , in mm, the units of frequency are Hz. Since the scanning speed varies from 0.5 mm/s to 11 mm/s as described in Section 4.1.6 and the wavelengths present on the ring vary from 0.531 mm to 6.24 mm, the range of frequencies encountered as inputs to the system can be calculated using Equation 4.5 and are shown in Table 4.1. Based on this data, cut-off frequencies of 2, 3, 5, 10, 100, and 200 Hz are tested. These cut-off frequencies allow the data to be filtered at different points and sometimes not at all. This range of data allows filtering effects to be studied.

4.2. Experimental setup

The experimental set-up is shown in Figure 4.4. The CMM is a Leitz PMM with a B4 controller, a TRX probe head, and a rotary table. The temperature control for the area is

Table 4.1: Range of frequencies in ring based on scanning speed and wavelength

Speed (mm/s)	Wavelength = 6.24 mm	Wavelength = 0.531 mm
0.5	0.08 Hz	0.94 Hz
1	0.16 Hz	1.88 Hz
2	0.32 Hz	3.77 Hz
3	0.48 Hz	5.65 Hz
3.5	0.56 Hz	6.59 Hz
4	0.64 Hz	7.53 Hz
4.5	0.72 Hz	8.47 Hz
5	0.80 Hz	9.42 Hz
6	0.96 Hz	11.30 Hz
7	1.12 Hz	13.18 Hz
8	1.28 Hz	15.07 Hz
9	1.44 Hz	16.95 Hz
10	1.60 Hz	18.83 Hz
11	1.76 Hz	20.72 Hz

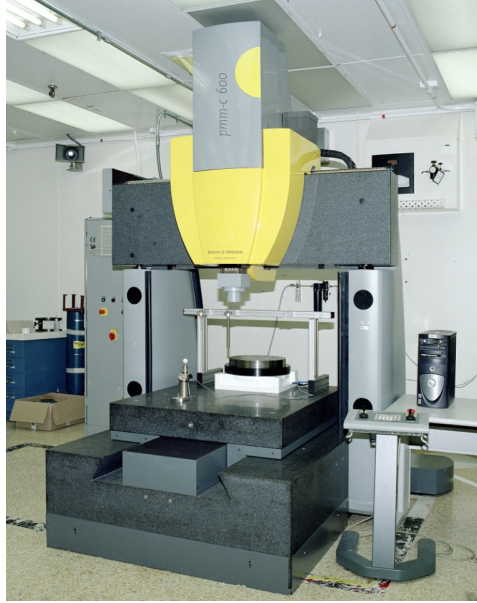


Figure 4.4: Leitz CMM

20±1 °C. This type of CMM has a moving table design with air bearings on the guide ways. The machine volume is created by axes that are approximately 1200 mm, 700 mm, and 700 mm in length. The permitted load is 4400 pounds. The probing force can range from 0.1-1.2 Newtons. The maximum positioning speed is 400 mm/sec. As described in Section 4.1.5, the probe head has a natural frequency along the x-axis, which is the longest axis along the granite, of 8.55 Hz. Collision protection is built into the system. This system is equipped with an automatic probe changer. This CMM has a Volumetric Length Measurement Error of $0.6 + L/600 \mu\text{m}$ per ISO 10360-2 [30]. That means that at the farthest reach at 1200 mm, the volumetric accuracy is 2.6 μm .

The rotary table is an A.G. Davis Ultraron that has a 36000 line count encoder to provide rotational increments of 0.001°. On the inside diameter of the ring, which was used for

the majority of the experiments, this gives a radial positioning capability of 1.33 μm . The radial positioning uncertainty is lower for objects of smaller radius. Typical certification for this rotary table gives a 0.005 mm radial error motion. The certification test positions a single sphere on the rotary table and measures the radial error.

The CMM user-interface software Quindos [55] is on a PC with Windows XP. Quindos is used to develop inspection routines and evaluate data for the CMM and has a database structure. Quindos also contains a powerful geometric analysis engine. The system is configured so that commands generated in Quindos are sent through the controller to the CMM. Data collected on the CMM are then sent back through the controller to Quindos and the operator.

For the experimentation, the Low Force Probing Set was used. An Ultra-Low Force Probing Set exists but is only appropriate for perfectly smooth surfaces. On textured surfaces, the ultra-low force would be insufficient to maintain contact with the surface of the workpiece. Therefore, the Low Force Probing Set is selected. When the probe is within a deflection window of $30 \pm 20 \mu\text{m}$, probing points are continually taken at the selected data acquisition rate which is selected on a points/mm basis, up to the maximum data collection rate of 250 points/second. The scan acceleration is set to 3 mm/s^2 .

During experimentation, the ring is placed horizontally on the faceplate of the rotary table. No fixturing is required. In the probe configuration used, as shown in Figure 3.1, the probe is held at a 45-degree angle to provide clearance for the probe head. The ring is

not mounted on posts because this fixturing might introduce instabilities under the scanning force. The probe tip diameter used in all scanning experiments is 0.5 mm. The implemented probe configuration is shown in Figure 3.1.

4.3. Experimental procedure

A range of scanning speeds and filter cut-off frequencies was tested as shown in Table 4.2 based on the considerations stated in Sections 4.1.6 and 4.1.7. These experiments were used to determine the performance effects due to changes in scanning speed and filtering. In Table 4.2, every combination of speed and filter cut-off frequency was tested on the inside diameter of the ring. The shaded cells represent the tests that were conducted on the outside of the ring. Tests were focused on the inside of the ring because

Table 4.2: Speeds and filter cut-off frequencies tested

Speed (mm/s)	Cut-off Frequencies Tested					
	2 Hz	3 Hz	5 Hz	10 Hz	100 Hz	200 Hz
0.5	X	X	X	X	X	X
1	X	X	X	X	X	X
2	X	X	X	X	X	X
3	X	X	X	X	X	X
3.5	X	X	X	X	X	X
4	X	X	X	X	X	X
4.5	X	X	X	X	X	X
5	X	X	X	X	X	X
6	X	X	X	X	X	X
7	X	X	X	X	X	X
8	X	X	X	X	X	X
9	X	X	X	X	X	X
10	X	X	X	X	X	X
11	X	X	X	X	X	X

initial tests of both outside and inside diameters revealed that the results are similar on either surface. Therefore, the experiments focused on the inside diameter. Each combination of speed and cut-off frequency was tested with one full rotation of the ring measuring either the inner or outer diameter. This measurement is equivalent to multiple observations of a ring of constant frequency because each frequency occurs four times on the ring as it sweeps from low to high and back to low in each half.

A Quindos program given in Appendix 4 is used to conduct these experiments and collect the necessary data. This program is based on a scanning program created by Mattias Schubert of MTWZ in 2005. That initial code is significantly modified for this application.

4.3.1. Setup procedure

When the Quindos program is initialized, the Low Force Probing Set is selected for the probing force. The probes that are used are then calibrated. A 5 mm diameter tip straight down probe is first calibrated and then placed back in the probe changer. The 0.5 mm diameter tip on the 45-degree angle is next calibrated as shown in Figure 3.1. Finally, the rotary table is calibrated as described in Section 3.4.3.

Once the probes and rotary table are calibrated, the manual coordinate system is created. This coordinate system is measured with the 5 mm tip. It is generated by first probing the top of the ring to generate Datum A. The center of the ring is then determined by measuring the smooth section on the inside of the ring, and the center of the counterbore

located clockwise from the hole marked with a “2” as shown in Figure 3.11 is also measured at four points. These manual measurement points are projected onto the x_{mach} - y_{mach} reference plane. An axis is then created through the center of these two circles and is called the x_{part} -direction. The z_{part} -direction is normal to the Datum A plane, and the origin of the manual Cartesian coordinate system is established where the axis through the center of the ring intersects the plane on the top of the ring.

After the manual coordinate system has been established, an automatic coordinate system is then established. This coordinate system is generated with no manual intervention from the operator since the features were located during the determination of the manual coordinate system. This coordinate system will also measure more points per feature and is therefore more accurate. The automatic coordinate system differs from the manual coordinate system only in the orientation of the axes in the x_{mach} - y_{mach} plane.

The automatic coordinate system is rotated by 71.15 degrees about z_{part} so that the zero degree location on the x_{part} -axis lines up with one of the longest wavelengths. The scans will begin at the zero-degree location, and this should be at the longest wavelength where the slopes are the most gradual and therefore easiest on the scanning control system. The value of 71.15 degrees was determined experimentally by magnifying a plot of the waveform. This zero position is approximately 2.35 degrees counterclockwise of the zero used for the calibration. For comparison of the data, the measured data will be rotated to align with the calibration data. Next, both Cartesian and cylindrical coordinate systems are created. The Cartesian coordinate system will be used to develop the scan

path during the scanning experiments while the cylindrical coordinate system will be used during the actual scan and the data analysis.

4.3.2. Measurement Procedure

The following measurement procedure was used during each experimental scan:

1. Select 0.5 mm probe tip
2. Select Cartesian coordinate system
3. Select filter cut-off frequency
4. Select scan point density of 50 points per linear mm to provide a spacing of approximately every 20 μm
5. Generate scan path 12.5 mm down from the top plane of the ring in the Cartesian coordinate system and then transform into the cylindrical coordinate system for the actual scan
6. Scan ring
7. Change filter cut-off frequency
8. Run second experiment with the same speed and different filter cut-off frequency

4.4. Experimental results

For each point measured in the data set, the experimental results include the filtered coordinates of each point and the probe head deflections in the Cartesian directions.

When the ring is measured, no calculations are initially done to the data until the raw data

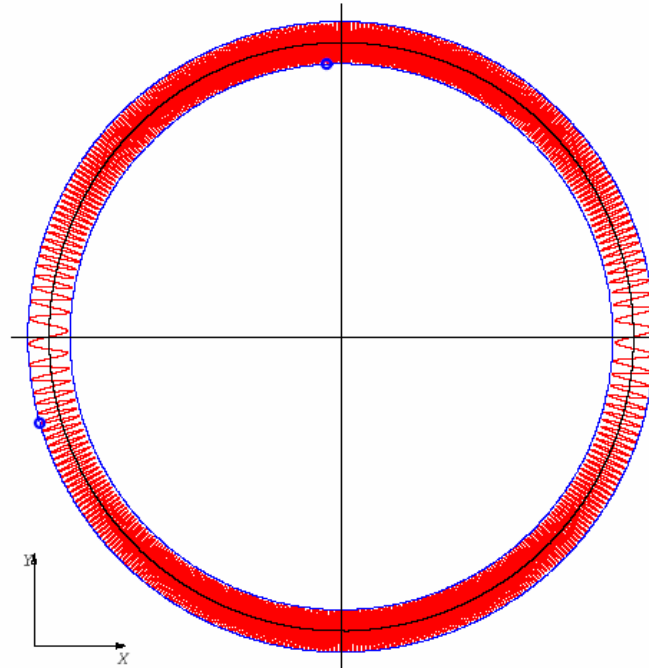
which contains the probe head deflections are saved to a different variable. Calculations are then performed on the raw data to determine the best fit radius and deviations from that radius for each scanned data point. A single scan generates approximately 23800 data points which translates to 60 MB of data. Data are collected for each of the experimental data sets shown in Table 4.2. The data has been archived and is available from the author. From each scan, the plots shown in Figure 4.5 are generated. Figure 4.5a shows the deviations from a least-squares circle and Figure 4.5b shows the scanning force variations during the scan.

4.5. Experimental data analysis

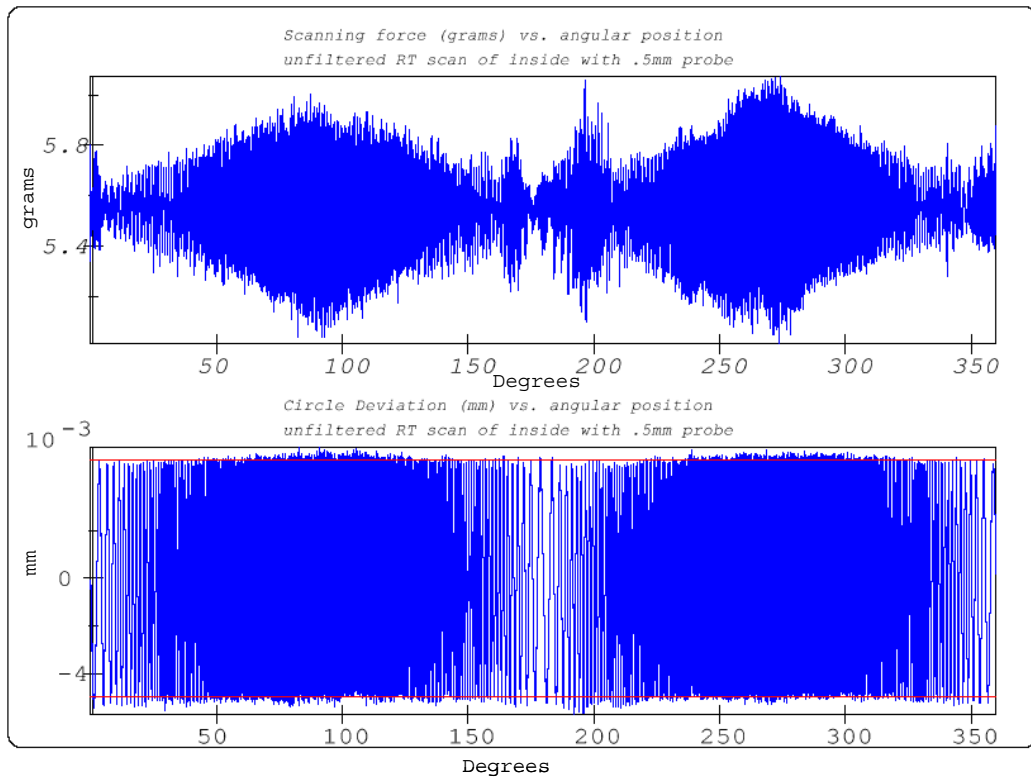
During experimentation, a preliminary, qualitative data analysis is performed. This analysis verifies that the anticipated dependencies among scanning speed, filtering parameters, and scanning performance are significant. This section details this analysis.

4.5.1. Scanning speed effects

In order to conduct an initial evaluation of the scanning performance, a roundness plot is generated. To create this plot the data are first transformed back into Cartesian coordinates to accommodate the Quindos roundness plotting routines. Once this is performed, a roundness plot is generated of the inside circumference of the ring measured in the $x_{\text{part}}-y_{\text{part}}$ plane. The deviations from the best fit circle are magnified by a factor of 1000 for plotting purposes. The plots for three representative cases of increasing



(a) Deviations off best fit circle



(b) Variation of scan force above deviations
 Figure 4.5: Experimental results per scan

speed are shown in Figures 4.6, 4.7, and 4.8. In each case, the plot shown is for a filter cut-off frequency of 200 Hz because no data filtering of the frequencies present on the wave occurs.

As seen from these plots, the probe has increasing difficulty following the contour of the ring as the speed increases. For the experimental speeds tested, a waveform close to the calibrated waveform is observed for slow speeds as shown in Figure 4.6. However, disturbances and discontinuities in the data are noted at higher speeds as shown in Figures 4.7 and 4.8. The roundness, or form of the circle, increases from 11.3 μm for the 0.5 mm/s case in Figure 4.6, to 18.1 for 7 mm/s in Figure 4.7, and finally to 68.8 μm for 11 mm/s in Figure 4.8.

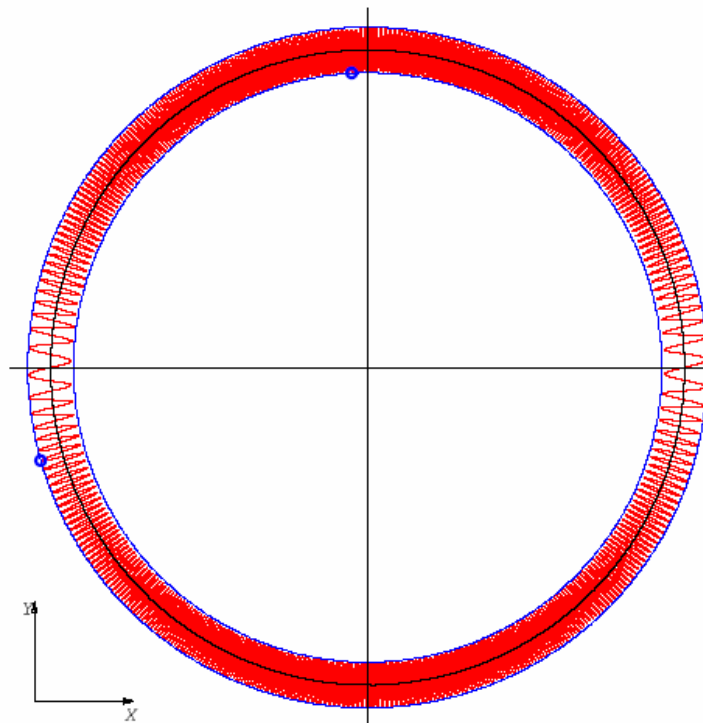


Figure 4.6: Roundness from slow scanning speed

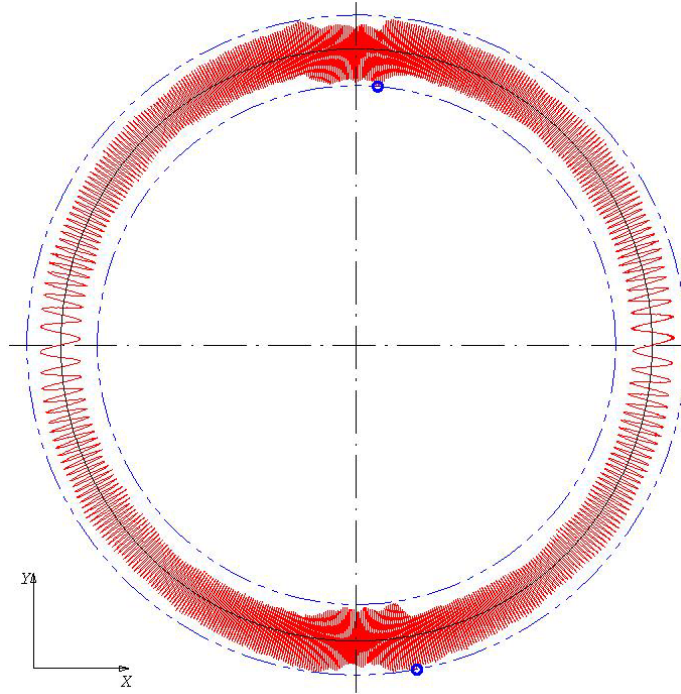


Figure 4.7: Roundness from medium scanning speed

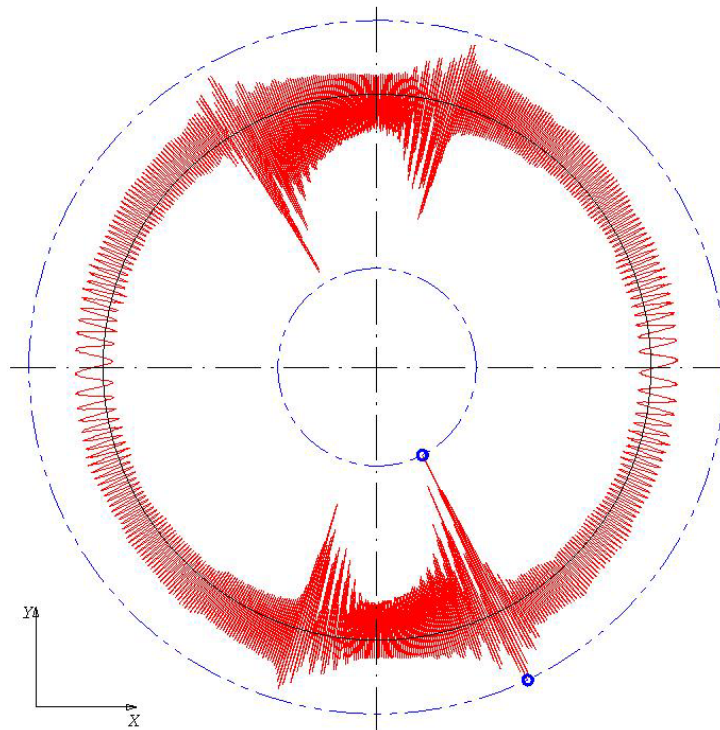


Figure 4.8: Roundness from fast scanning speed

The 7 mm/s data set contains frequencies that vary from 1.12 Hz to 13.18 Hz as shown in Table 4.1. This range encompasses the natural frequency of the LVDT which explains in part why disturbances appear at this and higher speeds. In the next chapter on modeling, these data are further analyzed in order to provide a means of selecting a proper scanning speed. The data are studied to determine if the disturbances in the data begin at this natural frequency.

It is desired to analyze the scan force and the deviations versus angular position for each speed in order to determine the correlation between the values. Since the control system attempts to maintain a constant force or deflection, noisy position data should correlate to rapidly fluctuating scanning force values. The force data must be calculated from the probe head deflection data which are stored. This calculation is made as shown in Equation 4.6 in the Cartesian coordinate system which is an extension of Equation 4.1. According to Leitz, the probe head has a spring constant of 1.8 N/mm. However, it is typical to express the scanning force in grams not Newtons. For this case, the spring constant can be found by dividing by the gravitational acceleration of 9.8 m/s² according to Newton's second law of motion, and the result is a spring constant of 185 g/mm. The scanning force is calculated from

$$F_m = k_{scm} \sqrt{x_{ph}^2 + y_{ph}^2 + z_{ph}^2} \quad (4.6)$$

where

F_m = scanning force (g),

k_{scm} = spring constant (185 g/mm),

x_{ph} = deflection of probe head in x-direction (mm),

y_{ph} = deflection of probe head in y-direction (mm), and

z_{ph} = deflection of probe head in z-direction (mm).

The data is then sorted in order of angular position because sometimes the first data point was actually made at 359.99 degrees instead of 0.01 and then plotted. The calibrated waveform for the inside surface of the ring is shown in Figure 4.9 and can be compared to the inside scan experimental results shown in Figures 4.10, 4.11, and 4.12. Figure 4.9 shows deviations off the final least-squares best fit radius of 76.116036 mm. Figure 4.10 shows the experimental results for scanning the ring at 0.5 mm/s with a 200 Hz cut-off frequency. Figure 4.11 shows the experimental results for scanning the ring at 7 mm/s

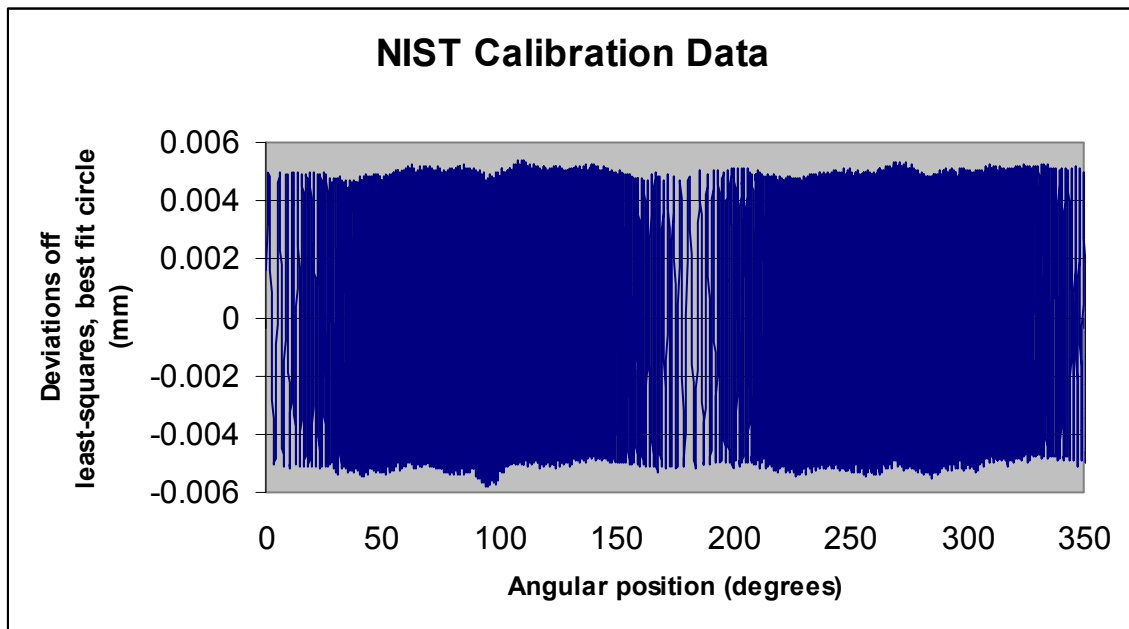


Figure 4.9 Inside calibrated waveform shown as deviations off of best fit radius

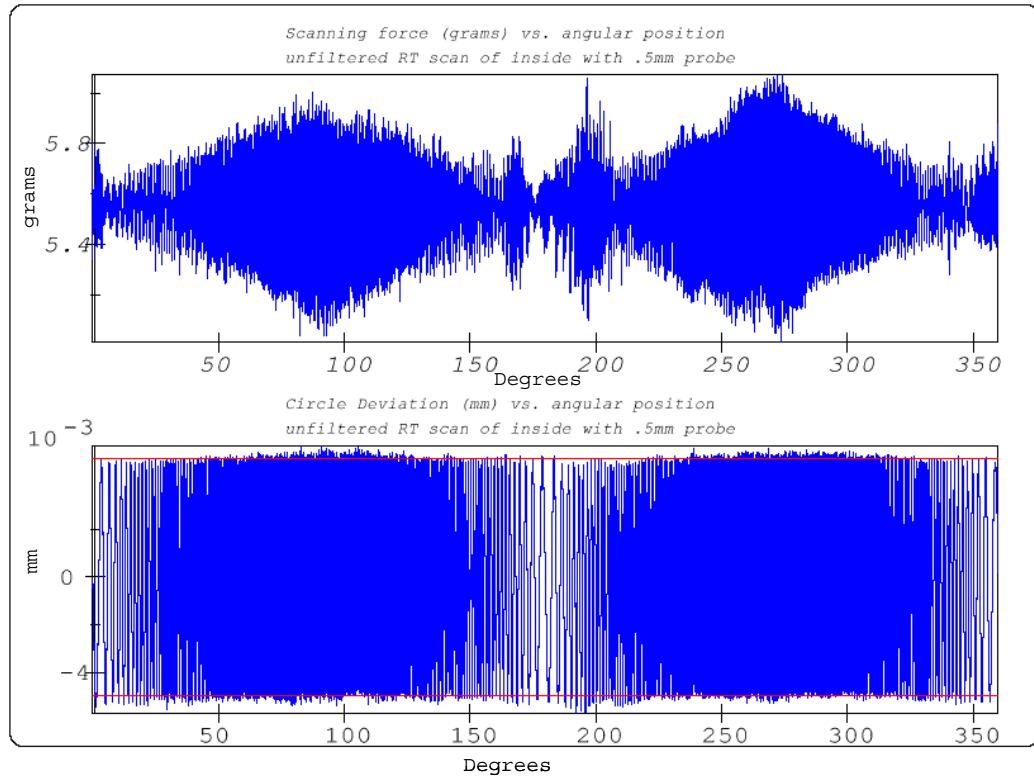


Figure 4.10: Force and deviations vs. angular position for slow scanning speed

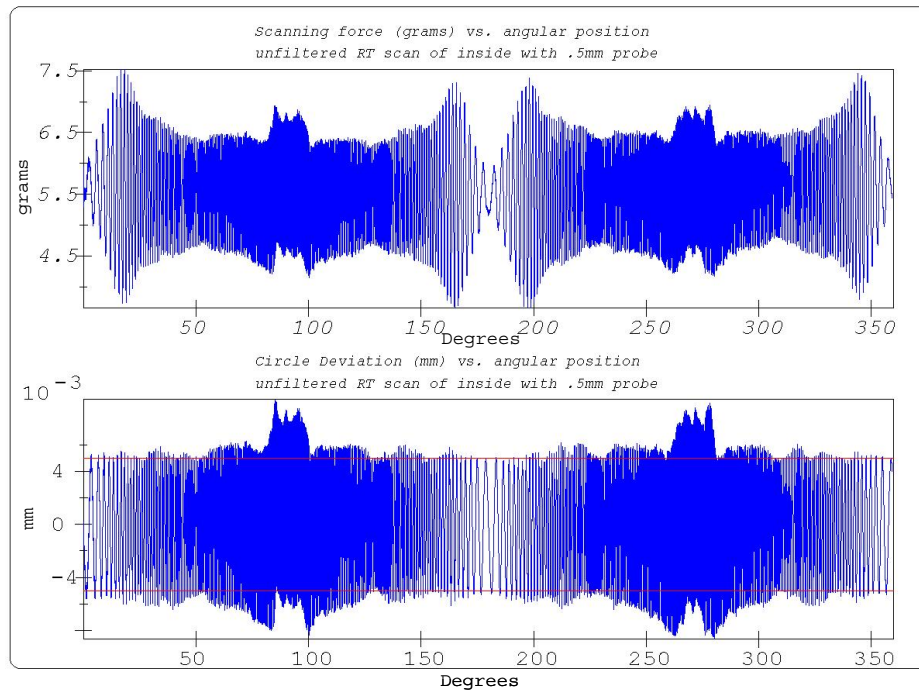


Figure 4.11: Force and deviations vs. angular position for medium scanning speed

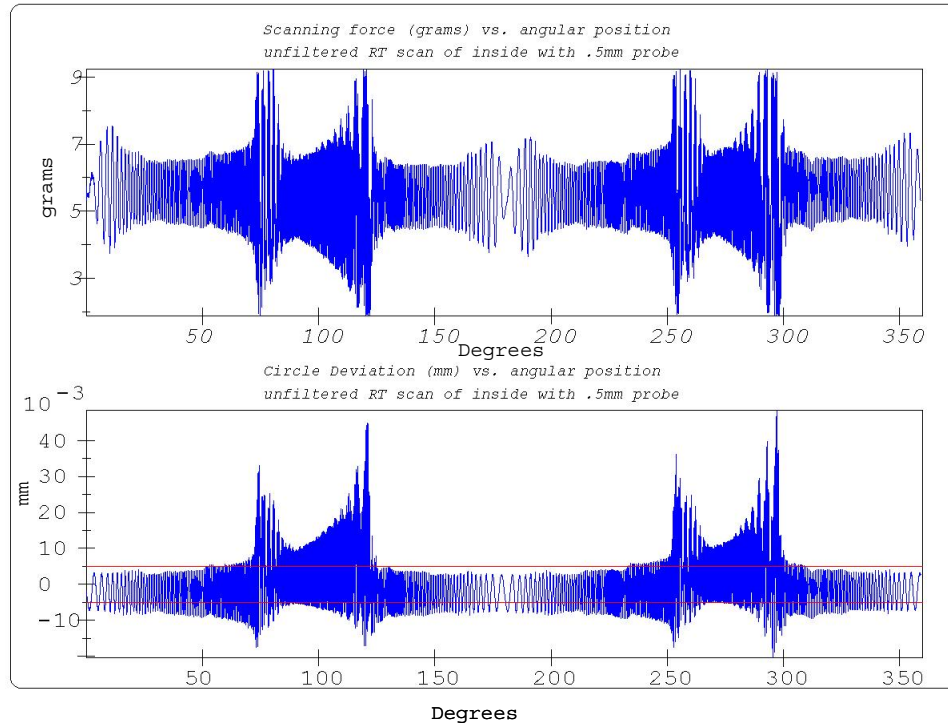


Figure 4.12: Force and deviations vs. angular position for fast scanning speed

with a 200 Hz cut-off frequency. Figure 4.12 shows the experimental results for scanning the ring at 11 mm/s with a 200 Hz cut-off frequency. It should be noted that these figures do not all have the same vertical range. The range of forces increases from 1.1 g for 0.5 mm/s, to 3.75 g for 7 mm/s, to 7 g for 11 mm/s. From these plots, it can also be seen that, in general, as the range in force increases, the range of deviations increases at the same angular position. It should also be noted that the force is most constant in the areas of longest wavelength where the following is easiest for the control system. Figures 4.11 and 4.12 also contain information that shows when the speed increases but the wavelengths are long enough, the scan can still maintain good following of the

waveform. For this reason, the beginnings and ends of these data sets have a higher variation in force without a corresponding increase in range of deviations.

4.5.2. Filtering effects

The filter used does not affect the scanning force. However, the filtering effect is evident in the roundness plots. When several roundness plots of scans at the same speed but with differing cut-off frequencies are studied, the substantial effects of filtering can be noted. Figures 4.13, 4.14, and 4.15 show the effects for a speed of 5 mm/s with cut-off frequencies of 2 Hz, 5 Hz, and 10 Hz, respectively. The resulting forms of the circle for

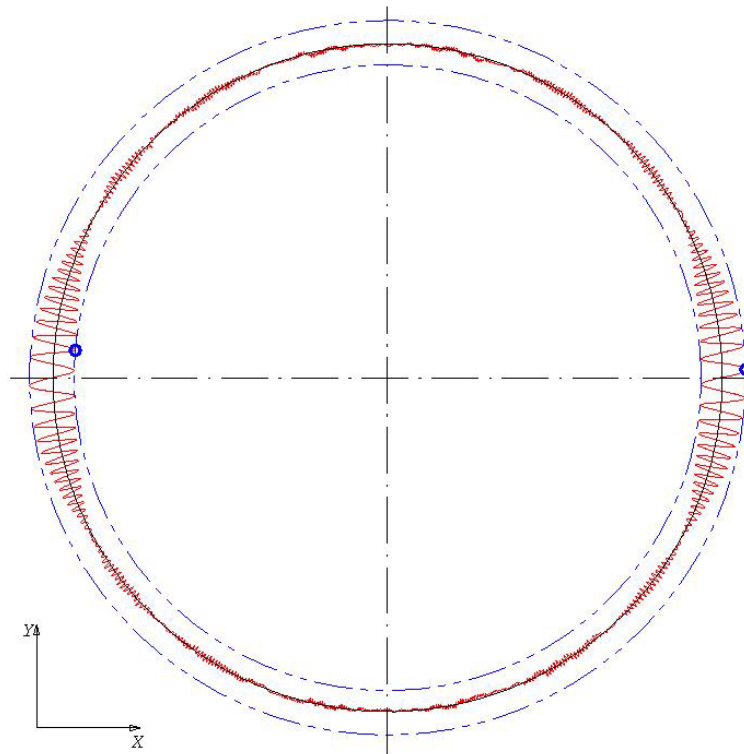


Figure 4.13: Roundness with low frequency cut-off

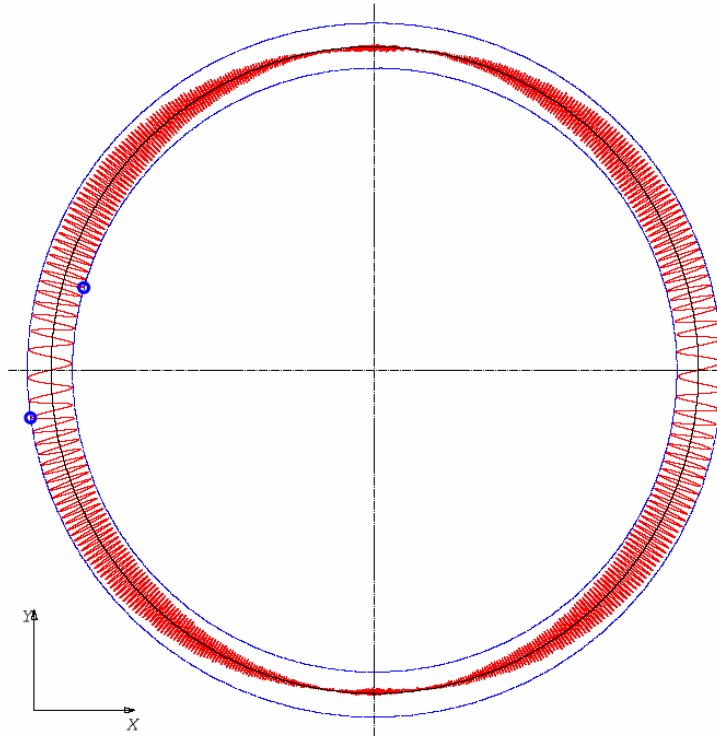


Figure 4.14: Roundness from mid-range cut-off frequency

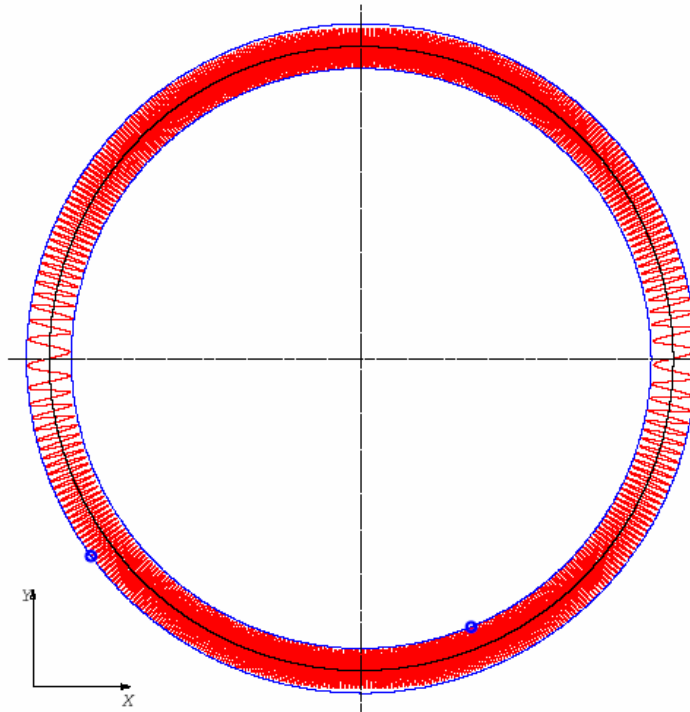


Figure 4.15: Roundness from high cut-off frequency

the cases of 2 Hz, 5 Hz, and 10 Hz are 10.1 μm , 10.6 μm , and 10.9 μm respectively. It should be noted from Table 4.1 that the input frequencies for 5 mm/s are 0.8 Hz to 9.42 Hz. Therefore, the 2 Hz cut-off frequency filters most of the data while 10 Hz should filter almost none of the data. From Figures 4.13 and 4.14, it can be seen that the high frequency portions of the data are being filtered.

5. Modeling

This chapter develops empirical models of CMM scanning that aid in the selection of scanning parameters. Methods are given to select parameters that provide the lowest achievable measurement uncertainty. These models must accurately represent the performance of scanning as a function of the user-selectable scanning speed and filter parameters. The generated models should be applicable to any scanning CMM and should be generated through a set of measurements that could feasibly be conducted in an industrial setting. Each model will function as shown in Figure 5.1. The inputs to the model are the measurements of the ring, the probe head natural frequency, the wavelengths of interest, and the allowable uncertainty. The outputs are the optimum scanning parameters to meet the input requirements. The models contain the data analysis routines that analyze the system scanning performance.

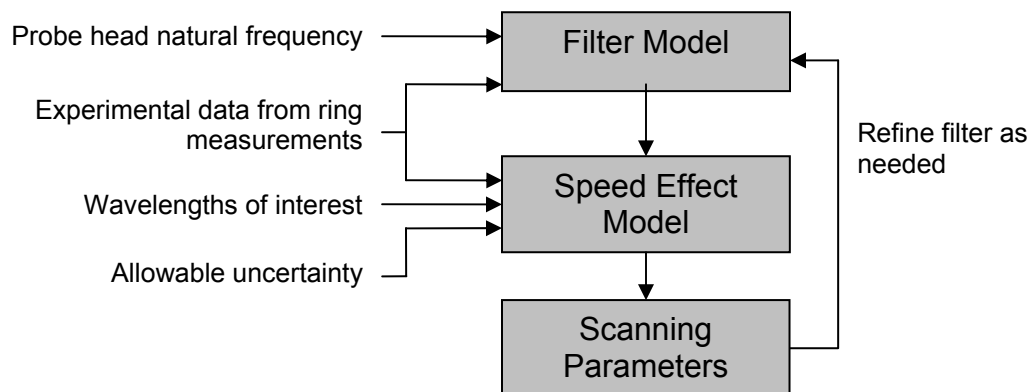


Figure 5.1: Schematic of modeling concept

5.1. Modeling of filtering effects

The purpose of this model is to characterize the filtering of scanning data. These digital filters are often proprietary and, as described in Chapter 4, must be characterized to ensure that no meaningful information is lost due to the effect of the filter which rejects certain frequencies. This model takes the experimental data from the ring experiments described in Chapter 4 and quantifies the filter parameters. A low-pass filter structure is assumed based on the application and the desire to filter high frequency noise.

5.1.1. Desired filter parameters to derive

For the theoretical filter model, a filter transfer function is calculated. For the digital filter, it is desired to specify the filter type, roll-off, stop band, transition band, pass band, and ripples [51]. The filter type determines which range of frequencies is in the pass band, and allowed to pass, in the stop band, and filtered out, or in the transition band where the data is partially passed through the filter. As the names signify, low-pass filters pass frequencies up to some cut-off frequency. In contrast, high-pass filters only allow data above some cut-off frequency to pass. The roll-off occurs in the transition band and quantifies how quickly the data is attenuated when moving from the pass band to the stop band. The roll-off is determined in part by the filter cut-off frequency. The ripples are caused by the imperfect attenuation of the signal in the stop band. These characteristics are shown in Figure 5.2. It can be seen that for the CMM under test, the filter type is a low-pass filter because it allows low frequency signals to pass while blocking higher frequencies.

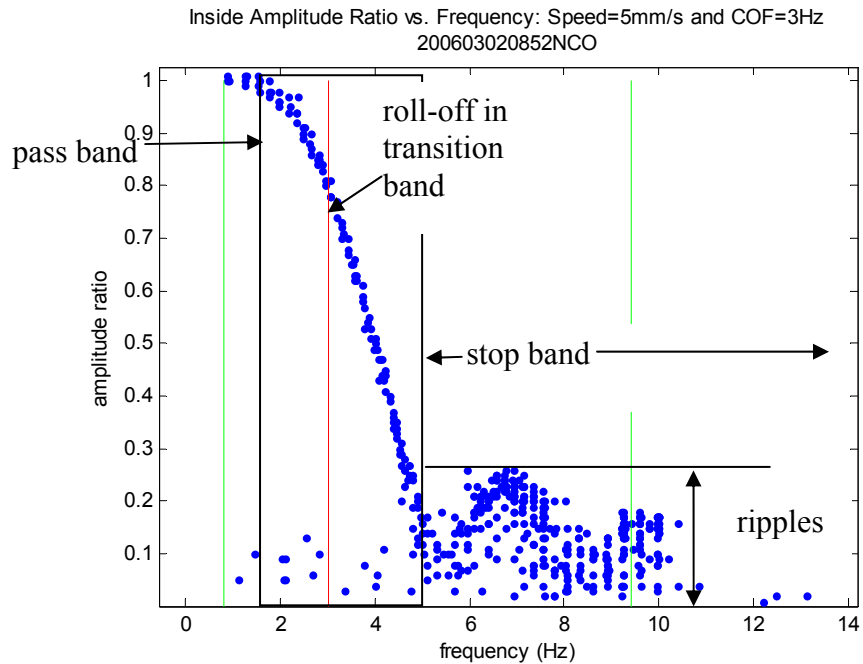


Figure 5.2: Filtering parameters

5.1.2. Mathematical methodology for filter modeling

Filter characterization can be performed in the frequency domain. As previously described, the input frequency seen by the system is found by dividing the scanning speed by the wavelength on the ring being scanned. Therefore, the input frequencies seen in this set of experiments varied from a low of 0.08 Hz to a high of 28.25 Hz. In order to transform the data into the frequency domain using MATLABTM [56], a Quindos program was written that puts the experimental data into a format that can be used by MATLABTM. Quindos [55] is the geometric data analysis program described in Section 4.2 that provides a user interface to Leitz CMMs. The Quindos program is given in Appendix 5. The output is a text file named according to the time of the experimental run and containing the angular position of each data point along with the deviations off the

best fit circle. This text file was then the input for the MATLABTM program given in Appendix 6.

This MATLABTM program is used to separate the waves in order to see the effect of scanning parameters on the measurement of various wavelengths. Every other zero crossing of the wave is assumed to signify the beginning of a new wave. This analysis is then verified by superimposing the lines calculated as separating the waves over the experimental data as shown in Figure 5.3. The waves shown in this figure are the deviations off the least-squares, best-fit circle for the data.

Figure 5.3 also shows how within each wave, the maximum and minimum deviations are found. The difference between these two values gives the peak-to-valley amplitude of

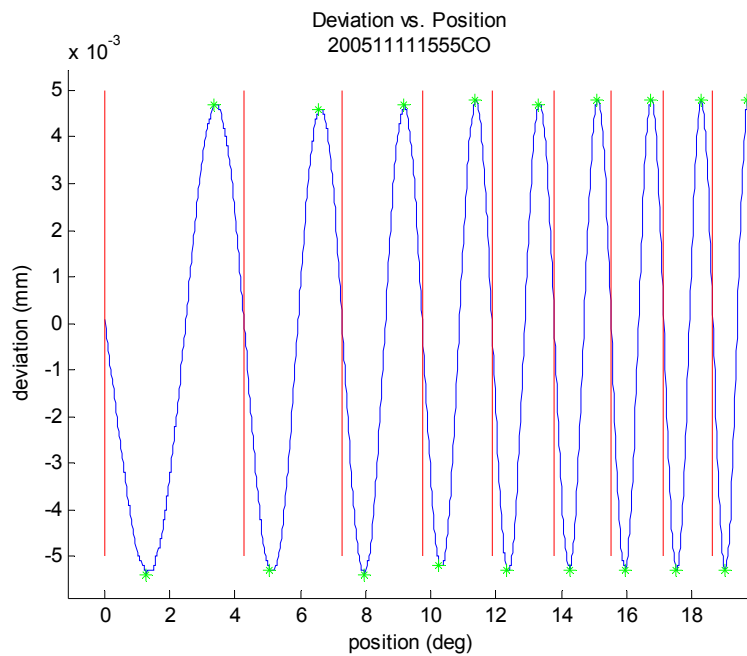


Figure 5.3: Analytical separation of waves and marking of maxima and minima

that wave. According to the calibration, each wave actually has an approximate 10 μm peak-to-valley amplitude. An amplitude ratio is then calculated as the amplitude divided by 10. Therefore, the amplitude ratio will vary from 0 for a wave with an amplitude of 0 to 1 when the wave has an amplitude of 10 μm . The wavelength is next calculated as a proportion of the circumference. Finally, the frequency is calculated as the speed divided by the wavelength. Once the frequency has been calculated for each wave, the frequencies and their corresponding amplitude ratios are sorted by frequency and plotted. Next, the filter cut-off frequency that was input during the selection of the experimental data set is plotted along with the theoretical input frequencies present in the data set based on the scanning speed. Sample results are shown in Figures 5.4 and 5.5.

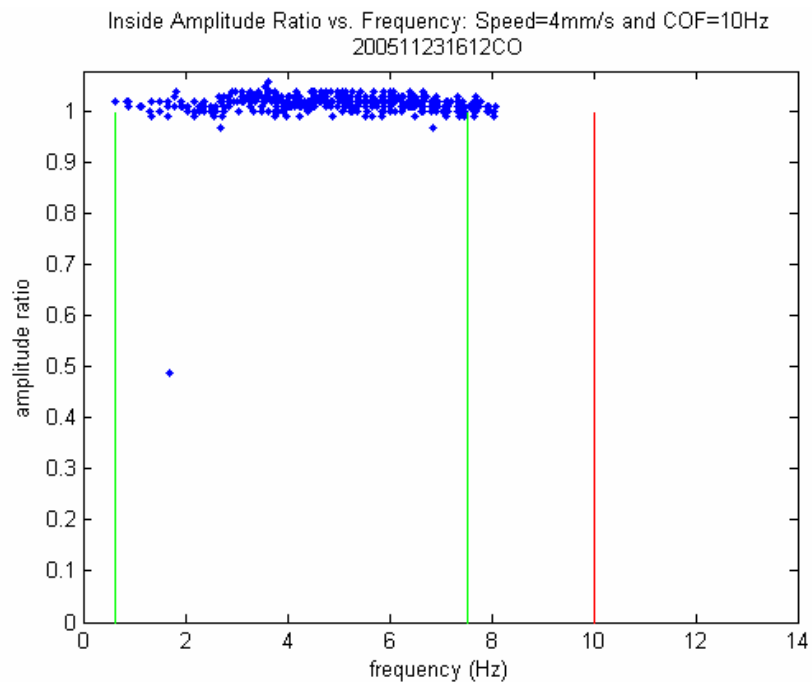


Figure 5.4: Experimental filtering results – no filtering apparent

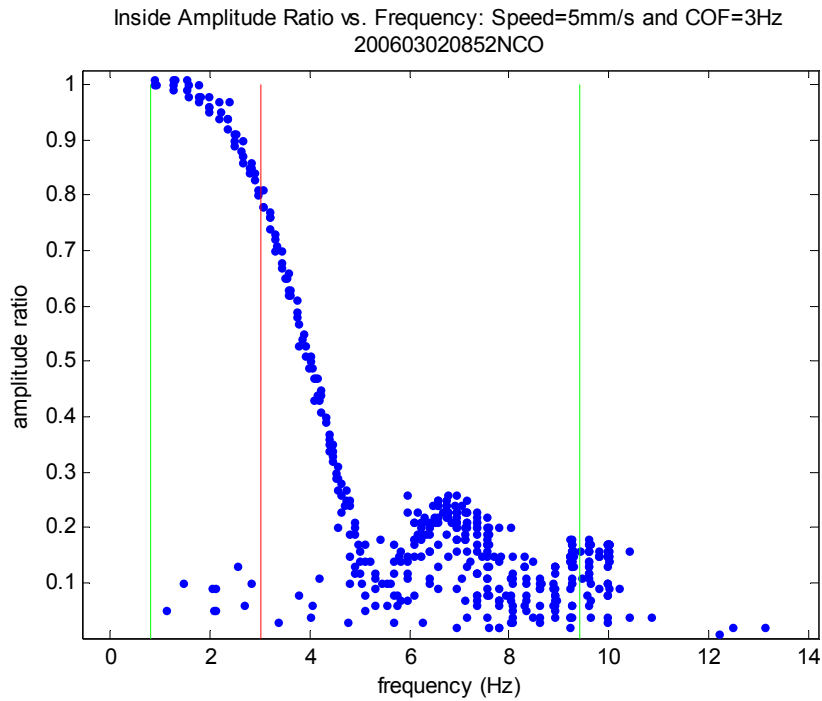


Figure 5.5: Experimental filtering results – filtering apparent

Using this technique the effects of each filter cut-off frequency are experimentally determined. As shown in Figure 5.4, if the cut-off frequency is beyond the frequency content of the data, no filtering occurs, and the amplitude ratio remains constant at approximately one. However, if the filter cut-off frequency is set within the data, then filtering occurs as shown in Figure 5.5. Important characteristics such as the filtering to 80% of the original amplitude at the cut-off frequency are readily apparent, but a more detailed characterization of the filtering parameters is needed.

5.1.3. Theoretical filter modeling results

A theoretical filter characterization is first conducted. A filter transfer function in the Laplace domain can be calculated according to

$$\frac{Y(s)}{X(s)} = G(s), \quad (5.1)$$

where

$Y(s)$ = output,

$X(s)$ = input, and

$G(s)$ = filter transfer function.

This characterization was performed using the MATLAB™ System Identification Toolbox [56]. The data was input into the toolbox using the program given in Appendix 7. The data input is shown in Figure 5.6.

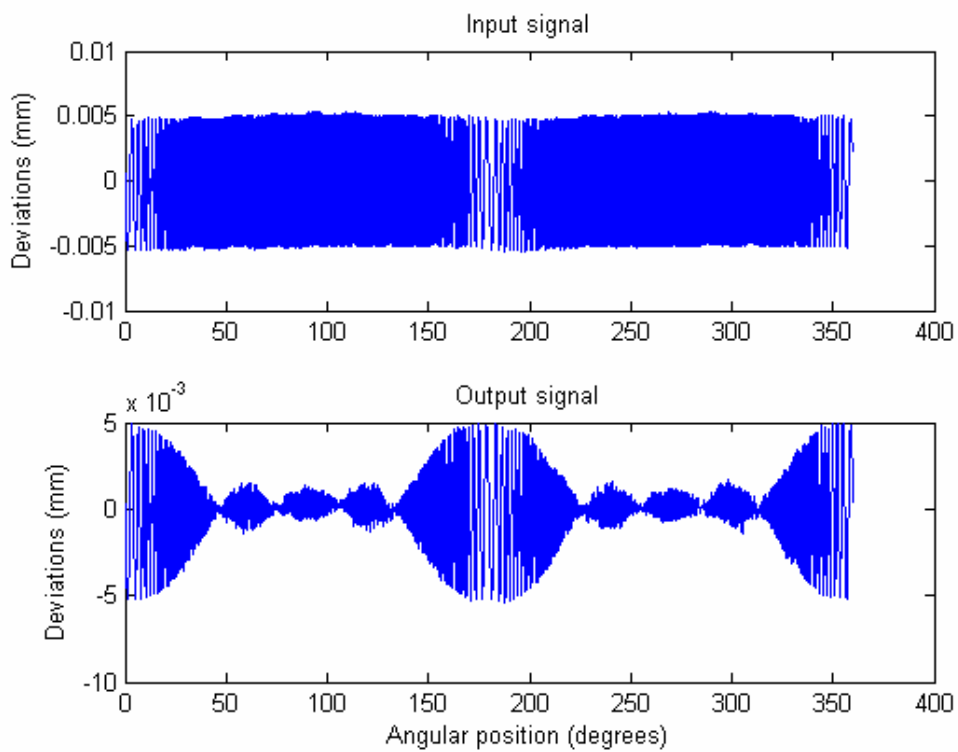


Figure 5.6: Input and output data for theoretical filter characterization

In the System Identification Toolbox, a process model is selected with certain characteristics such as numbers of poles and zeros. The Toolbox then fits a model to the data provided and generates the coefficients for the model. Some aspects of the filter structure can be observed from the filtered data characteristics. For example, the ripples seen in Figure 5.5 in the stop band indicate the presence of small resonances within the filter. Therefore, the filter must be second-order at a minimum. Additionally, some delay inherently exists in the system due to several factors including the time required to digitize and process the sampled data.

Through manual iterations on the filter characteristics, the addition of poles and a zero were found to bring the model closer to the actual data. The best model found was one with three underdamped poles, a zero, and a time delay. This filter is given by Equation 5.2

$$G(s) = K * \frac{1+Tz*s}{(1+2*Zeta*Tw*s+(Tw*s)^2)(1*Tp3*s)} * \exp(-Td*s) \quad (5.2)$$

where

$$K = -1.8381,$$

$$Tw = 5.2019,$$

$$Zeta = 0.42271,$$

$$Tp3 = 105.96,$$

$$Td = 22.625, \text{ and}$$

$$Tz = -1.5746.$$

Figure 5.7 shows the model output in gray superimposed over the measured output in black. The model captures the major characteristics of the filter but does not represent it perfectly. It is important to note that this model contains the maximum number of poles that can be simulated using this toolbox. A more accurate representation of the system, including the rates of change of the output, likely could be achieved if more poles could be included in the simulation.

5.1.4. Digital filter modeling results

Once the filter has been theoretically characterized, it is desired to find a reasonable digital model for the filter. A digital filter model is needed since the filter is implemented

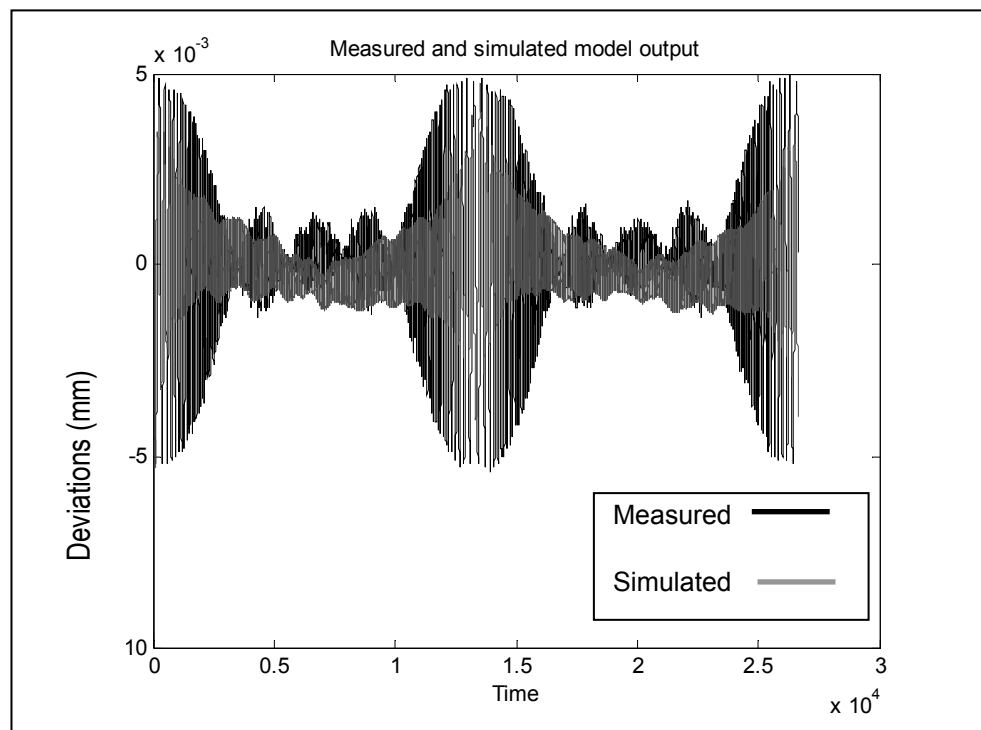


Figure 5.7: Measured and simulated filter output

digitally in the CMM system. The MATLAB™ Signal Processing Toolbox which contains a Filter Design and Analysis tool was used to perform this characterization. The theoretical filter that was generated in Section 5.1.3 was used to initialize the model. The MATLAB™ digital filter specifications [56] to be selected are shown in Figure 5.8.

The toolbox initializes the model as a low-pass, equiripple finite impulse response (FIR) filter. Next, the filter parameters must be selected in order to match the filter to the data shown in Figure 5.5. The sampling frequency, f_s , is calculated according to

$$f_s = \frac{N \cdot v}{2 \cdot \pi \cdot R_{f_i}} \quad (5.3)$$

as the number of points, N , measured during the experimental run divided by the measurement time. The measurement time is the circumferential length found from the

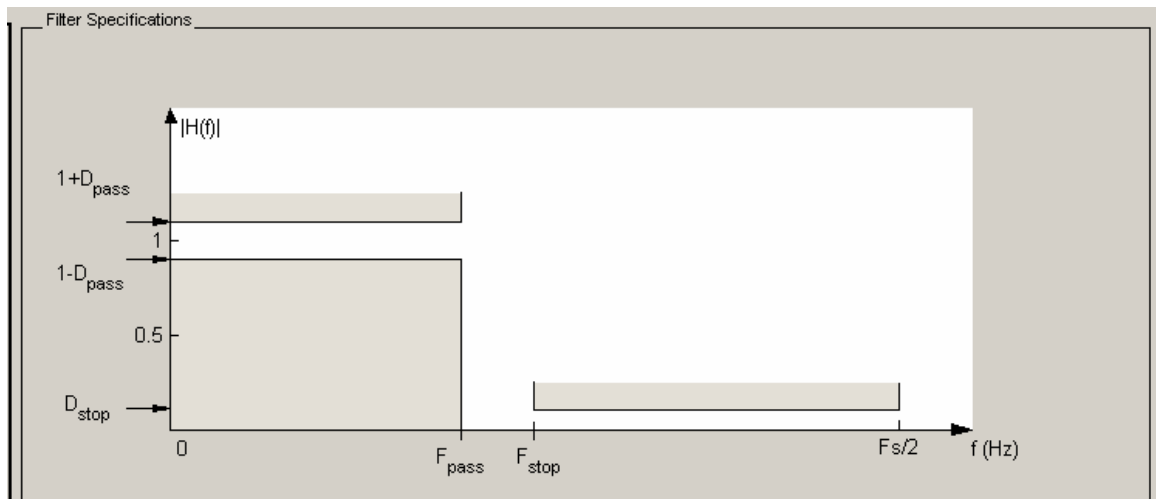


Figure 5.8: MATLAB™ digital filter specifications

inner radius, R_{fi} , divided by the scanning speed, v ,

where

$N = 23794$ points,

$v = 5$ mm/s, and

$R_{fi} = 76.15$ mm.

For scanning the inside of the ring at 5 mm/s, f_s is 248.65 Hz.

From a comparison of Figure 5.5 to Figure 5.8, several parameters including the passband frequency F_{pass} , the passband ripple D_{pass} , the stopband frequency F_{stop} , and the stopband attenuation D_{stop} were set to the following values:

$F_{pass} = 1.8$ Hz

$D_{pass} = 0.02$ units

$F_{stop} = 5$ Hz

$D_{stop} = 0.25$ units.

MATLABTM then designs a digital filter that matches these characteristics. The MATLABTM digital filter design is shown in Figure 5.9, and the pole/zero plot for this filter structure is given in Figure 5.10. The resulting MATLABTM file is given in Appendix 8.

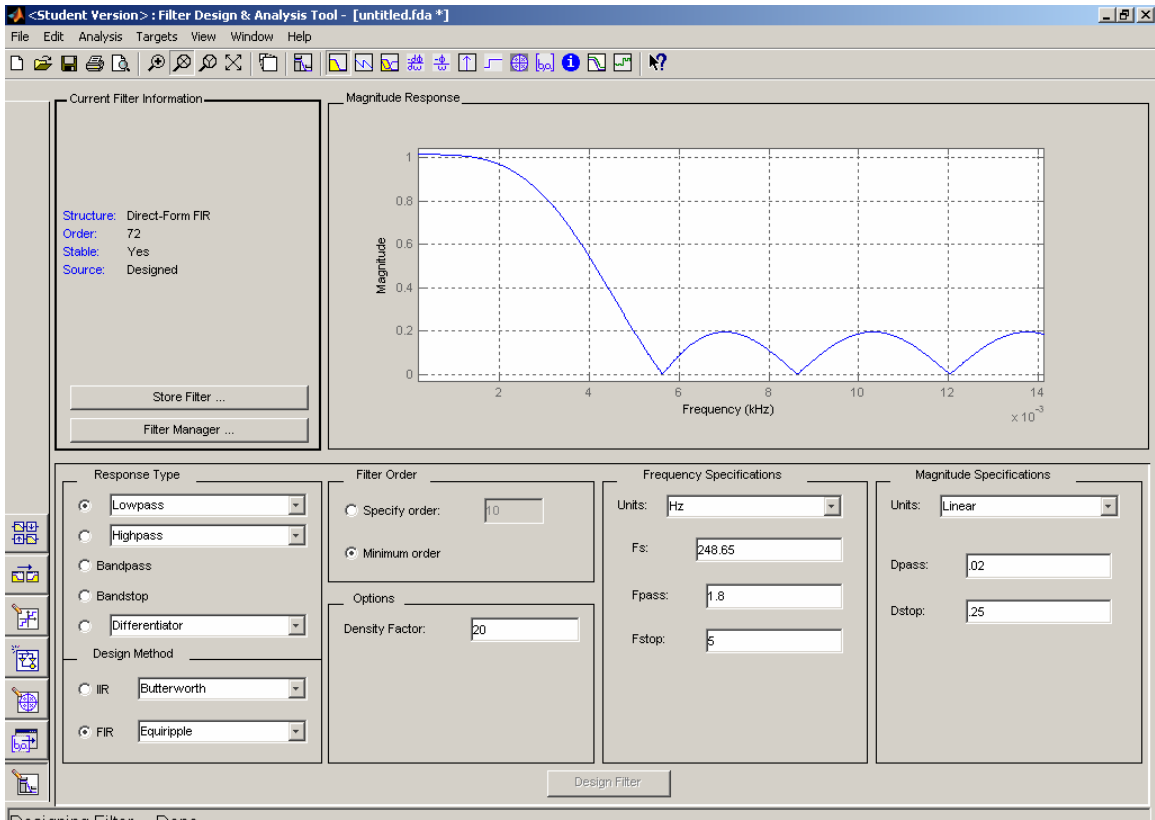


Figure 5.9: Digital filter design in MATLABTM

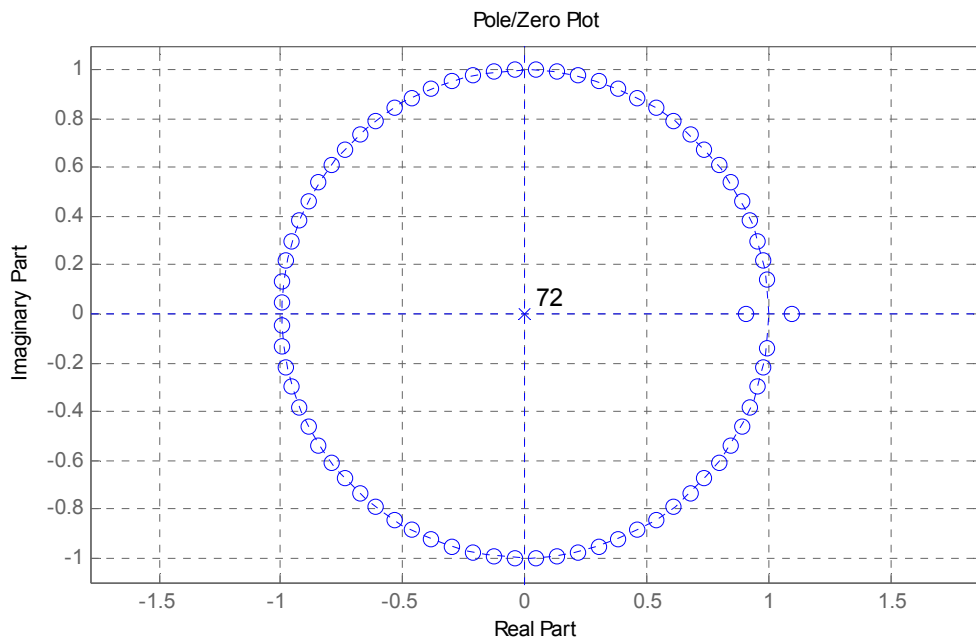


Figure 5.10: Pole/zero plot for digital filter

The minimum order is determined by the Parks McClellan optimal FIR filter order estimation method [57] which uses the parameters specified above to estimate the required order. The designed digital FIR filter uses a 72nd order system in a structure defined by

$$Y_f(t_f) = \sum_{n_f=0}^{72} h_f(n_f) \cdot x_f(t_f - n_f) \quad (5.4)$$

where

Y_f = filter output,

h_f = filter coefficients,

n_f = order of filter,

x_f = sample, and

t_f = time increment.

For digitally sampled systems, each sample is delayed by $1/f_s$ from the previous sample. FIR filters use a sum of the current sample and n samples adjacent to the current sample, multiplied by n_f+1 corresponding filter coefficients to produce a single filtered output sample. For a digital filter of order n_f , there are always n_f+1 coefficients [58]. The designed filter coefficients are given in Table 5.1.

These coefficients are the Fourier series coefficients of the filter frequency response and therefore in the time domain represent the time constants of the system [59]. The goal of

Table 5.1: Digital filter coefficients

#	Value	#	Value	#	Value
1	-0.096589996	25	0.023927646	49	0.023927646
2	0.002697494	26	0.024989033	50	0.022831088
3	0.002839692	27	0.025972176	51	0.021681455
4	0.003089186	28	0.026895708	52	0.020482488
5	0.003454683	29	0.027728276	53	0.01926881
6	0.003919166	30	0.028502512	54	0.018030774
7	0.004487232	31	0.029153892	55	0.016787373
8	0.005149786	32	0.029824637	56	0.015549787
9	0.005909834	33	0.030308196	57	0.01432036
10	0.00671457	34	0.030584315	58	0.013103488
11	0.007654109	35	0.030918938	59	0.011927152
12	0.008638277	36	0.031041263	60	0.01078181
13	0.009684922	37	0.031131703	61	0.009684922
14	0.01078181	38	0.031041263	62	0.008638277
15	0.011927152	39	0.030918938	63	0.007654109
16	0.013103488	40	0.030584315	64	0.00671457
17	0.01432036	41	0.030308196	65	0.005909834
18	0.015549787	42	0.029824637	66	0.005149786
19	0.016787373	43	0.029153892	67	0.004487232
20	0.018030774	44	0.028502512	68	0.003919166
21	0.01926881	45	0.027728276	69	0.003454683
22	0.020482488	46	0.026895708	70	0.003089186
23	0.021681455	47	0.025972176	71	0.002839692
24	0.022831088	48	0.024989033	72	0.002697494
				73	-0.096589996

the Parks McClellan minimization function [56] is to minimize the maximum error between the desired and actual filter frequency responses by selecting the optimum coefficients. Since the designed coefficients only vary from a minimum of -0.09659 to a maximum of 0.03104, this small variation within an order of magnitude confirms that all coefficients are significant.

The designed coefficients are valid for the sampling rate that is used for a scanning speed of 5 mm/s. For a different sampling rate, the coefficients are dynamically re-calculated within the CMM controller or retrieved from a look-up table stored within the CMM.

Once the digital filter model is determined, the modeled results are compared to the experimental results as shown in Figure 5.11. Figure 5.11 shows good agreement between the model and experimental results. For example, at the cut-off frequency of 3 Hz, both data sets show an amplitude ratio of 0.8. The -3 dB level where the amplitude ratio is at 0.5 can also be compared. This level occurs just past 4 Hz for both the modeled and experimental results. The design parameters can also be compared, and the F_{pass} of 1.8 Hz, D_{pass} of 0.02 units, F_{stop} of 5 Hz, and D_{stop} of 0.25 units are all observed in the filter model as in the experimental data. Additionally, the resonances occur at frequencies of approximately 7 and 10 Hz.

5.1.5. Use of models to select filter

The filter must be selected to filter noise and disturbances but not surface data. If not filtering data were the only concern, a high filter cut-off frequency could be set.

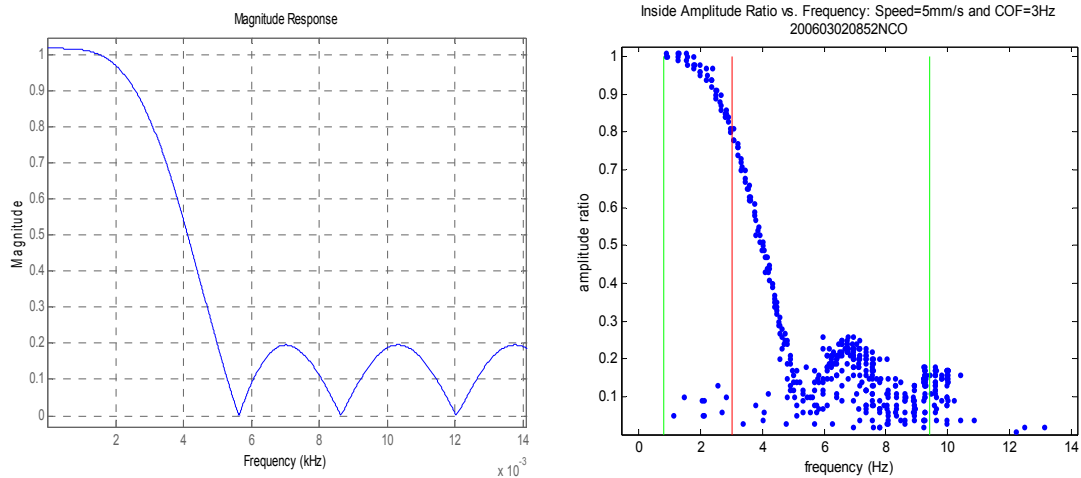


Figure 5.11: Comparison of digital filter model to experimental filtering results

However, as shown in Figure 5.12 for a 2 mm/s scan using a 200 Hz cut-off frequency, noise may be present in the data set which should only contain frequencies from 0.32 to 3.77 Hz. In Figure 5.12, noise is detected at frequencies in the 33 Hz and 50 Hz bands. Therefore, a filter should be selected that filters this noise from the data. For a speed of 2 mm/s, a 10 Hz filter filters the noise without filtering the ring surface data. A comparison of the effects of the 10 Hz and 200 Hz filters on this data is seen in Figure 5.13.

Using the methods developed in this section, theoretical and digital models of a proprietary CMM filter are developed from the wavy ring experimental data. These models simulate the effects of the filter on any given experimental data set and predict whether the surface data and expected noise patterns are filtered. With this knowledge, user selectable filter parameters, such as cut-off frequency, can be appropriately set to

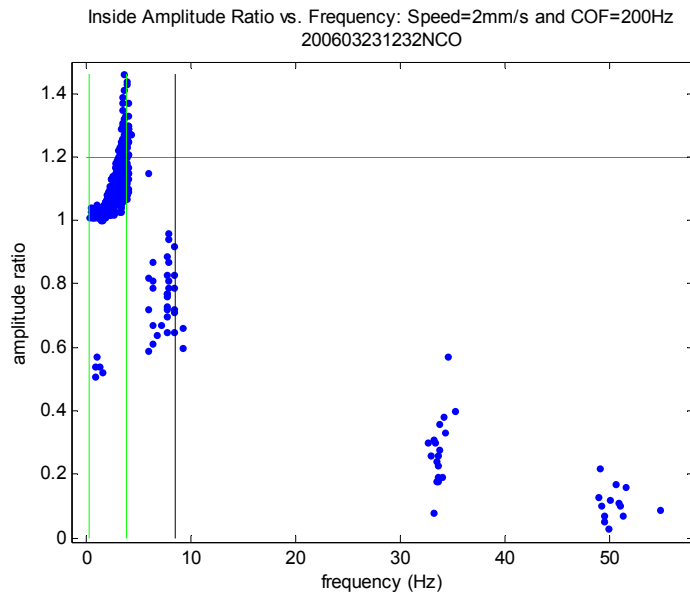


Figure 5.12: Experimental data showing noise beyond data range

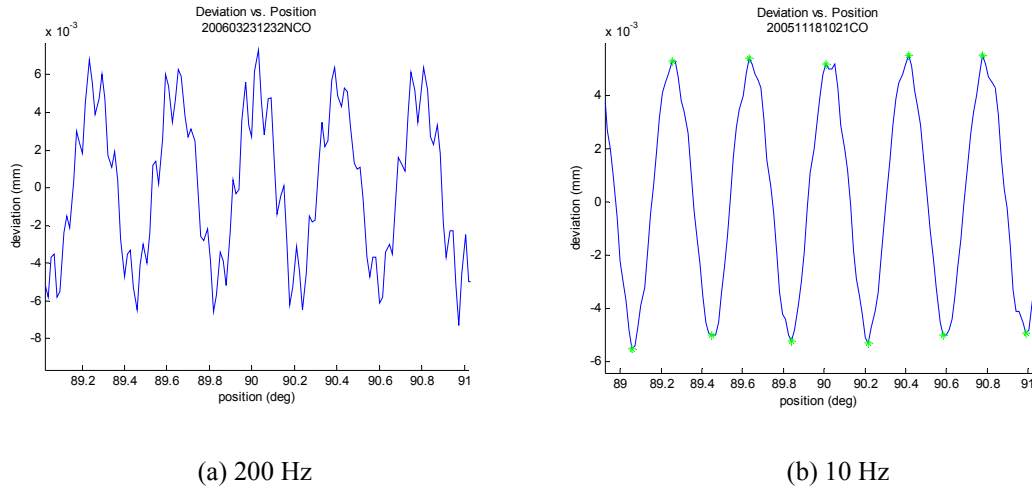


Figure 5.13: Comparison of filtering with different cut-off frequencies

filter out noise but not surface data. The selected parameters should then be used in the experiments for modeling the scanning speed effects.

5.2. Modeling of scanning speed effects

The purpose of these models is to characterize the effects of scanning speed on measurement capability. Like the filters described previously, the servo loop for CMMs is also proprietary, so empirical methods must be used to determine the effects of scan speed. This model takes the experimental data from the ring experiments described in Chapter 4 and quantifies the effect of scanning speed.

5.2.1. Modeling objectives

The objectives of the modeling are to determine the primary sources of disturbances in scanning data and to quantify the measurement uncertainty that exists for a given

scanning speed. This information can then be used to select a scanning speed. A primary source of disturbance in the system is the natural frequency of the probe head which limits the bandwidth of the servo loop. When the input frequency equals the natural frequency, resonance occurs in the system due to secondary mechanical motions. This motion generates a disturbance that is difficult to distinguish from noise in the measurement data. In this case, the bandwidth of the servo loop has been exceeded because the probe can no longer track the surface waves.

This servo loop is shown in Figure 5.14. Figure 5.14 shows how the initial input to the controller is e_s , the error signal. This signal is input into the controller which outputs a commanded position, u , to the CMM that will take the probe to the proper location based on the pre-defined circle path. The output, y_o , is therefore the actual measured position which is then converted back into units of force for comparison to the force set point per

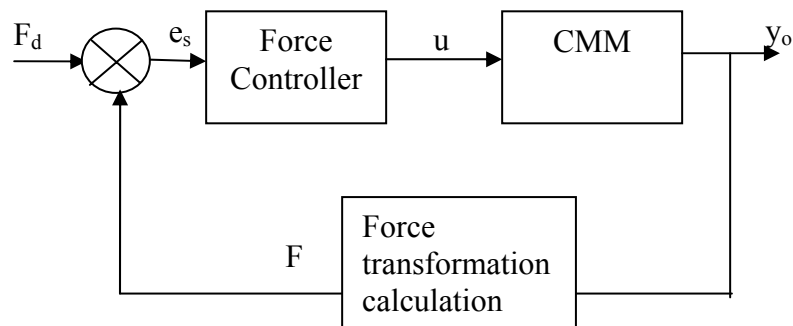


Figure 5.14: Servo loop

Equation 4.6. The difference between this force and the nominal force, F_d , is used by the controller to adjust the commanded data and improve the scanning performance. When the error signal is large, this suggests that the bandwidth has been exceeded. Data are not reported when contact is lost with the surface and the force is outside the acceptable range. Although the servo loop is proprietary and its specifications are unknown, the models developed will be used to characterize this servo loop and model scanning performance.

5.2.2. Modeling the combined effects of scanning speed and probe head natural frequency

The natural frequency of the probe head in the x-direction was determined in Section 4.1.5 to be 8.55 Hz. The data format presented in Figures 5.4 and 5.5 can be used here to determine the effect of natural frequency. The program used to create Figures 5.4 and 5.5 is given in Appendix 6. This program is modified to show a vertical line at the location of the natural frequency. Additionally, a horizontal line is plotted at an amplitude ratio of 1.2. From Section 5.1.2, the amplitude ratio is defined as the amplitude of a wave divided by the nominal amplitude of 10 μm . A ratio of 1.2 is selected as being significant since this represents a 20% disturbance in the signal. The resonance that occurs at the natural frequency is often a source of this disturbance.

In order to separate filtering and natural frequency effects, only experimental sets with unfiltered measurement data containing observable natural frequency effects are examined and given in Figure 5.15. It is known that the measurement data in these sets is

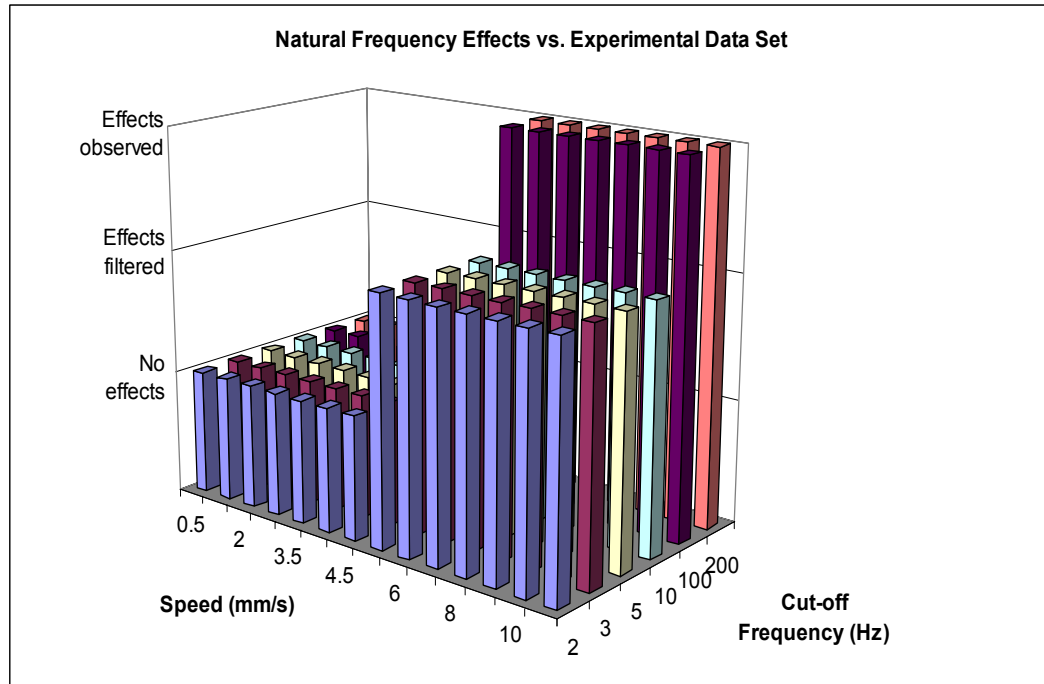


Figure 5.15: Natural frequency effects in experimental data sets

unfiltered because the cut-off frequency is set higher than the maximum frequency of the wave for the scanning speed. These maximum frequencies can be seen in Table 4.1.

Speeds less than 5 mm/s were eliminated because the natural frequency is not encountered at these speeds and therefore has no effect. At higher speeds, cut-off frequencies of 10 Hz or less filter the natural frequency effects and some of the measurement data.

For each speed, the experimental data set with a cut-off frequency of 100 Hz was plotted as shown in Figure 5.16. This cut-off frequency was selected because it is the minimum cut-off frequency for which no filtering is present for the speeds under consideration. As

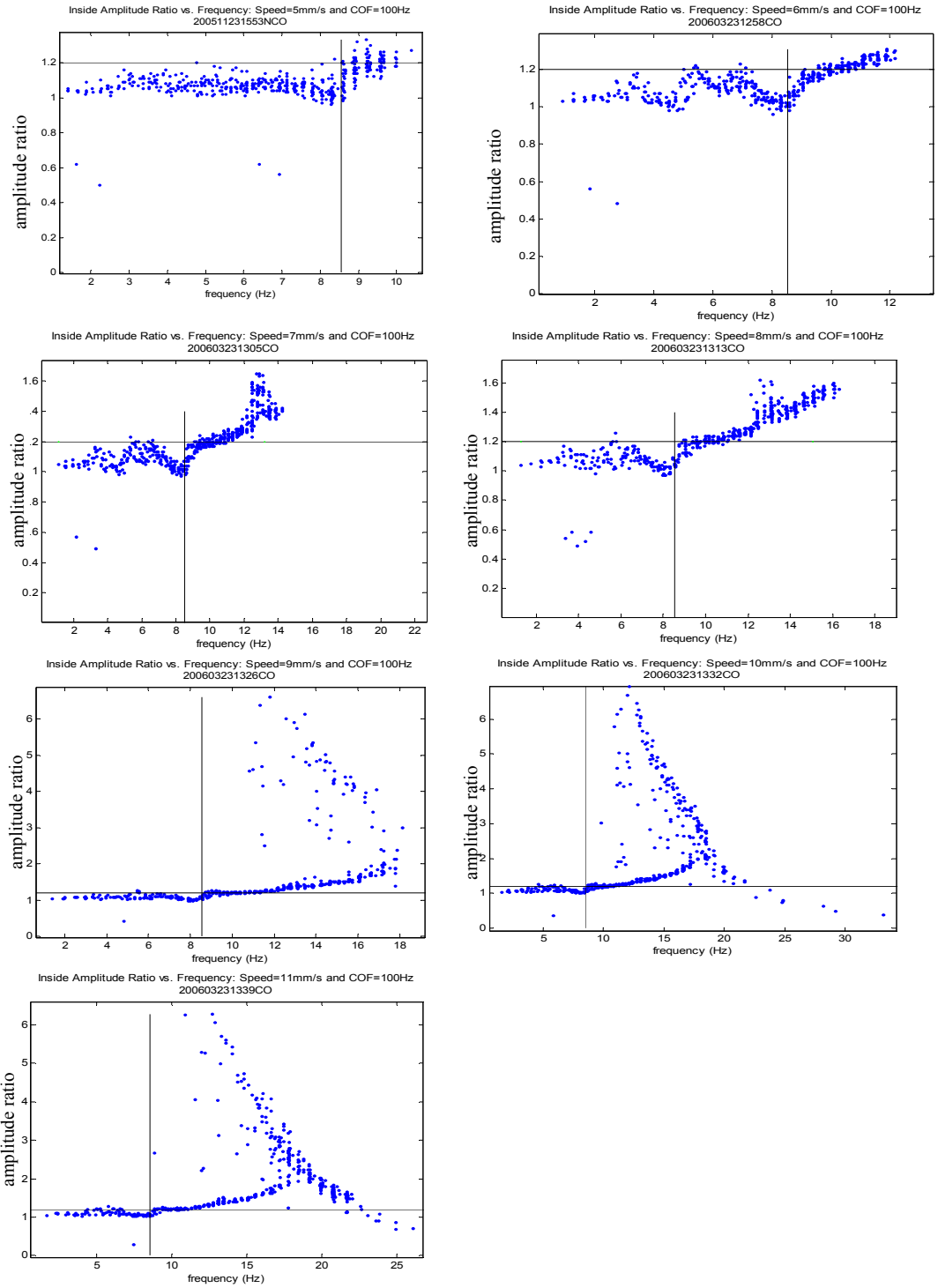


Figure 5.16: Combined effect of natural frequency and scanning speed on scanning performance

can be seen from Figure 5.16, the amplitude ratio begins increasing without bound when the natural frequency is reached at each speed. An increase in amplitude above one indicates that the system response has been dynamically disturbed. The disturbance in the data become significant at the natural frequency or soon thereafter. Therefore, the disturbances exhibited in these experimental data sets are attributable to the natural frequency that leads to system vibrations. This analysis shows that examination of data from the wavy ring artifact could also be used to experimentally determine the natural frequency of the probe head.

5.2.3. Modeling the effect of scanning speed on measurement uncertainty

The ISO standard 15530-3 [60] describes an experimental method for determining the uncertainty of a measurement using a calibrated artifact. This is a special case of the uncertainty determination method described in Section 2.2. The basis of this standard is that the uncertainty in such a measurement can be found from the difference in the measured and calibrated values of the artifact. Uncertainty sources that must be considered include standard uncertainty due to the measurement strategy, u_p , calibration standard uncertainty from the calibration certificate, u_{cal} , and any bias between the measured and calibrated values, b . Additional terms can be added if this method is to be extended to provide an uncertainty estimate for workpieces that are very similar to the calibrated workpiece. Equation 5.5 gives the mathematical form of this uncertainty evaluation as it is given in 15530-3; namely,

$$U = k \times \sqrt{u_{cal}^2 + u_p^2} + |b| \quad (5.5)$$

where

U = the expanded measurement uncertainty,

k = coverage factor determining level of confidence in uncertainty estimate,

$u_{cal} = \frac{U_{cal}}{k}$ where k is the coverage factor used in the artifact calibration,

$u_p = \sqrt{\frac{1}{N-1} \sum_{i=1}^N (y_i - \bar{y})^2}$ = the standard deviation of measured values, and

$b = \bar{y} - x_{cal}$ where \bar{y} is the average measured value and x_{cal} is the calibrated value.

The above equation is appropriate for measurands which yield a discrete result such as the diameter of a circle. However, this equation is not directly applicable to the measurement of the ring for which the measurand is the deviations off of the best fit circle because a \bar{y} cannot be calculated. Alternative calculations must be used to account for the standard deviation of the measured values. Based on this measurand, the bias should be removed from Equation 5.5 because the bias represents how well the radius was measured. The quality of radius measurement is not included in the measurand of deviations off of best fit circle.

The equivalent uncertainty for the wavy ring can be calculated using the following procedure. Each data point consists of the angle of measurement and the deviation from the best fit circle for that point. Each data set is independent and will generate a slightly

different radius. To account for this difference, the data must be referenced to a common radius.

The experimental data were collected in two sets in November 2005 and March 2006.

Temperature compensation was not used, so the temperature difference led to different best fit radii. The average best fit radius in 2005 was 76.3144 mm. The average best fit

radius in 2006 was 76.1124 mm. The calibrated radius was 76.116036 mm. The data

were divided by year. For each year, the data for all experimental sets were re-fit to the

best fit center and radius of the slowest scan speed. The re-fit deviations were then added

to the slow scan speed radius to obtain the surface data for the scanned data. For the

calibration data, the calibrated deviations were added to the slow scan speed radius.

These data transformations were performed in Quindos and are shown in Table 5.2.

Once these data transformations had been performed, the experimental data could be directly compared to the calibration data. Although the nominal angular values are the same for each measurement made with the same set of scanning parameters, the actual angular value for each measurement will vary. As an example, the fifth measurement

Table 5.2: Data transformations to unify reference data

	Calibration data	Experimental data
Scans in 2005	$r_{cal} = r_{slow2005} + dev_{ori_cal}$	$r_{exp} = r_{slow2005} + dev_{bestfit_slow2005}$
Scans in 2006	$r_{cal} = r_{slow2006} + dev_{ori_cal}$	$r_{exp} = r_{slow2006} + dev_{bestfit_slow2006}$

point nominally may be at an angular location of 2 degrees while the measured values may be at angles of 1.99 degrees or 2.02 degrees. Especially at the higher frequencies, these slight angular differences could lead to false comparisons of calibrated and measured data. Additionally, there are 26880 calibrated data points compared to approximately 23800 measured data points. Due to these challenges, the measured points cannot be directly correlated with calibrated data points. Instead, a fifth-order polynomial is fit through the six nearest calibration points, and the normal distance from the measured point to the calibrated spline is calculated as shown in Figure 5.17. A fifth-order polynomial was sufficient to generate an accurate representation of the calibrated waveform near the measured point without producing a computational burden. Using additional points to generate a higher-order polynomial would not substantially alter the curve in the region of interest.

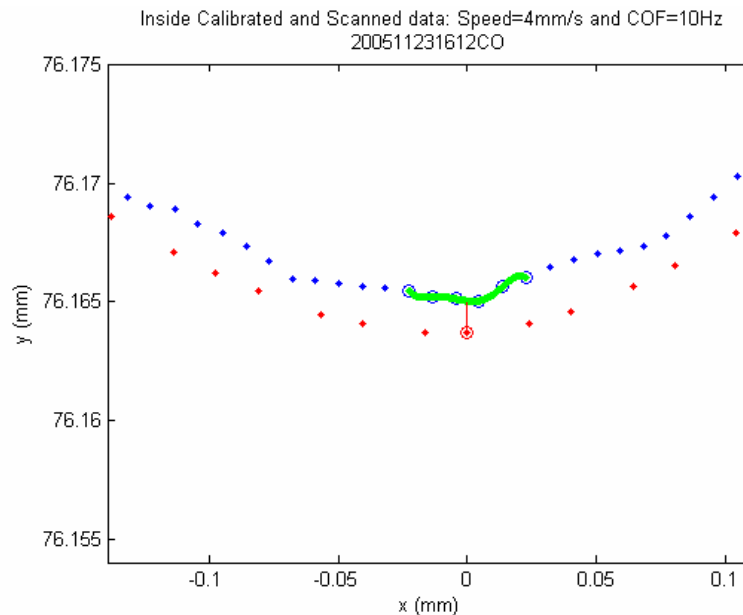
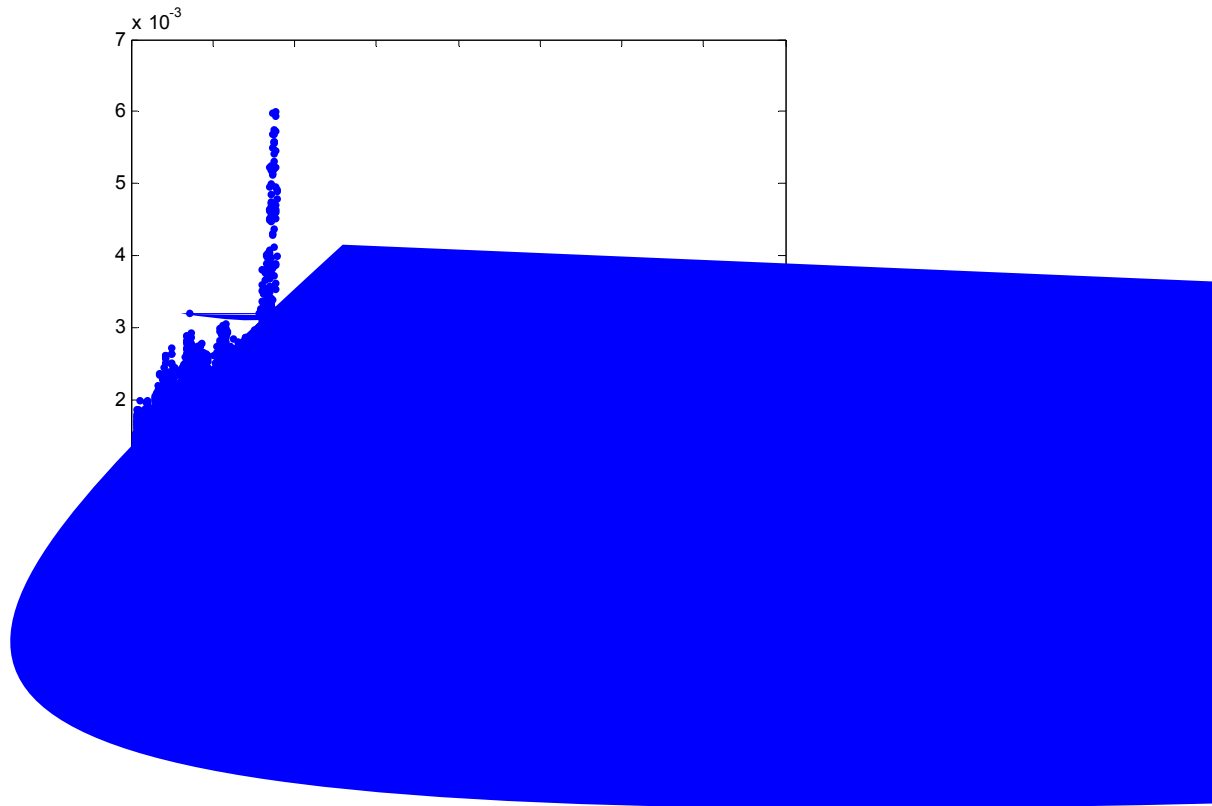


Figure 5.17: Graphical representation of the error between measured and calibrated values

This normal distance is the error between the measured and calibrated values and is stored. The MATLABTM program used to perform these calculations is given in Appendix 9. These calculations were performed for each speed tested using the lowest filter cut-off frequency at each speed that would not filter out actual data as determined in Section 5.1. The cut-off frequencies used were 5 Hz for speeds of 0.5 and 1 mm/s, 10 Hz for speeds from 2 to 4.5 mm/s, and 100 Hz for speeds of 5 mm/s and greater. For 0.5 mm/s, 5 Hz was used instead of 3 Hz because this data set was better centered which required less data processing. Additionally, data analysis confirmed that the 5 Hz data is not noisier than the 3 Hz data.

The errors can then be plotted versus angular position as shown in Figure 5.18. This figure shows that the highest errors occur at the shortest wavelengths around 90 and 270



degrees. The longer wavelength regions near 0, 180, and 360 degrees show smaller errors. A histogram of these errors can then be created as shown in Figure 5.19, and the standard deviation of the error data calculated from this data. This histogram shows a Gaussian distribution of data, from which a standard deviation can be easily calculated.

It should also be noted that the bias which is being ignored in this analysis is represented by the distance of the highest peak from zero. The bias is ignored because the measurand for the experimental scans is a roundness instead of a profile measurement. The ring could be used to analyze profile measurements, in which case the bias would be included. The deviations measurand makes this analysis applicable to roundness machines as well as CMMs.

Histogram of error between Inside calibrated and scanned data: Speed=7mm/s and COF=100H
200603231305CO

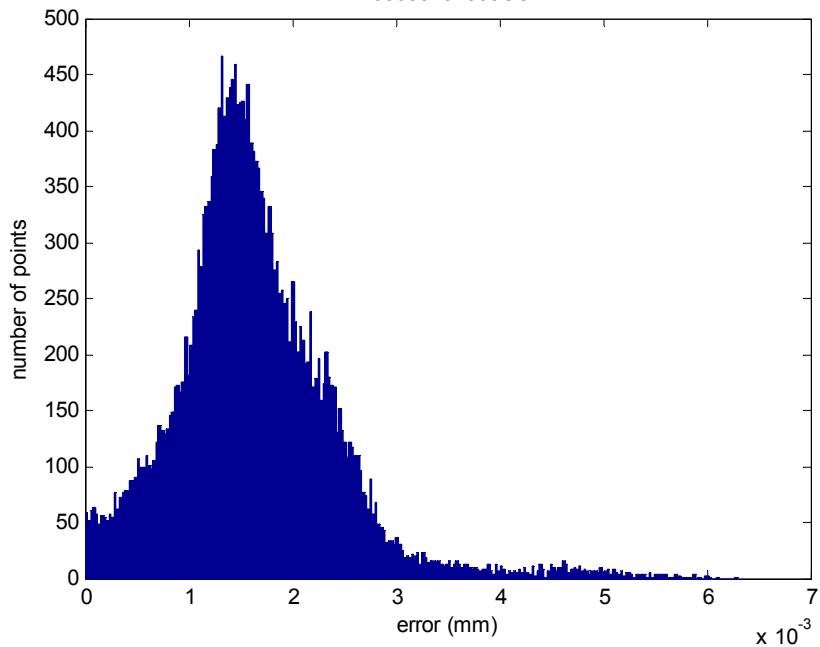


Figure 5.19: Histogram of errors showing standard deviation and bias

Since the bias is no longer included in the uncertainty calculation, U can be calculated by

$$U = k \times \sqrt{u_{cal}^2 + u_p^2}. \quad (5.6)$$

However, the equation for u_p must be modified since \bar{y} cannot be calculated. The modified equation for u_p is then the standard deviation of the error values as found from Equation 5.7; namely,

$$u_p = \sqrt{\frac{1}{N} \sum_{i=1}^N (e_i - \bar{e})^2}, \quad (5.7)$$

where

N = total number of data points in experimental data set and

e_i = normal distance between scanned point i and calibrated spline.

One or two standard deviations are equivalent to a coverage factor of $k=1$ or $k=2$, respectively. The denominator is changed to N , which is equal to the number of measured points, since the entire population of data instead of a sample is being used.

The geometric interpretation of this uncertainty source remains unchanged from that in Equation 5.5. This term accounts for how closely all the values are clustered.

Since no averaging is done on the actual data in this calculation, repeated measurements of the ring with a given set of parameters are not required in order to generate a first-

order estimate of the uncertainty. However, good measurement practice would be to repeat the experiment until the histogram converges. Mathematically, this means to add data until the standard deviation converges within an acceptable tolerance.

The uncertainty calculation is then conducted for each experimental data set, and an uncertainty for that speed determined. The results of this procedure are shown in Figure 5.20. As expected, the uncertainty increases with increasing speed. At slow speeds the uncertainty is under 0.001 mm. The uncertainty begins increasing once the natural frequency of the x-axis of the probe head is encountered during the scan, which occurs at speeds of 5 mm/s and greater. This region is noted as the region where resonance is possible on Figure 5.20. The large increase in uncertainty by an order of magnitude at speeds above 8 mm/s should be noted. This figure can be used to determine appropriate

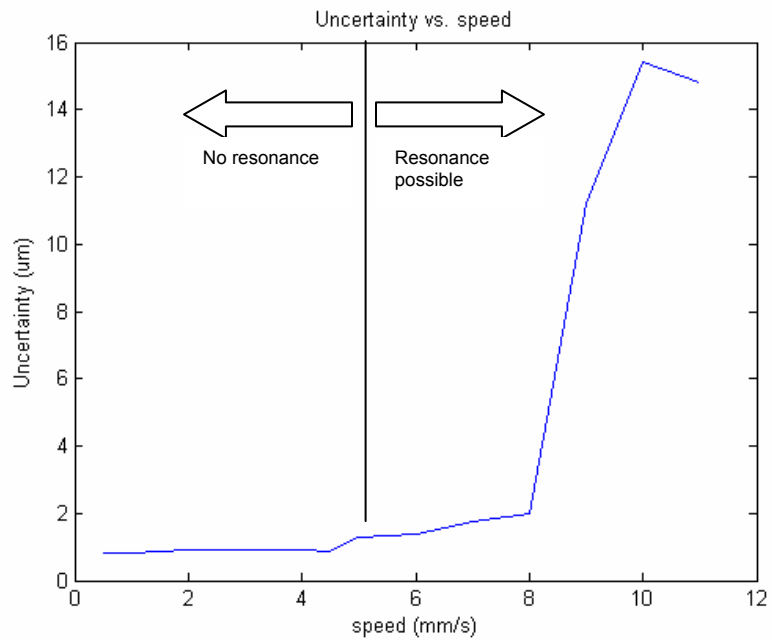


Figure 5.20: Uncertainty versus speed

operating speeds when wavelengths that encompass the range of the wavy ring must be measured.

The method described above is equally valid for determining a single uncertainty value for the measurement of the entire frequency spectrum of the ring or for establishing uncertainty bands for subsets of the waveform. This concept can therefore also be used to plot how the uncertainty varies over the range of frequencies within a single experiment. Figure 5.21 illustrates this concept and shows how the data are divided into four uncertainty bands. Each band contains approximately the same number of wavelengths. The bands contain the following wavelengths: 0.5-0.75mm, 0.75-1mm, 1-2

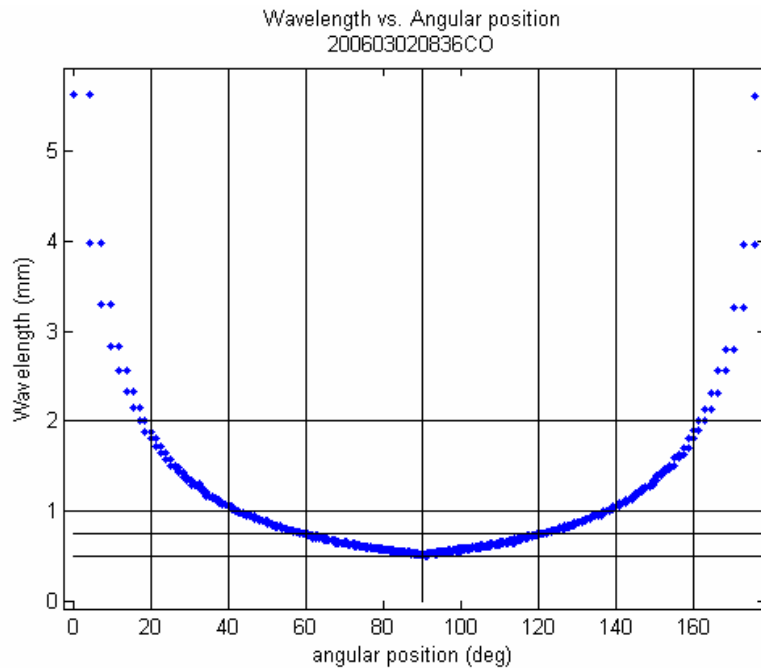


Figure 5.21: Uncertainty bands

mm, and 2-6 mm as shown by the horizontal lines in Figure 5.21. The angular divisions for each of these bands are shown by the vertical lines.

The errors for a given experimental data set can then be separated by band and plotted as shown in Figure 5.22. Although each speed was represented by a single uncertainty value in Figure 5.20, Figure 5.22 illustrates that the uncertainty at a given speed varies with wavelength. Measurements at the shorter wavelengths have a higher uncertainty. This figure allows an operator to determine whether a given speed is appropriate for measuring a subset of the wavelengths on the wavy ring.

A plot similar to Figure 5.22 is generated for each speed. These plots can then be combined into a plot such as that in Figure 5.23 that shows how the uncertainty increases

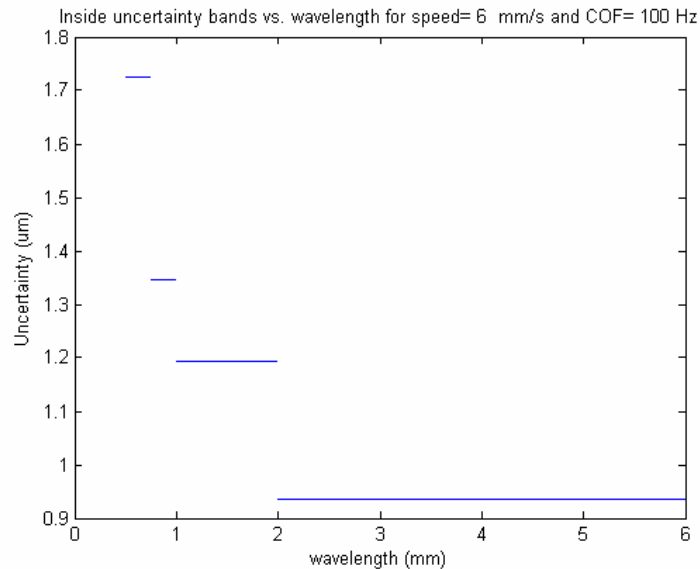


Figure 5.22: Uncertainty bands for a single speed

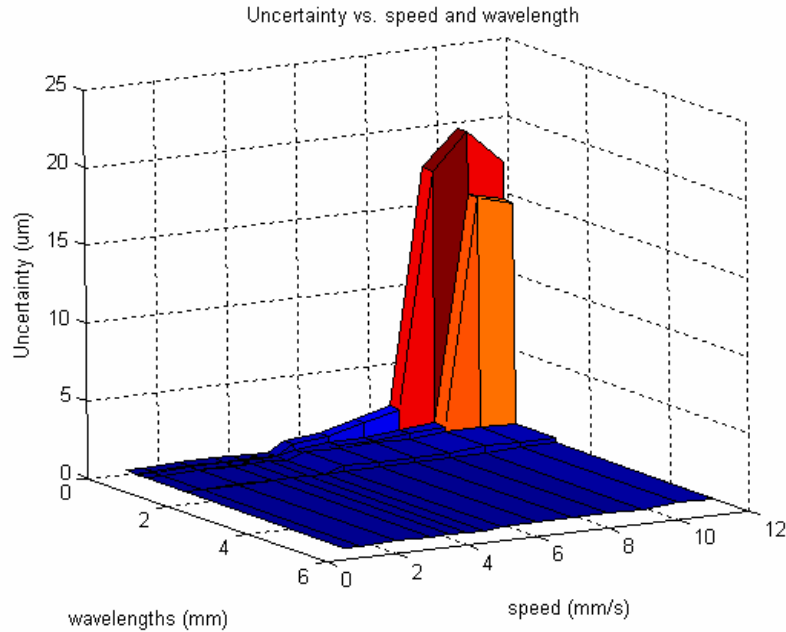


Figure 5.23: 3-D plot of uncertainty vs. wavelength and all scanning speeds

with increasing speed. The 3-D plot highlights the uncertainty bands present at each speed. From Figure 5.23, it is very clear that the region of peak uncertainty should be avoided. These high uncertainties occur at speeds of 9-11 mm/s. This plot can be used to determine that while these speeds may be acceptable for measuring long wavelengths, they are not suitable for short wavelength measurements.

The variations in uncertainty in the apparently almost planar region are dwarfed by the large uncertainties at the higher speeds. Therefore, the speeds from 0.5-8 mm/s are re-plotted in Figure 5.24. This figure shows the variation in uncertainty at these slower speeds. This figure can be used to select the highest speed that can be used to measure the wavelengths of interest with a given uncertainty. For example, if wavelengths down

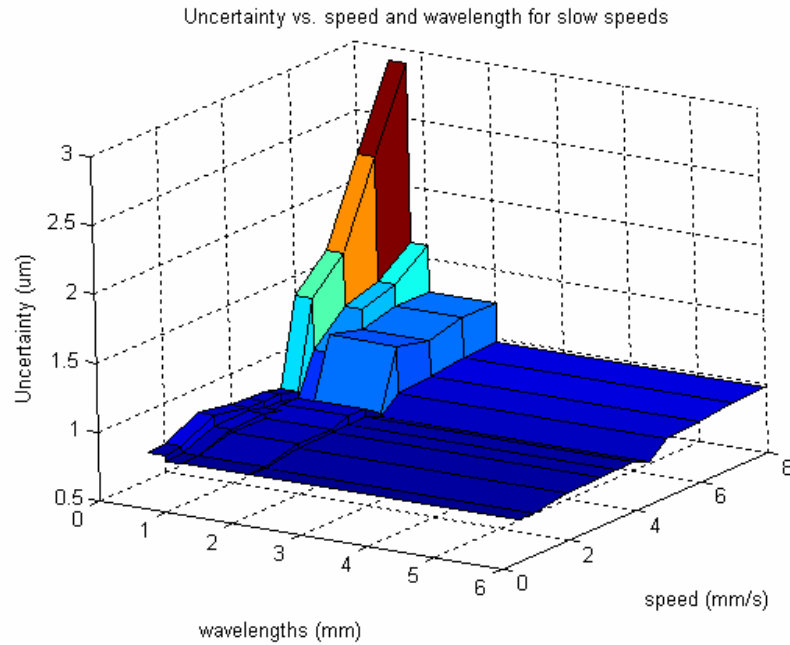


Figure 5.24: 3-D plot of uncertainty vs. wavelength and slower speeds

to 1 mm are of interest and the maximum uncertainty allowable, as determined by the metrologist, is 1 micrometer, then a maximum speed of 7 mm/s should be used.

5.2.4. Use of models to select scanning speed

The developed models provide a means for understanding the effect of scanning speed on measurement uncertainty for a given experimental set-up. The information in Figure 5.23 can be used to select the maximum scanning speed that provides the desired level of uncertainty. The desired measurement uncertainty is typically selected based on the tolerance of the measurement. This analysis shows how the ring can be used to experimentally determine the optimum scanning speed for a CMM system.

5.3. Experimental plan for scanning parameter selection

Using the techniques developed in this chapter, an appropriate scanning speed and filter cut-off frequency can be selected based on the desired measurement uncertainty and the wavelengths of interest. An experimental plan that would accomplish this task is summarized in the following steps:

1. Determine expected wavelength range of surface content from either expert opinion, point to point measurements, or very slow scan of surface.
2. Calculate probe head natural frequency in direction of interest as described in Section 4.1.5. Using this information and the minimum wavelength of interest selected in Step 1, determine maximum speed that will avoid natural frequency using Equation 4.5.
3. Characterize filter using techniques in Section 5.1.
4. Select filter that will not filter data at maximum speed but will filter system noise.
5. Determine maximum acceptable level of uncertainty.
6. Measure ring at increasing speeds up to the maximum allowable speed or to maximum speed before probe begins losing contact with surface. Use the slow speed scan data as reference data.
7. Calculate maximum speed that will provide desired uncertainty over wavelength range of interest using method described in Section 5.2.
8. Refine filter cut-off by selecting the lowest cut-off filter that will not filter data (to filter out higher frequency noise sources) at the selected speed.

6. Contributions and Future Work

6.1. Contributions

A number of fundamental contributions to the understanding of scanning CMM operations have been achieved. These include the following contributions that extend the capabilities of CMMs to measure surface texture with optimal speeds and low uncertainties:

1. A method for calibrating a wavy artifact is developed. This method includes the definition of the appropriate measurand and a calibration procedure. The measurand of deviations off the best fit circle allows for the scanning effects to dominate the measurement instead of CMM geometry errors.
2. An experimental procedure is developed that minimizes the scanning parameters that must be varied and isolates the key effects of speed and filtering. Algorithms and data analysis techniques that capture the scanning performance are developed.
3. Models of scanning operations focusing on filtering and speed effects are developed. These models are used to quantify scanning performance and the interaction of the probe and workpiece. Specifically, the filtering model is used to select a filter that filters the system noise but not the surface data at a given speed. The scanning speed model can be used to select a scanning speed that provides the fastest measurement for a given level of uncertainty. This quantifies the operating limits of the CMM in order to achieve the desired uncertainty.

4. A method for calculating the measurement uncertainty of a CMM making form measurements over a range of wavelengths is developed. This capability could reduce the number of inspection platforms on which a workpiece would need to be measured. A reduction in inspection platforms needed reduces both inspection costs and time.
5. A method for minimizing measurement uncertainty through the selection of optimum scanning parameters such as probe tip diameter, scanning speed, filter, and probing force is developed.
6. An understanding of the physics of the scanning probe and how these characteristics must drive scanning parameter selection is achieved. Specifically, the effect of the natural frequency on scanning performance is characterized.
7. A framework for future simulation of scanning is created. The models and methods developed in this work can be extended and built upon to model other aspects of CMM scanning operations.
8. A method for performance evaluation of CMMs used in scanning mode is created. The tests developed here could be incorporated into future standards that would allow users to select a CMM that would be most appropriate for their scanning application.
9. A method for evaluating whether an inspection platform can accurately measure the surface texture requirements specified on an engineering drawing is developed.

6.2. Future work

Many opportunities exist for further work in the area of modeling CMM scanning.

Future work could:

1. Develop theoretical models that capture the information in the empirical models presented here so that decisions on scanning parameters would not be dependent on experimental techniques. This would require modeling the probe and CMM controller. Additionally, a model of the interaction of the probe tip with the surface would be required.
2. Develop performance tests that are sensitive to scanning error sources. The models presented here could be incorporated into performance tests in standards to quantify performance with respect to scanning parameters such as scanning speed. The testing described in this dissertation would need to be simplified and condensed to a few key tests that would yield similar information. These models would provide the metrologist with much more information about a system's scanning capabilities than can be derived from the current international standard for scanning, ISO 10360-4, which was described in Section 2.3.2.
3. Determine how 2-D or 3-D scanning measurements would be affected by the different natural frequencies in the 2 or 3 axes used. In this dissertation only one axis of the probe head was used during scanning. Therefore, it was possible to avoid the natural frequency of this axis. This concept could be extended to the more general case of 3-D scanning. This case would also include errors generated by bulk machine motion and geometry errors.

4. Create an optimization framework that would select a variety of scanning parameters to optimize a measurement. This dissertation has described how scanning speed and filters should be selected. Other components of the optimization framework could determine the measurement strategy including the optimum workpiece orientation and scanning paths to minimize measurement uncertainty.
5. Develop active probes or nano-scale probes that could be used in scanning applications. Probe characterization could be based on the concepts presented in this dissertation.
6. Improve the servo control of the system based on the insight provided by the models developed here. This information could be used to improve the force control algorithms and filters used in the system.

List of References

[1] Swift, D., March 2002, "A Technology Decision Point for Dimensional Inspection in the NWC," (U) UCRL-ID-140962, Proc. of the *Non-Contact Inspection Workshop*, Aiken, SC.

[2] ISO 17025: 2005, "General Requirements for the Competence of Calibration and Testing Laboratories," International Organization for Standardization, Switzerland.

[3] ISO GUM, 1995, "Guide to the Expression of Uncertainty in Measurement," International Organization for Standardization, Switzerland.

[4] ANSI/NCSL Z540.2-1997 (R2002), "American National Standard for Expressing Uncertainty – U. S. Guide to the Expression of Uncertainty in Measurement," ANSI/NCSL, Boulder.

[5] ASME B89.7.5 – 2006, "Metrological Traceability of Dimensional Measurements to the SI Unit of Length," ASME, New York.

[6] ISO 14253-1: 1998, "Geometrical Product Specifications – Inspection by Measurement of Workpieces and Measuring Equipment Part 1: Decision Rules for Proving Conformance or Non-Conformance with Specifications," International Organization for Standardization, Switzerland.

[7] ASME B89.7.3.1 – 2001, "Guidelines for Decision Rules: Considering Measurement Uncertainty Determining Conformance to Specifications," ASME, New York.

[8] Phillips, S., March 2003, "Concepts and Applications of Measurement Uncertainty: An IDW Tutorial," *International Dimensional Workshop*, Knoxville, TN.

[9] Breyer, K., and Ohnheiser, R., 1994, "Length and Form Measurement on Coordinate Measuring Machines," Carl Zeiss, Oberkochen, Germany.

[10] ISO VIM, 1993, "International Vocabulary of Basic and General Terms in Metrology," International Organization for Standardization, Switzerland.

[11] ISO 14253-2: 1999, "Geometrical Product Specifications – Inspection by Measurement of Workpieces and Measuring Equipment Part 2: Guide to the estimation of uncertainty in GPS measurement, in calibration equipment and in product verification," International Organization for Standardization, Switzerland.

[12] Nielsen, H., "Managing Measurement Uncertainty," a Training Seminar, Oak Ridge, TN, June 19, 2002.

[13] Phillips, S. D., Estler, W. T., Doiron, T., Eberhardt, K. R., and Levenson, M. S., 2001, "A Careful Consideration of the Calibration Concept," *J. Res. Natl. Inst. Stand. Technol.*, **106**, pp. 371-379.

- [14] ASME B89.7.3.2 – 2007, “Guidelines for the Evaluation of Dimensional Measurement Uncertainty,” ASME, New York.
- [15] Phillips, S. D., Borchardt, B., Estler, W. T., and Buttress, J., 1998, “The Estimation of Measurement Uncertainty of Small Circular Features Measured by Coordinate Measuring Machines,” *Precision Engineering*, **22**, pp. 87-97.
- [16] Rasnick, B., Cox, B., and Sherrill, M., 1996, “Determination of Measurement Uncertainty on Coordinate Measuring Machines by Measurement Decomposition and Utilization of Canonical Artifacts,” Report Y/AMT-328, Y-12, Oak Ridge, TN.
- [17] Phillips, S. D., Borchardt, B.R., Sawyer, D. S., Estler, W.T., Ward, D.E., Eberhardt, K.R., Levenson, M.S., McClain, M., Melvin, B., Hopp, T., and Shen, Y., 1997, “The Calculation of CMM Measurement Uncertainty via The Method of Simulation by Constraints,” in Proceedings of *ASPE*, pp. 443-446.
- [18] Wilhelm, R. G., Hocken, R., and Schwenke, H., 2001, “Task Specific Uncertainty in Coordinate Measurement,” *Annals of the CIRP*, **50**(2), pp. 553-563.
- [19] Phillips, S. D., 1995, “Chapter 7: Performance Evaluations,” from *Coordinate Measuring Machines and Systems*, ed. J. Bosch, Marcel Dekker: New York,.
- [20] Lingard, P.S., Purss, M.E., Sona, C.M., Thwaite, E.G., and Mariasson, G.H., 1991, “Temperature Perturbation Effects in a High Precision CMM,” *Precision Engineering*, **13**, pp.41-51.
- [21] Rivin, E.I., 1995, “Vibration Isolation of Precision Equipment,” *Precision Engineering*, **17**, pp.41-56.
- [22] Singhose, W.E., Seering, W.P., and Singer, N.C., 1996, “Improving Repeatability of Coordinate Measuring Machines with Shaped Command Signals,” *Precision Engineering*, **18**, pp.138-146.
- [23] van Vliet, W. P., and Schellekens, P. H. J., 1998, “Development of a Fast Mechanical Probe for Coordinate Measuring Machines,” *Precision Engineering*, **22**, pp.141-152.
- [24] Carrier, P.W., and MacManus, R.A., July 16, 1996, “Vibration Damper for Coordinate Measuring Machine,” U.S. Patent 5,535,524, Assignee: Brown and Sharpe Manufacturing Company.
- [25] Helms, I.F., August 27, 1991, “Coordinate Measuring Machine with Vibration Damping System,” U.S. Patent 5,042,162, Assignee: Brown and Sharpe Manufacturing Company.

- [26] Schalz, K.J., February, 11, 1992, "Device and Method for Active Vibration Damping," U.S. Patent 5,086,564, Assignee: Wild Leitz GmbH.
- [27] Nai, K.C.H., July 2, 2002, "Method of and Apparatus for Reducing Vibrations on Probes Carried by Coordinate Measuring Machines," U.S. Patent 6,412,329, Assignee: Renishaw.
- [28] Bourdet, P., Lartigue, C., and Leveaux, F., 1993, "Effects of Data Point Distribution and Mathematical Model on Finding the Best-Fit Sphere to Data," *Precision Engineering*, **15**(3), pp.150-157.
- [29] Dowling, M.M., Griffin, P.M., Tsui, K.L., and Zhou, C., 1997, "Statistical Issues in Geometric Feature Inspection Using Coordinate Measuring Machines," *Technometrics*, **39**(1), pp.3-24.
- [30] ISO 10360, 2000 and 2001, "Geometrical Product Specifications – Acceptance and Reverification Tests for Coordinate Measuring Machines (CMM)," International Organization for Standardization, Switzerland.
Part 1: Vocabulary, 2000.
Part 2: CMMs Used for Measuring Size, 2001.
Part 3: CMMs with the Axis of the Rotary Table as the Fourth Axis, 2000.
Part 4: CMMs Used in Scanning Measuring Mode, 2000.
Part 5: CMMs Using Multiple-Stylus Probing Systems, 2001.
Part 6: Estimation of Errors in Computing Gaussian Associated Features, 2001.
- [31] ASME B89.4.1b-2001, "Methods for Performance Evaluation of Coordinate Measuring Machines," ASME, New York.
- [32] Cauchick-Miguel, P., King, T., and Davis, J., 1996, "CMM Verification: A Survey," *Measurement*, **17**(1), pp.1-16.
- [33] Genest, D. H., Jan. 1997, "The Right Probe Adds Versatility to CMMs," *Quality Digest*.
- [34] Renishaw, Dec. 2003, "Scanning Probes for Your CMM," <http://www.renishaw.com/client/product/UKEnglish/PGP-1070.shtml>.
- [35] Sutherland, A.T., and Wright, D.A., June 17, 2003, "Calibration of an analogue probe and error mapping," U.S. Patent 6,580,964, Assignee: Renishaw.
- [36] McMurty, D.R., Sutherland, A.T., and Wright, D.A., August 5, 2003, "Method of Calibrating a Scanning System," U.S. Patent 6,601,311, Assignee: Renishaw.
- [37] Cauchick-Miguel, P., King, T., and Abackerli, A., 1998, "A review on methods for probe performance verification," *Measurement*, **23**, pp.15-33.

- [38] Feng, C. X., and Pandey, V., Feb. 2002, "Experimental Study of Digitizing Parameters on Digitizing Uncertainty with a CMM," *International Journal of Production Research*, **40**(3), pp.638-697.
- [39] Tang, S. Y., and Sun, A., 2001, "An Analysis of CMM Scanning Measurement Uncertainty Using Design of Experiments," in *Proceedings of the 2001 Industrial Engineering Research Conference*, Paper No. 2045, Institute of Industrial Engineers, Norcross, GA.
- [40] Salsbury, J. G., Pereira, P. H., Muralidhar, A., Freire, A. S., and Hocken, R. J., May 8-11, 2000, "Performance of Scanning Coordinate Measuring Machines," *Proceedings of the 2000 International Dimensional Workshop*, Knoxville, TN.
- [41] Pereira, P. H., 2001 "Characterization and Compensation of Dynamic Errors of a Coordinate Measuring Machine," Dissertation, University of North Carolina at Charlotte, Charlotte, NC.
- [42] Farooqui, S. A., and Morse, E. P., 2004, "Alternative Artifacts for Evaluating Scanning CMM Performance," *Proceedings of the 2004 ASPE Annual Meeting*.
- [43] Wozniak, A., 2004, "An Investigation into the Dynamic Performance of CMM Scanning Probes," *Electronika*, **8**(9), pp.256-258.
- [44] Liang, R., Jusko, O., Lüdicke, F., and Neugebauer, M., 2001, "A Novel Piezo Vibration Platform for Probe Dynamic Performance Calibration," *Measurement Science and Technology*, **12**, pp.1509-1514.
- [45] Haitjema, H., and Kotte, G. J., 1997, "Dynamic Probe Calibration up to 10 kHz Using Laser Interferometry," *Measurement*, **21**(3), pp.107-111.
- [46] Jusko, O., and Lüdicke, F., 1999, "Novel Multi-Wave Standards for the Calibration of Form Measuring Instruments," *Proc. 1st EuSPEN*, Bremen, **2**, p. 299-302.
- [47] Jusko, O., Lüdicke, F., Wäldele, F., 2000, "High Precision Form Measurements with Coordinate Measuring Instruments," *Proc. X. International Colloquium on Surfaces*, Chemnitz.
- [48] Folkert, K. F., 2005, "Metrology Artifact Design," Thesis, North Carolina State University, Raleigh, NC.
- [49] Garrard, K. P., Dow, T. A., and Folkert, K. F., 2006, "Ring Gauge for Evaluation of CMM Dynamics," *Proceedings of the 2006 ASPE Annual Meeting*.
- [50] ASME Y14.5M-1994, "Dimensioning and Tolerancing," ASME, New York.

- [51] M. J. Roberts, 2001, *Signals and Systems: Analysis Using Transform Methods and MATLABTM*, McGraw-Hill: New York.
- [52] Dick, T. P., and Patton, C. M., 1995, *Calculus*, PWS Publishing: New York.
- [53] Fargo, F. T., 1968, *Handbook of Dimensional Measurement*, Industrial Press: New York.
- [54] Ogata, K., 2004, *System Dynamics Fourth Edition*, Prentice Hall: New Jersey.
- [55] Messtechnik Wetzlar GmbH, Feb. 2007, "Quindos 6," http://www.mtwz.com/index_en.html.
- [56] Mathworks, Inc., 2005, "MATLABTM (Version 7.1)," Computer Software, Massachusetts.
- [57] Rabiner, L. R., and Herrmann, O., 1973, "The Predictability of Certain Optimum Finite Impulse Response Digital Filters," IEEE Trans. on Circuit Theory, **CT-20**(4), pp.401-408.
- [58] Hamming, R. W., 1997, *Digital Filters Third Edition*, Dover Publications: New York.
- [59] Carlson, A. B., 1986, *Communication Systems: An Introduction to Signals and Noise in Electrical Communication*, McGraw-Hill: New York.
- [60] ISO 15530-3:2004, "Geometrical Product Specifications – Coordinate measuring machines: Technique for determining the uncertainty of measurement – Part 3: Use of Calibrated workpieces or standards," International Organization for Standardization, Switzerland.

Appendices

Appendix 1: Angular locations of calibration points

```
%%
%%%%%%%%%%%%%%%%%%%%%%%%%%%%%%%%%%%%%%%%%%%%%%%%%%%%%%%%%%%%%%%%%%%%%%%%
% %           Angular locations of calibration points for ring
% %           Pamela Murray
% %           Last updated: 9/15/06
% %           cal_spacing_dissertation.m
% %%%%%%%%%%%%%%%%%%%%%%%%%%%%%%%%%%%%%%%%%%%%%%%%%%%%%%%%%%%%%%%%%%%%%%%%%
close all
clear all

%NC State ring waveform
A=0.005 ;%starting signal amplitude (mm)
R=152.4/2; %inner radius in mm
L=(R*2)*pi/4; %length of one quadrant
f=10; %base frequency
d=200; %linear modulation parameter
N=36000; %total number of points in ring

n=N/4; % number of points per section
res=L/n; % spatial resolution
t1=0:res:L-res; % vector of distance samples

su = A*sin(2*pi/(L+00)* t1 .*(d/L.* t1 +f)); %low to high freq sweep
sd = -A*sin(2*pi/(L+00)*(L-t1).*(d/L.*(L-t1)+f)); %high to low freq
sweep
t = [t1 t1+L t1+2*L t1+3*L]; % concatenate to form swept wave for ring
theta=(t/R)*180/pi; %convert to angles
s = [su sd su sd];

% Calculate the number of waves around the ring
%"sign" has a +1 in the increment if the wave is positive there, 0 if
it is
%0, and a -1 if the wave is negative in that increment
for i=1:N
if s(i)<0
    sign(i)=-1;
else if s(i)==0
    sign(i)=0;
    else sign(i)=1;
end
end
end

%"change" contains a 1 in each of the N-1 increments where the sign
%changes - this is where a 0 crossing occurs
for i=1:N-1
    if sign(i)<=0
        if sign(i+1)>0
            change(i)=1;
        else change(i)=0;
        end
end
```

```

        else if sign(i)>0
            if sign(i+1)<=0
                change(i)=1;
            else change(i)=0;
            end
        end
    end
end
end

%"index" contains the indices that contain 0 crossings
%Note: these are the indices that contain a 1 in "change"
index=0;
for i=1:N-1
    if change(i)==1
        index=[index i];
    end
end
length_index=length(index);
index=index(2:length_index);

%"lines" contains the indices that separate waves
%Note: every other zero crossing separates waves
lines=0;
for i=1:2:length(index)
    lines=[lines index(i)];
end
length_lines=length(lines);
lines=lines(2:length_lines);
lines=[lines N];

%Calculate the angles for calib. so each wave has 2^n points
a=(length(lines)-1)/4; %a=number of waves per quadrant
fprintf('The ring has %g waves in one quadrant.\n',a)

%Find theta increments for su
n=5; %will give 2^n points/wave

%for su
for i=1:(a*(2^n))
    increment=(i-1)/(2^n);
    p=[d f*L -increment*(L^2)];
    r=roots(p);
    pos=r>=0;
    tup(i)=r(pos);
    %thetaup(i)=(tup(i)/R)*(180/pi); %in degrees
end
%plot(tup, '.')
%plot(thetaup)

%low to high freq sampled sweep
sunew=A*sin(2*pi/(L+00)* tup.*(d/L.* tup +f));

%for sd

```

```

for i=2:(a*(2^n)+1)
    increment=(i-1)/(2^n);
    p=[d f*L -increment*(L^2)];
    r=roots(p);
    pos=r>=0;
    tdown(i-1)=L-r(pos);
end
tdown=fliplr(tdown);

tnew = [tup tdown+L tup+2*L tdown+3*L]; %length locations for
calibration
thetaneu=(tnew/R)*180/pi; %these are the radial locations that should
be probed in the calibration

%put thetaneu in text file
fid = fopen('thetas32.txt','w');
fprintf(fid,'%3.6f\n',[thetaneu]);
fclose(fid);

%create clearance points angles (space half way between prb)
j=0;
for i=1:length(thetaneu)
    otheta(i+j)=thetaneu(i);
    j=j+1;
end
for i=1:(length(thetaneu)-1)
    otheta(2*i)=thetaneu(i)+(thetaneu(i+1)-thetaneu(i))/2;
end

fid = fopen('othetas32.txt','w');
fprintf(fid,'%3.6f\n',[otheta]);
fclose(fid);

%plot calibration density on wave
figure(1)
hold on
%plot wave
%plot(theta,s)
plot(t1,su,tup,suneu,'b.')
title('Sample Location vs. Angular Position')
xlabel('Angular Position (deg)')
ylabel('Deviation (mm)')

```


Appendix 2: Ring calibration program

IO2NIST.WDB

```
*****
*****
*                                     *
*           PROGRAM - LISTING           *
*                                     *
*****
*****
```

```
LOAD
OPEN C:\IO2NIST.TXT, D1
LISTING , D1
!*****Ring 2 Calibration Program***
!*****
!Setup
GOTO 1000
!Probe and rotary table calibration
GOTO 2000
!Establish coordinate systems
GOTO 3000
!Measure
GOTO (LAB=4000)
!*****
!Setup
1000:CONTIN
!Setup instructions provided in "Setup for wavy ring measurements" 3/7/06
!Read all slides before beginning
!Check for equipment listed on slide 2
!Define and use parameter set for M48 (if needed)
STOP
DFNCMM
USECMM

!*****
!Probe and rotary table calibration
2000:CONTIN
!***PROBE CALIBRATION
DSBRTMOV
DSBRTCSY
!Mount 5/8 inch calibration sphere as shown on slide 4
!edit value below if using different cal sphere
```

```

DFNNOR (VAL=0.625*25.4)
!Confirm that probe is configured as shown in Slide 3
!Install probe so that .4 dia tip points in machine +x as shown on Slide 4
!Take CLP and PRB with 3mm tip for REFPRB.
REFPRB , , , , , , -3.8*25.4, , 3, , PRB(1), , , , , , , , Y, , , , 2
!Execute PRB(2) calibration - NPTs are there.
CALSPH PRB(2), .402, , , , , , 3, , 0, 0
LISPRB LDBPRB:PRB(1)
LISPRB LDBPRB:PRB(2)

!Rotary table calibration (slide 5)
!Follow all notes in help text
USEPRB PRB(1)
ENBRTMOV
!**edit dia of rot table cal sphere as needed***
AUTRTCSY (NRP=(0,45,90,135,180,225,270,315), DIA=.75*25.4, PSP=2, SAF=2)
STOP
ENBRTCSY
!*****
!Establish coordinate systems
3000:CONTIN

!Orient, center, and fixture ring as shown in slides 6 and 7
!Let epoxy cure for 45 minutes before beginning manual set-up

!Manual coordinate system
~DEL=YY
USECSY REFR$CSY
!Measure 3 points w/ PRB(1) on top of ring with CLP before the first (Slide 8)
USEPRB (NAM=PRB(1))
MEPLA MAN_PLA, , REFR$CSY, , (NOE), , , , , , , , , ~DEL
!Measure 3 points w/PRB(1) on smooth circle on inside of ring (Slides 9 and 10)
MECIR MAN_CIR, , REFR$CSY, REFR$CSY.$XY, (NOE), , , , , , , , , ~D
< EL
!Measure 4 points w/ PRB(1) in 1/4 inch bore closest to notch (Slide 11)
!This is the bore marked with 2 on top
MECIR MAN_CIR_SM, , REFR$CSY, REFR$CSY.$XY, (NOE), , , , , , , , ,
< , , ~DEL
COLPTS MAN_AXI, REFR$CSY, Y, (MAN_CIR,MAN_CIR_SM)
!Calculate axis through center of circle and center of bore
MEAXIXY MAN_AXI, , REFR$CSY, , (NOM,NOE)
!Build coordinate system
BLDCSY CSY(1), , REFR$CSY, MAN_PLA, +Z, , MAN_AXI, +X, , MAN_CIR, ,
MAN_CIR,
< , MAN_PLA

```

USECSY CSY(1)
STOP
!Move probe above ring (slide 12)
EDTTXT HEADER

!*****AUTOMATIC MEASURE SECTION*****

!Do not begin until epoxy has cured for a minimum of 2 hours

4000:CONTIN

!Measure per slide 13

INDPRC AUTO_RUN

SAVE , , , , , C:\IO2NIST.WDB

STOP

!Check for files per slide 14

!Take photos per slide 15

AUTO_RUN Procedure

!**AUTO START HERE

!**AUTO START HERE

!**AUTO START HERE

!Automatic coordinate systems

USEPRB PRB(1)

ENBRTMOV

ENBRTCSY

USECMM SLOWER_A

USECSY CSY(1)

GENCIR AUTO_PLA, 0, 0, 0, 160, 17, XY, P, 0, 360, 3, CSY(1), , , 25

MEPLA (NAM=AUTO_PLA, CSY=CSY(1))

MOVCM (RTP=0, DST=(0,0,15))

GENCIR AUTO_CIR, 0, 0, -4, 152.251, 17, XY, I, 0, 360, 3, CSY(1), , , 25

MECIRXY (NAM=AUTO_CIR, CSY=CSY(1))

MEPNT KLEER(1), , CSY(1), , (NOC,NOE)

GENCIR AUTO_CIR_SM, 89.2, 0, -4, 7, 6, XY, I, 0, 360, 5, CSY(1), , , 15, , 0

MECIRXY (NAM=AUTO_CIR_SM, CSY=CSY(1))

COLPTS (NAM=AUTO_AXI, CSY=CSY(1), ELE=(AUTO_CIR,AUTO_CIR_SM))

MEAXIXY (NAM=AUTO_AXI, CSY=CSY(1), MOD=(NOM,NOE))

MOVCM (RTP=0, DST=(0,0,15))

!Build cartesian csy

BLDCSY CSY(2), , CSY(1), AUTO_PLA, +Z, , AUTO_AXI, +X, , AUTO_CIR, ,
AUTO_CIR, , AUTO_PLA

!Build cylindrical csy

BLDCSY CSY(3), CYL, CSY(1), AUTO_PLA, +Z, , AUTO_AXI, +X, , AUTO_CIR, ,
AUTO_CIR, , AUTO_PLA

USECSY (NAM=CSY(3))

```

!STOP

!*****
4000:CONTIN
!Measure inside
!Select small probe and coordinate system
USECSY (NAM=CSY(3))
USEPRB (NAM=PRB(2))
MOVCOMM (RTP=0, TYP=ABS, DST=(0,0,100))

!Find beginning of wave
!GENCIR STARTER, , , -10, 152.25, 200, , , 0, 25, .4, CSY(3), , , , 25, , , , , 180
!MECIR STARTER, , CSY(3)
!EDTNPT STARTER
!
!SSSSSSSSSSSSSS
!From analysis of data, the 0 location is at 4.2743 degrees
!Rotate csy by 4.2743 degrees
! ring 1
!BLDTRA ROT_ANGLE, , 0, 0, 0, 4.274303, Z
! ring 2

BLDTRA ROT_ANGLE, , 0, 0, 0, 8.79741, Z
TRACSY CSY(4), ROT_ANGLE, CSY(3)
USECSY CSY(4)

!Generate probing points in theta4 element
!CNVFIL C:\QDSCMM\IN32.TXT, ELE
!EDTNPT IN32
!GENPTS IN32, 1, 99999, 1, I, 152.2/2, , X, , ALT
!GENPTS IN32, 1, 99999, 1, I, -12.5, , Z, , ALT
!GENPTS IN32, 1, 99999, 1, I, 180-Y$VAL, , R, , ALT
! ring 1
!GENPTS IN32, 1, 99999, 1, I, R$VAL-4.2743, , R, , ALT
! ring 2
!GENPTS IN32, 1, 99999, 1, I, R$VAL-8.79741, , R, , ALT
!EDTNPT IN32
!GENPTS IN32, 1, 99999, 1, I, 1, , U, , ALT
!GENPTS IN32, 1, 99999, 1, I, 180+Y$VAL, , V, , ALT
!GENPTS IN32, 1, 99999, 1, I, 0, , W, , ALT
!DO I, 1, 99999, 1
!PUTSTR , IN32.NOM.PTS(I), T, ELE, , , 'PRB'
!ENDDO

FMETIME IN32START, , MM/DD/YYYY hh:mm

```


DELCSY LDBCSY:*(), N
DELREA LDBREA:*(), N
DELCHS LDBCHS:*(), N

!END AUTO HERE
!END AUTO HERE
!END AUTO HERE

Appendix 3: Ring calibration report

REPORT OF CALIBRATION

NIST Test No. 821/273679-06

Amended: January 31, 2007

For: (1) Wavy Ring CMM Artifact

Page 1 of 6

Serial Number: 2

This wavy ring CMM artifact has been measured using an error-mapped coordinate measuring machine in combination with a precision rotary table. The CMM is housed in a constant humidity measurement environment where room temperature is controlled to 20.00 ± 0.05 ° C. Historical measurement processes employ several parts. The artifact is measured multiple times in a specific table location to generate short-term repeatability data and to sample artifact geometry and surface finish effects. NIST control standards are also measured concurrently to develop statistical long-term reproducibility data for the measurement system. The artifact was mounted to the rotary table with three raised feet and using a light application of epoxy. No restrictive or clamping devices were used. The average artifact temperature during the measurements was 20.008 ° C. The measurand results are reported at the temperature of 20.000 ° C.



Figure 1.



Figure 2.

The measurand is defined as the deviations from the best fit circle applied to the data collected using the QUINDOS programs and probe configuration provided and supplied by the customer. Accuracy of the program's function is the responsibility of the customer. Figure 1 shows the setup of the artifact on the CMM table and the orientation of the probe head. The results are supplied to the customer on the computer CD with the M8638 data label shown in Figure 2 and signed by a signatory of this report. This written report does not contain results within its pages.

Report continued, page 2 of 6
NIST Test No. 821/273679-06
Group Control No. M8638 Amended
Amended: January 31, 2007

The best fit radius for the inside surface measurement of the artifact is 76.11564 millimeters.**
The best fit radius for the outside surface measurement of the artifact is 101.71266 millimeters.**

These values are corrected for pressure fluctuations and closure related errors and represent the least squares average of the data collected at each surface.

The uncertainty of this measurement result was calculated according to NIST Technical Note 1297, "Guidelines for Evaluating and Expressing the Uncertainty of NIST Measurement Results," and the ISO document "Guide to the Expression of Uncertainty in Measurement", considered to be parts of this report. The expanded uncertainty, U , using a coverage factor of $k = 2$, is $\pm 0.382 \mu\text{m}$. A detailed error budget is included in the following pages.

This report shall not be reproduced except in full without the written approval of the Engineering Metrology Group.

Measurements made by _____ (301) 975-3468.

John R. Stoup

For the Director,
National Institute of Standards and Technology

Dr. Theodore D. Doiron, Group Leader
Engineering Metrology Group
Precision Engineering Division
Manufacturing Engineering Laboratory

Purchase Order No. 4300050772
Group Control No. M8638
Date: June 26, 2006

**** The original reported values were corrected for an error in the environmental compensation calculations. New data was also added to the CD files as requested by the client.**

Uncertainty budget for M48 1D & 2D Calibrations

1. Machine Positional and Scale Uncertainty

The external calibration laser and on-machine laser scales were set to the same wavelength compensation number. The only sources of error in the machine map are the reproducibility of the map, index of refraction difference between the two laser paths, difference in laser frequencies and interpolation errors between measured points of the map.

Along the X and Y axes, the positional and scale uncertainty is assessed by analyzing the error map of positional errors as measured by gridplate and ballplate rotation assessments. The historical average standard deviation of the positional errors is about 0.040 μm . The zerodur double corner cube artifact yielded 0.042 μm which was used for this analysis. This also includes the variations due to the probe form error that is sampled during the artifact rotation and repositioning.

The temperature difference between the two beams is quite small. In fact the temperature difference between any points near the table is less than 0.02 $^{\circ}\text{C}$, giving an associated error of 0.02 $\mu\text{m}/\text{m}$. Taking this as the half width of a rectangular distribution we get a standard uncertainty of 0.01 $\mu\text{m}/\text{m}$. The atmospheric pressure difference between the two beams, about 100 mm apart in height, is negligible.

The vacuum laser frequencies were the same to a few parts in 10^{-8} . We have taken 2×10^{-8} as an estimate of the standard uncertainty from this source. The error map smoothness is quite good and linear interpolation between the measured points, 25 mm apart, is indistinguishable from the map reproducibility cited above.

2. Control Artifacts and Historical Length Dependent Reproducibility

We have measured gages on the same machine for over 5 years and have both check standard data (over 200 calibrations of 900 mm, 20 inch steel gage blocks and a 42 inch Zerodur end standard) as well as multiple calibrations of check standard ring and plug gages. Analysis of the check standard data show the reproducibility (1σ) level is 0.040 $\mu\text{m} + 0.040 \times 10^{-6} L$. The A term is already counted in line 1 of the budget. We will include the calibration history of the primary measurement spheres used by the CMM to determine the probe diameter. The historical standard uncertainty of these spheres is 0.008 μm . These terms also include the probing repeatability.

3. Wavelength Compensation

The wavelength compensation has two parts. First the current wavelength is calculated from the atmospheric pressure, temperature and humidity using stand alone monitors and loaded into the

Report continued, page 4 of 6
NIST Test No. 821/273679-06
Group Control No. M8638 Amended

computer. During the run, the wavelength compensation is updated using internal recalculations and re-measurements of the environmental components. The sources of error are therefore: the Edlén Equation to convert pressure, temperature and humidity to wavelength correction, and the uncertainty in pressure, temperature and humidity used in the equation. The old Edlén equation was estimated to have a systematic error of about 5×10^{-8} . The new equation based on the refractometry of air work at NPL is stated to be accurate to about 3×10^{-8} .

Since the environmental sensors have had multiple calibrations during the time span of the check standards and customer histories, the variability due to these sensors will eventually be adequately sampled in the reproducibility data. Currently, however, we have less than 10 recalibrations of the temperature, pressure, and humidity instruments that make up the weather station. The thermometer calibration history shows the thermistors “as found” condition at calibration to have a standard deviation of 0.006 °C. Using this and the dependence of the refractive index on the temperature we get a standard length uncertainty of 6×10^{-9} . The standard uncertainty in pressure, derived from the “as found” condition on calibration over the last two years, of 10 Pa gives a length uncertainty of 3×10^{-8} , and the humidity uncertainty of 4% gives a length uncertainty of 4×10^{-8} .

4. Thermal Expansion Correction

There are two sources of uncertainty associated with thermal expansion: the uncertainty in the thermometer measurement and the uncertainty in the value of the thermal expansion coefficient. The system uses thermocouples referenced to a calibrated SPRT. The uncertainty in this system has been tested by measurements against other calibrated SPRTs. The standard uncertainty from these comparisons is estimated to be 2 mK. Multiple thermometers are placed on or in each artifact. Temperature differences along artifacts are generally under 4 mK, and corrections are applied for larger differences. The uncertainty in the thermal expansion coefficient of the artifact depends on the artifact. For steel artifacts of unknown origins we will take the uncertainty to be $1 \times 10^{-7}/^{\circ}\text{C}$. The uncertainty in the length measurement due to temperature and CTE effects is less than $2 \times 10^{-9}/^{\circ}\text{C}$.

5. Contact Deformation

Since the probe is calibrated using a steel sphere the deformation is only the same for the master sphere and the artifact when the materials match. The deformation can be calculated using the formula of Puttock and Thwaite (CSIRO Report, 1967). The deformation of a sphere-sphere contact has been calculated independently at NIST, and checked experimentally. No statistically significant differences have been found between experimental and theoretical results. For steel artifacts, this results in a standard uncertainty of 0.005 μm .

6. Atmospheric Pressure Fluctuations During Data Collection

The coordinate measuring machine can not make intermediate corrections to the wavelength in air while it is executing measurement commands. For very long data collection routines, this can allow drift in the environmental conditions to affect the quality of the collected data if the laser beam deadpath is long. This type of effect from humidity and temperature drifts can be negligible for these laboratories; however air pressure drifts must be corrected due to the impact on the wavelength. For the measurement of this wavy ring artifact, the data collection required several days of continuous measurement during which the air pressure changes could not be corrected. Independent monitoring of the air pressure developed a 6th order polynomial correction curve to be applied to the finished results. Deviations from this curve were never more than 200 Pascals for either the internal or external surface data collection. Using an average laser beam deadpath of 500mm and a rectangularly distributed error, this equates to a standard uncertainty due to uncorrected pressure fluctuations of 0.150 μm .

7. Closure Error for 360 Degree Rotational Data Sets

For long data collection routines, there can be positional drift of the rotary table and coordinate measuring machine coordinate systems. Under normal operating conditions over 12 hour spans of time, these drifts rarely exceed 0.100 μm to 0.150 μm . Historical analyses of larger drifts indicate that a linear approximation is usually a satisfactory estimate if the drifts exceed 0.250 μm . This is usually indicative of a disturbance in the thermal equilibrium of the machine environment. A range of $\pm 0.150 \mu\text{m}$ is estimated as the deviation from the linear function fitted to these larger drifts. Using the rectangular distribution estimate, the standard uncertainty of this source is estimated to be $\pm 0.087 \mu\text{m}$.

8. Rotary Table Error

The precision rotary table used on the M48 CMM has three error sources associated with its rotary positioning function. The table has a $\pm 0.040 \mu\text{m}$ cyclical error that appears to have 400 cycles per revolution. This is most likely related to the mechanism used for precisely rotating and then stopping the table motion. In addition to this, a large frequency rotational error of $\pm 0.100 \mu\text{m}$ has been observed through measurements of a primary hemisphere standard of known roundness. These errors are not accurately mapped at this time so their effects will be estimated using rectangularly distributed errors within these described ranges. The combination of these errors gives a standard uncertainty of 0.062 μm . The table also has a radial positioning accuracy of approximately $\pm 0.5 \text{ sec}$. when traveling along one direction. The highest radial position sensitivity on the wavy ring is about 0.050 $\mu\text{m}/\text{arcsec}$. These combine to give a worst case length error of $\pm 0.025 \mu\text{m}$.

ERROR BUDGET CALCULATION

In order to present an uncertainty statement of the form (A+BL) we calculate the uncertainty for short artifacts by summing the squares of the length independent sources and take the square root to be (A). We then sum all of the sources using L as 1 meter and take the square root to be (A+B) and solve for B. This procedure overestimates the uncertainty for the intermediate lengths slightly, but is necessary if we are to have a linear uncertainty statement. For the case of the wavy ring, we did not make a standard two-point measurement, therefore the length dependent term does not apply.

Wavy Ring Uncertainty Budget (L is in meters)

Factor #	Source	μm	ppm
1a	Machine Positioning Uncertainty	0.042	
1b	Temperature difference in beam paths during calibration		0.01
1c	Laser Frequency Difference		0.02
2	Mastering Artifact and Historical Length Dependent Performance	0.008	0.04
3a	Edlén Equation		0.03
3b	Index of Refraction – Air Temperature		0.01
3c	Index of Refraction - Air Pressure		0.03
3d	Index of Refraction – Humidity		0.04
4a	Thermal Expansion		0.05
4b	Coefficient of Thermal Expansion		0.05
5	Deformation Corrections	0.005	
6	Pressure Fluctuation Corrections	0.150	
7	Closure Error	0.087	
8a	Rotary Table Error	0.062	
8b	Length Error from Radial Positioning Uncertainty	0.025	
	Total Standard Uncertainty, u_c ($k = 1$)	0.191	0.10*L

U (μm) = 0.382 μm ($k = 2$)

Appendix 4: Experimental scanning program

```
*****
*****
*
*          PROGRAM - LISTING          *
*
*****
*****
```

```
!*****Ring Measurement Program***
!*****
!Setup
GOTO 1000
!Probe calibration
GOTO 2000
!Establish coordinate systems
GOTO 3000
!Measure inside
GOTO 4000
!Plot
GOTO 4500
!Measure outside
GOTO 5000
!Calculate surface points
GOTO 6000
!*****
!Setup
1000: CONTIN
INSKWD
DELCMM  GDBCMM:SAVE$CMM, N
DELCMM  LDBCMM:SAVE$CMM, N
DELCMM  EDBCMM:SAVE$CMM, N
!Create new parameter set
CRECMPAR (NAM=GDBCMM:SAVE$CMM, IPA=LFPS)
AUTZER
!PMGMGCSY
USEMGCSY (NAM=GDBCSY:MG$CSY)
!Select magazine position of probe in head. -1=no probe in head
SETMAGA (MGZ=001)
SETMAGA (MGZ=201)
SETMAGA (MGZ=-1)
DFNNOR  (VAL=29.9932)
!Check scanning parameters
```

TSCMCO (OPR=READ, TXT=INIFILE, CMD='SHOW INIFILE')
TSCMCO (OPR=READ, TXT=CONF, CMD='SHOW CONFIG')
EDTTXT (NAM=INIFILE)
EDTTXT (NAM=CONF)

!*****

!Probe calibration
2000: CONTIN
~DEL=Y
REFPRB_P (XOF=0, YOF=0, ZOF=-80, DIA=5, PRB=PRB(1), MGZ=001,
DEL=~DEL, SNT=TRX, DFT=3)
!PTODEV (STR='ENABLE CMPARAM', DEV=CM)
!Change probing offset: distance along normal to offset off surf before probing
!for probe calibration
PTODEV (STR='PRBLPA ,,2', DEV=CM)
!PTODEV (STR='DISABLE CMPARAM', DEV=CM)
!Calibrate probes 2 and 3
~DEL05=N
CALSPH (NAM=PRB(2), DIA=.5, DFT=2, MGZ=201, AZI=180, ELV=-45,
SNT=TRX, DEL=~DEL05, UAD=Y)
MOVCM (TYP=DLT, DST=(0,0,100))
CALSPH (NAM=PRB(3), DIA=1, DFT=2, MGZ=101, AZI=180, ELV=-45,
ANG=(30,0,0), SNT=TRX, DEL=~DEL05, UAD=Y)
MOVCM (TYP=DLT, DST=(0,0,100))
!Reset offset back to .5
!PTODEV (STR='ENABLE CMPARAM', DEV=CM)
PTODEV (STR='PRBLPA ,,0.5', DEV=CM)
!PTODEV (STR='DISABLE CMPARAM', DEV=CM)
STOP
USEPRB (NAM=PRB(1))
USECSY (NAM=REFR\$CSY)
!MOVCM (RTP=0, TYP=ABS, DST=(400,400,300))
AUTRTCSY (DIA=29.9932, SAF=1, DEL=Y)
USERTCSY
ENBRTMOV
MOVCM (RTP=0, DST=(0,0,200))
STOP

!***** MANUAL CSY *****

!Establish coordinate systems
3000: CONTIN
~DEL=NN
~DEL=YY
!top of ring
MEPLA (NAM=MAN_PLA, CSY=REFR\$CSY, MOD=(NOE), DEL=~DEL)

```

!smooth circle on inside
MECIR (NAM=MAN_CIR, CSY=REFR$CSY, PRO=REFR$CSY.$XY,
MOD=(NOE), DEL=~DEL)
!top counter bore
MECIR (NAM=MAN_CIR_SM, CSY=REFR$CSY, PRO=REFR$CSY.$XY,
MOD=(NOE), DEL=~DEL)
COLPTS (NAM=MAN_AXI, CSY=REFR$CSY, DEL=Y,
ELE=(MAN_CIR,MAN_CIR_SM))
!Axis through center of circle and center of counterbore
MEAXIXY (NAM=MAN_AXI, CSY=REFR$CSY, MOD=(NOM,NOE))
BLDCSY (NAM=CSY(1), REF=REFR$CSY, SPA=MAN_PLA, SDR=+Z,
PLA=MAN_AXI, PDR=+X, XZE=MAN_CIR, YZE=MAN_CIR, ZZE=MAN_PLA)
USECSY (NAM=CSY(1))
LISCSY CSY(1)
!***** AUTO CSY *****

GENCIR (NAM=AUTO_PLA, XCO=0, YCO=0, ZCO=0, DIA=160, NPT=12,
PLA=XY, INO=P, MIP=0, MXP=360, PDI=3, CSY=CSY(1), ZVL=25)
MEPLA (NAM=AUTO_PLA, CSY=CSY(1))
MOVCMML 0, , (0,0,15)
GENCIR (NAM=AUTO_CIR, XCO=0, YCO=0, ZCO=-4, DIA=152.251, NPT=12,
PLA=XY, INO= I, MIP=0, MXP=360, PDI=3, CSY=CSY(1), ZVL=25)
MECIRXY (NAM=AUTO_CIR, CSY=CSY(1))
GENCIR (NAM=AUTO_CIR_SM, XCO=89.2, YCO=0, ZCO=-4, DIA=13.646,
NPT=6, PLA=XY, INO=I, MIP=0, MXP=360, PDI=5, CSY=CSY(1), ZVL=15, RTP=0)
MECIRXY (NAM=AUTO_CIR_SM, CSY=CSY(1))
COLPTS (NAM=AUTO_AXI, CSY=CSY(1), ELE=(AUTO_CIR,AUTO_CIR_SM))
MEAXIXY (NAM=AUTO_AXI, CSY=CSY(1), MOD=(NOM,NOE))
TRAOBJ (NEW=AUTO_AXI, OLD=AUTO_AXI, ANG=71.15, AXI=Z,
REF=CSY(1))

!Build cartesian csy
BLDCSY (NAM=CSY(2), REF=CSY(1), SPA=AUTO_PLA, SDR=+Z,
PLA=AUTO_AXI, PDR=+X, XZE=AUTO_CIR, YZE=AUTO_CIR,
ZZE=AUTO_PLA)

MOVCMML (RTP=0, DST=(0,0,15))
!Build cylindrical csy
BLDCSY (NAM=CSY(3), TYP=CYL, REF=CSY(1), SPA=AUTO_PLA, SDR=+Z,
PLA=AUTO_AXI, PDR=+X, XZE=AUTO_CIR, YZE=AUTO_CIR,
ZZE=AUTO_PLA)

STOP
USECSY CSY(3)
!*****Measure inside*****

```



```

4000: CONTIN
!Select probe
USECSY CSY(2)
USEPRB (NAM=PRB(2))
MOVCOMM (RTP=0, TYP=ABS, DST=(0,0,100))
PTODEV (STR='COFREQ 100', DEV=CM)

!Modify PDI for probe selected
GENSCACIR (NAM=CIR(1), PLA=XY, INO=I, TYP=CIR, XCO=0, YCO=0, ZCO=-
12.5, DIA=152.25, DNS=50, SPD=11, PDI=0.5, MIP=0, MXP=360, DEL=Y,
CSY=CSY(2))
!GENSCACIR , CIR(1), XY, I, CIR, 0, 0, -12.5, 152.25, 50, 2, , 0.5, 0, 360, , Y, , , ,
CSY(3)
PUTVALS (OBJ=CIR(1).NOM.PTS(2), RDS=R, VAL=180-71.15)
PUTVALS (OBJ=CIR(1).NOM.PTS(3), RDS=R, VAL=178-71.15)
TRAELE (NEW=CIR(1), TRA=CSY(3), OLD=CIR(1), TYP=CSY)
EDTNPT CIR(1)
CPYOBJ (FRM=CIR(1), TO =CIR_NKOFI(1), TYP=ELE)
MECIRXY (NAM=CIR(1), CSY=CSY(3), MOD=(NOC,NOE))
CPYOBJ (FRM=CIR(1), TO =DVMOUT(1))
!just calc and eval
MECIRXY (NAM=CIR(1), CSY=CSY(3), MOD=NOM)
!"No filter"
PTODEV (STR='COFREQ 200', DEV=CM)

!use noc, noe so will still have dvm (head deflections) in vector columns
MECIRXY (NAM=CIR_NKOFI(1), CSY=CSY(3), MOD=(NOC,NOE))

!Analyze data
PTODEV (STR='COFREQ 100', DEV=CM)
CPYOBJ (FRM=CIR_NKOFI(1), TO =DVMOUT_NKOFI(1))
MECIRXY (NAM=CIR_NKOFI(1), CSY=CSY(3), MOD=NOM)

!translate to cartesian coords for plotting
TRAELE (NEW=XY_CIR(1), TRA=CSY(2), OLD=CIR(1), TYP=CSY)
TRAELE (NEW=XY_CIR_NKOFI(1), TRA=CSY(2), OLD=CIR_NKOFI(1),
TYP=CSY)
MECIRXY (NAM=XY_CIR(1), CSY=CSY(2), MOD=NOM)
MECIRXY (NAM=XY_CIR_NKOFI(1), CSY=CSY(2), MOD=NOM)
!Copy force data to different element for data analysis
CPYOBJ (FRM=DVMOUT(1), TO =XY_(1))
CPYOBJ (FRM=DVMOUT_NKOFI(1), TO =XY_NK(1))
!find number of scan points (j) in a calculated element
GETVAL (NAM=CIR_PTS(1), OBJ=CIR(1), DSC=j)
GETVAL (NAM=CIRNK_PTS(1), OBJ=CIR_NKOFI(1), DSC=j)

```

```

!modify points in dvm element to add point numbers into field D
GENPTS (NAM=XY_(1), BGN=1, END=CIR_PTS(1), DLT=1, VNA=I, FUN=I,
DSC=D, TYP=APT, MOD=ALT)
!CPYOBJ XY_(1), XY_MM(1)
!Convert deflection to grams
!SFM=Spring force multiplier=conversion from mm to g
!MTK4 has spring constant of 1.8N/mm
SFM=185
GENPTS (NAM=XY_(1), BGN=1, END=CIR_PTS(1), DLT=1, VNA=I,
FUN=SFM*FSQR(U$VAL*U$VAL+V$VAL*V$VAL+W$VAL*W$VAL), DEL=N,
DSC=A, TYP=APT, MOD=ALT)
!GENPTS XY_MM(1), 1, CIR_PTS(1), 1, I,
FSQR(U$VAL*U$VAL+V$VAL*V$VAL+W$VAL*W$VAL), N, A, APT, ALT
GENPTS (NAM=XY_NK(1), BGN=1, END=CIRNK_PTS(1), DLT=1, VNA=I,
FUN=I, DSC=D, TYP=APT, MOD=ALT)
GENPTS (NAM=XY_NK(1), BGN=1, END=CIRNK_PTS(1), DLT=1, VNA=I,
FUN=SFM*FSQR(U$VAL*U$VAL+V$VAL*V$VAL+W$VAL*W$VAL), DEL=N,
DSC=A, TYP=APT, MOD=ALT)
!Sort points in increasing angular order to improve plotting
SRTAPT (NAM=CIR(1), ORI=CIR(1), CRI=Y)
SRTAPT (NAM=XY_(1), ORI=XY_(1), CRI=Y)
!SRTAPT XY_MM(1), XY_MM(1), Y
SRTAPT (NAM=CIR_NKOFI(1), ORI=CIR_NKOFI(1), CRI=Y)
SRTAPT (NAM=XY_NK(1), ORI=XY_NK(1), CRI=Y)
STOP

!*****Plot*****
!Circular plot of data
!to do: fix no. pts. and inspector, date, and time on plot
RNDNES_P (ELE=XY_CIR(1), OPN=N, FAC=1000)
RNDNES_P (ELE=XY_CIR_NKOFI(1), OPN=N, FAC=1000)

4500: CONTIN
!Strip plot of data
!Describe plot
~DESCRIPTION='filtered RT scan of inside with .5mm probe'
~DESCRIPTION='unfiltered RT scan of inside with .5mm probe'
!Select scan data to plot
~SCAN_DATA=CIR(1)
~SCAN_DATA=CIR_NKOFI(1)
~SCAN_DATA=OCIR(2)
~SCAN_DATA=OCIR_NKOFI(2)
!Select force data to plot
~FORCE_DATA=XY_(1)
~FORCE_DATA=XY_NK(1)

```

```

~FORCE_DATA=OXY_(2)
~FORCE_DATA=OXY_NK(2)
!Plot all data
INDPRC PLOT_ALL
!Select range of data to plot
MINANG=80
MAXANG=100
INDPRC PLOT_PART

!Return to outside measurement section
GOTO 5500

!Complete inside measurement section
FMTOBJ (FIL=C:\QUINDOS6LIB\RING\CIR(1).TXT, NAM=CIR(1), TYP=ELE)
FMTOBJ (FIL=C:\QUINDOS6LIB\RING\CIR_NKOFI(1).TXT,
NAM=CIR_NKOFI(1), TYP=ELE)
FMTOBJ (FIL=C:\QUINDOS6LIB\RING\DVMOUT(1).TXT, NAM=DVMOUT(1),
TYP=ELE)
FMTOBJ (FIL=C:\QUINDOS6LIB\RING\DVMOUT_NKOFI(1).TXT,
NAM=DVMOUT_NKOFI(1), TYP=ELE)
STOP
SAVE (SCB=Y, FIL=C:\QUINDOS6LIB\RING\RING.WDB)
DELAPT ELE:*( ), N

!*****OUTSIDE*****
5000:CONTIN
!Select probe
USEPRB (NAM=PRB(2))
MOVCM (RTP=0, TYP=ABS, DST=(0,0,100))
MOVCM (RTP=0, TYP=ABS, DST=(200,0,100))
USECSY (NAM=CSY(2))
PTODEV (STR='COFREQ 5', DEV=CM)

!Modify PDI in GENSCACIR for probe tip size
GENSCACIR (NAM=OCIR(2), PLA=XY, INO=O, TYP=CIR, XCO=0, YCO=0,
ZCO=-12.5, DIA=203.5, DNS=50, SPD=3.5, PDI=0.5, MIP=0, MXP=360, DEL=Y,
CSY=CSY(2))
PUTVALS (OBJ=OCIR(2).NOM.PTS(2), RDS=R, VAL=360-71.15)
PUTVALS (OBJ=OCIR(2).NOM.PTS(3), RDS=R, VAL=358-71.15)
!PUTVALS OCIR(2).NOM.PTS(3), , R, 358
TRAELE (NEW=OCIR(2), TRA=CSY(3), OLD=OCIR(2), TYP=CSY)
EDTNPT (NAM=OCIR(2))
CPYOBJ (FRM=OCIR(2), TO =OCIR_NKOFI(2), TYP=ELE)
MECIRXY (NAM=OCIR(2), CSY=CSY(3), MOD=(NOC,NOE))
CPYOBJ (FRM=OCIR(2), TO =ODVMOUT(2))

```

```

!calc and eval
MECIRXY (NAM=OCIR(2), CSY=CSY(3), MOD=NOM)
PTODEV (STR='COFREQ 200', DEV=CM)
MECIRXY (NAM=OCIR_NKOFI(2), CSY=CSY(3), MOD=(NOC,NOE))

!Data analysis
!switching back to filtered
PTODEV (STR='COFREQ 5', DEV=CM)
CPYOBJ (FRM=OCIR_NKOFI(2), TO=ODVMOUT_NKOFI(2))
MECIRXY (NAM=OCIR_NKOFI(2), CSY=CSY(3), MOD=NOM)
TRAELE (NEW=OXY_CIR(2), TRA=CSY(2), OLD=OCIR(2), TYP=CSY)
TRAELE (NEW=OXY_CIR_NKOFI(2), TRA=CSY(2), OLD=OCIR_NKOFI(2),
TYP=CSY)
!re-calc in Cartesian csy
MECIRXY (NAM=OXY_CIR(2), CSY=CSY(2), MOD=NOM)
MECIRXY (NAM=OXY_CIR_NKOFI(2), CSY=CSY(2), MOD=NOM)
!Copy data to different element for data analysis
CPYOBJ (FRM=ODVMOUT(2), TO=OXY_(2))
CPYOBJ (FRM=ODVMOUT_NKOFI(2), TO=OXY_NK(2))
!find number of points (j) in a calculated element
GETVAL (NAM=OCIR_PTS(2), OBJ=OCIR(2), DSC=j)
GETVAL (NAM=OCIRNK_PTS(2), OBJ=OCIR_NKOFI(2), DSC=j)
!modify points in dvm element to add point numbers into field D
!and Convert deflection to grams
!SFM=Spring force multiplier=conversion from mm to g
!MTK4 has spring constant of 1.8N/mm
SFM=185
GENPTS (NAM=OXY_(2), BGN=1, END=OCIR_PTS(2), DLT=1, VNA=I, FUN=I,
DSC=D, TYP=APT, MOD=ALT)
GENPTS (NAM=OXY_(2), BGN=1, END=OCIR_PTS(2), DLT=1, VNA=I,
FUN=SFM*FSQR(U$VAL*U$VAL+V$VAL*V$VAL+W$VAL*W$VAL), DEL=N,
DSC=A, TYP=APT, MOD=ALT)
GENPTS (NAM=OXY_NK(2), BGN=1, END=OCIRNK_PTS(2), DLT=1, VNA=I,
FUN=I, DSC=D, TYP=APT, MOD=ALT)
GENPTS (NAM=OXY_NK(2), BGN=1, END=OCIRNK_PTS(2), DLT=1, VNA=I,
FUN=SFM*FSQR(U$VAL*U$VAL+V$VAL*V$VAL+W$VAL*W$VAL), DEL=N,
DSC=A, TYP=APT, MOD=ALT)
!Sort points in increasing angular order to improve plotting
SRTAPT (NAM=OCIR(2), ORI=OCIR(2), CRI=Y)
SRTAPT (NAM=OXY_(2), ORI=OXY_(2), CRI=Y)
SRTAPT (NAM=OCIR_NKOFI(2), ORI=OCIR_NKOFI(2), CRI=Y)
SRTAPT (NAM=OXY_NK(2), ORI=OXY_NK(2), CRI=Y)

STOP
!Plot roundness charts

```

```

CONDEVPL
RNDNES_P (ELE=OXY_CIR(2), FAC=2000)
RNDNES_P (ELE=OXY_CIR_NKOFI(2), FAC=2000)
CUTDEVPL
!Go to strip chart plotting section
GOTO 4500
!Return from strip chart plotting section
5500: CONTIN
!Clean-up, clean-up
FMTOBJ (FIL=C:\QUINDOS6LIB\RING\OCIR(2).TXT, NAM=OCIR(2),
TYP=ELE)
FMTOBJ (FIL=C:\QUINDOS6LIB\RING\OCIR_NKOFI(2).TXT,
NAM=OCIR_NKOFI(2), TYP=ELE )
FMTOBJ (FIL=C:\QUINDOS6LIB\RING\ODVMOUT(2).TXT,
NAM=ODVMOUT(2), TYP=ELE)
FMTOBJ (FIL=C:\QUINDOS6LIB\RING\ODVMOUT_NKOFI(2).TXT,
NAM=ODVMOUT_NKOFI(2), TYP=ELE)
STOP
SAVE (SCB=Y, FIL=C:\QUINDOS6LIB\RING\RING.WDB)
DELAPT (NAM=ELE:*(), CNF=N)

!*****Find surface points*****
6000:CONTIN
!Put probe radius in deviation field
GETVALS (OBJ=XY_CIR(2), RDS=j, REA=NUM_PTS)
GENPTS (NAM=XY_CIR(2), BGN=1, END=NUM_PTS, DLT=1, VNA=A, FUN=-
.25, DEL=N, DSC=A, TYP=APT, MOD=FUN)
!shift along normal vector by deviation
SHFPTS (SRC=XY_CIR(2), DST=XY_CIR(9), STY=APT, MOD=DVI)
!Verify shfpts command
EDTAPT (NAM=XY_CIR(2))
EDTAPT (NAM=XY_CIR(9))
!Develop mask
CVMSKTXT (TXT=TESTMASK, MSK=PMSAPTTT)
EDTTXT (NAM=TESTMASK)
CNVTXT (NAM=TESTMASK)
LISAPT (NAM=XY_CIR(9),MSK=XYZ_ONLY)
OPEN (FIL=D:\INSIDE_DATA.TXT, DEV=D1, DCH=*)
LISAPT (NAM=XY_CIR(9), DEV=D1, MSK=XYZ_ONLY)
CLOSE (DEV=D1)

```

Appendix 5: Format data for MATLAB analysis

```
!*****
!****FILTERAPTS.WDB****
!****Program to put APTs in correct format for MATLAB analysis of filter****
!****Gives 2 columns of data: 1st=angular position, 2nd=deviations from circle
!****Input: date of files of interest
!****Output 2 text files containg APTs for scans with and w/o cut-off filter
!****Pamela Murray 3/10/06
!*****

!Create mask (first time only)
!CVMSKTXT APTMSK, PM$APTTT
!EDTTXT APTMSK
!CNVTEXT APTMSK
0001: CONTIN
STOP
!Edit date information for files of interest
~YEAR=2006
~MONTH=03
~DAY=02
~TIME=1351
!Hit gold-execute for the correct side
!Measured inside
GOTO 2000
!Measured outside
GOTO 3000

!*****
!Inside measurement section
2000: CONTIN
CONCAT ~DATE, (~YEAR,~MONTH,~DAY,~TIME), 1
!This works as long as there is only one .wdb in the folder
CONCAT ~LOADFILE,
(\\YCFS1\DIMENSIONALS\NCSTATE_RING\RING_DATA\',~DATE,'*.WDB'), 1
LOAD , TDBELE:CIR(1), , , , N, ~LOADFILE
LOAD , TDBELE:CIR_NKOFI(1), , , , N, ~LOADFILE
CONCAT ~SAVECO, ('C:\MATLAB701\WORK\RING\',~DATE,'CO.TXT'), 1
CONCAT ~SAVENCO, ('C:\MATLAB701\WORK\RING\',~DATE,'NCO.TXT'), 1
!Save APTs to files in correct format - select based on in/outside
OPEN ~SAVECO, D1, , , *
LISAPT CIR(1), D1, , , APTMSK
CLOSE , D1
OPEN ~SAVENCO, D1, , , *
LISAPT CIR_NKOFI(1), D1, , , APTMSK
CLOSE , D1
```

```

!delete elements and strings to prepare for running with next data set
DELELE CIR(1), N
DELELE CIR_NKOFI(1), N
DELCHS ~DATE, N
DELCHS ~LOADFILE, N
DELCHS ~SAVECO, N
DELCHS ~SAVENCO, N
GOTO 0001

!Measred outside
3000: CONTIN
CONCAT ~DATE, (~YEAR,~MONTH,~DAY,~TIME), 1
!This works as long as there is only one .wdb in the folder
CONCAT ~LOADFILE,
(\\YCF51\DIMENSIONAL$NCSTATE_RING\RING_DATA\',~DATE,'*.WDB'), 1
!if measured outside
LOAD , TDBELE:OCIR(2), , , , N, ~LOADFILE
LOAD , TDBELE:OCIR_NKOFI(2), , , , N, ~LOADFILE
CONCAT ~SAVECO, ('C:\MATLAB701\WORK\RING\',~DATE,'CO.TXT'), 1
CONCAT ~SAVENCO, ('C:\MATLAB701\WORK\RING\',~DATE,'NCO.TXT'), 1
!Save APTs to files in correct format - select based on in/outside
OPEN ~SAVECO, D1, , , *
LISAPT OCIR(2), D1, , , APTMSK
CLOSE , D1
OPEN ~SAVENCO, D1, , , *
LISAPT OCIR_NKOFI(2), D1, , , APTMSK
CLOSE , D1
!delete elements and strings to prepare for running with next data set
DELELE OCIR(2), N
DELELE OCIR_NKOFI(2), N
DELCHS ~DATE, N
DELCHS ~LOADFILE, N
DELCHS ~SAVECO, N
DELCHS ~SAVENCO, N
GOTO 0001

SAVE , , , , , , \\TECHDEV2\TECHDEV\PM5\PROJECTS\UNIV_RELATIONS\
NCSU\FILTERAPTS.WDB

```

Appendix 6: Amplitude ratio vs. frequency

```
% %%%%%%%%%%%%%%%%%%%%%%%%%%%%%%%%%%%%%%%%%%%%%%%%%%%%%%%%%%%%%%%%%%%%%%%%%%
% %                                     filter_definition.m: Filter Analysis
% %                                     Pamela Murray
% %                                     Last updated: 3/14/06
% %%%%%%%%%%%%%%%%%%%%%%%%%%%%%%%%%%%%%%%%%%%%%%%%%%%%%%%%%%%%%%%%%%%%%%%%%%

close all
clear all
A=0.005 ;%starting signal amplitude (mm)
R=152.3/2; %inner radius in mm
L=(R*2)*pi/4; %length of one quadrant
%terms to generate wave taken from NCSU selected to give wavelengths of
%interest (.2mm to 2 mm) and so waveforms match up approximately
f=10; %base frequency
d=200; %linear modulation parameter
N=40000; %total number of points in ring
n=N/4; % number of points per section
res=L/n; % spatial resolution
t1=0:res:L-res; % vector of distance samples
% generate low to high sweep
su = A*sin(2*pi/(L+00)* t1 .*(d/L.* t1 +f));
% generate high to low frequency sweep
sd = -A*sin(2*pi/(L+00)*(L-t1).*(d/L.*(L-t1)+f));
% concatenate sequences to form swept wave for ring
t = [t1 t1+L t1+2*L t1+3*L];
theor_theta=(t/(2*R))*360/pi;
theor_s = [su sd su sd];

%%%%%%%%%%%%%%%%%%%%%%%%%%%%%%%%%%%%%%%%%%%%%%%%%%%%%%%%%%%%%%%%%%%%%%%%%
%Edit data below to evaluate experimental results
year='2006';
month='03';
day='23';
time='1339';
side='Inside';
speed=11; %mm/s
filter='NCO'; %CO or NCO
cof=200; %Hz
%%%%%%%%%%%%%%%%%%%%%%%%%%%%%%%%%%%%%%%%%%%%%%%%%%%%%%%%%%%%%%%%%%%%%%%%%

date=strcat(year,month,day,time);
file=strcat(date,filter);
path=strcat('c:\MATLAB701\work\ring\',file, '.txt');
D=importdata(path);
theta=D(:,1);
s=D(:,2);
N=length(s);

%"sign" has a +1 in the increment if the wave is positive there, 0 if
it is
%0, and a -1 if the wave is negative in that increment
for i=1:N
if s(i)<0
    sign(i)=-1;
```



```

else if s(i)==0
    sign(i)=0;
    else sign(i)=1;
    end
end
end

%"change" contains a 1 in each of the N-1 increments where the sign
%changes - this is where a 0 crossing occurs
for i=1:N-1
    if sign(i)<=0
        if sign(i+1)>0
            change(i)=1;
        else change(i)=0;
        end
    else if sign(i)>0
        if sign(i+1)<=0
            change(i)=1;
        else change(i)=0;
        end
    end
end
end
end

%"index" contains the indices that contain 0 crossings
%Note: these are the indices that contain a 1 in "change"
index=0;
for i=1:N-1
    if change(i)==1
        index=[index i];
    end
end
length_index=length(index);
index=index(2:length_index);

%"lines" contains the indices that separate waves
%Note: every other zero crossing separates waves
lines=0;
for i=1:2:length(index)
    lines=[lines index(i)];
end
length_lines=length(lines);
lines=lines(2:length_lines);
lines=[lines N];

%plot wave
figure(1)
hold on
plot(theta,s)
title({'Deviation vs. Position';file})
xlabel('position (deg)')
ylabel('deviation (mm)')
hold on

```

```

%plot lines to separate waves
for i=1:length(lines)
    location=lines(i);
    x=[theta(location) theta(location)];
    y=[-.005 .005];
    plot(x,y,'r-')
    hold on
end

%plot min/max within each wave
%calculate amplitude, amplitude ratio, and wavelength of each wave
for i=1:length(lines)-1
    min_index=lines(i);
    max_index=lines(i+1);
    y_temp=s(min_index:max_index);
    [y,c]=max(y_temp);
    plot(theta(c+min_index-1),y,'g*')
    [z,d]=min(y_temp);
    plot(theta(d+min_index-1),z,'g*')
    amplitude(i)=y-z;
    amplitude_ratio(i)=(y-z)/(2*A);
    wavelength_deg(i)=theta(max_index)-theta(min_index);
    wavelength(i)=wavelength_deg(i)*2*pi*R/360;
    frequency(i)=speed/wavelength(i);
end
hold off

figure(2)
%sort frequencies and ratios and plot
[sorted_frequency,order] = sort(frequency,2);
% order the amplitude ratio like the frequency
ordered_ratio=zeros(1,length(frequency));
for i=1:length(frequency)
    ordered_ratio(i)=amplitude_ratio(order(i));
end
plot(sorted_frequency,ordered_ratio,'.')
topline=strcat(side, ' Amplitude Ratio vs. Frequency: Speed= ',num2str(speed), ' mm/s and COF= ',num2str(cof), ' Hz');
title({topline;file})
xlabel('frequency (Hz)')
ylabel('amplitude ratio')
%plot COF location
hold on
cofx=[cof cof];
fy=[0 1];
plot(cofx,fy,'r')
%plot range of input frequencies
min_input_freq=speed/6.24;
max_input_freq=speed/.531;
minfreqx=[min_input_freq min_input_freq];
maxfreqx=[max_input_freq max_input_freq];
hold on
plot(minfreqx, fy,'g')
hold on

```

```
plot(maxfreqx,fy,'g')
%axis([0 1.5 0 1.2]);
hold off
print('-f2', '-djpeg90', file);
```

Appendix 7: Theoretical filter characterization

```
% %%%%%%%%%%%%%%%%%%%%%%%%%%%%%%%%%%%%%%%%%%%%%%%%%%%%%%%%%%%%%%%%%%%%%%%%%%
% %          filter_sysid5.m: data for system id - Final version
% %          Pamela Murray Moor
% %          Last updated: 2/5/07
% %%%%%%%%%%%%%%%%%%%%%%%%%%%%%%%%%%%%%%%%%%%%%%%%%%%%%%%%%%%%%%%%%%%%%%%%%%
close all
clear all
% %%%%%%%%%%%%%%%%%%%%%%%%%%%%%%%%%%%%%%%%%%%%%%%%%%%%%%%%%%%%%%%%%%%%%%%%%%
%Import filtered data
year='2006';
month='03';
day='02';
time='0852';
side=' Inside';
speed=5; %mm/s
filter='NCO'; %CO or NCO
cof=3; %Hz
date=strcat(year,month,day,time);
file=strcat(date,filter);
%path=strcat('C:\MATLAB701\work\RING\',file,'.txt'); %work
path=strcat('C:\Program Files\MATLAB_SV71\work\ring\',file,'.txt');
D=importdata(path);
theta=D(:,1);
s=D(:,2);
N=length(s);
thetai=0:.0135:360;
si = interp1(theta,s,thetai,'cubic');
Ni=length(si);
% %%%%%%%%%%%%%%%%%%%%%%%%%%%%%%%%%%%%%%%%%%%%%%%%%%%%%%%%%%%%%%%%%%%%%%%%%%
%Import unfiltered data
uyear='2005';
umonth='11';
uday='11';
utime='1530';
uside=' Inside';
uspeed=.5; %mm/s
ufilter='CO'; %CO or NCO
ucof=5; %Hz
udate=strcat(uyear,umonth,uday,utime);
ufile=strcat(udate,ufilter);
%upath=strcat('C:\MATLAB701\work\RING\',ufile,'.txt'); %work
upath=strcat('C:\Program Files\MATLAB_SV71\work\ring\',ufile,'.txt');
%home
uD=importdata(upath);
utheta=uD(:,1);
us=uD(:,2);
uN=length(us);
uthetai=0:.0135:360;
usi = interp1(utheta,us,uthetai,'cubic');
uNi=length(usi);
%correct interpolation at end of series
for i=26639:26667
```

```
    usi(i)=usi(26638);  
end
```

Appendix 8: Digital filter characterization

```
%digital_filter2.m
%Digital filter selection

function Hd = digital_filter2
%DIGITAL_FILTER2 Returns a discrete-time filter object.

%
% M-File generated by MATLAB(R) 7.1 and the Signal Processing Toolbox
6.4.
%
% Generated on: 05-Feb-2007 22:11:01
%

% Equiripple Lowpass filter designed using the FIRPM function.

% All frequency values are in Hz.
Fs = 248.65; % Sampling Frequency

Fpass = 1.8; % Passband Frequency
Fstop = 5; % Stopband Frequency
Dpass = 0.02; % Passband Ripple
Dstop = 0.25; % Stopband Attenuation
dens = 20; % Density Factor

% Calculate the order from the parameters using FIRPMORD.
[N, Fo, Ao, W] = firpmord([Fpass, Fstop]/(Fs/2), [1 0], [Dpass,
Dstop]);

% Calculate the coefficients using the FIRPM function.
b = firpm(N, Fo, Ao, W, {dens});
Hd = dfilt.dffir(b);
```

Appendix 9: Uncertainty analysis

```
% %%%%%%%%%%%%%%%%%%%%%%%%%%%%%%%%%%%%%%%%%%%%%%%%%%%%%%%%%%%%%%%%%%%%%%%%%%
% %                               Wavy Ring Uncertainty Analysis
% %                               unc_analysis_final.m
% %                               Pamela Murray Moor
% %                               Last updated: 2/25/07
% %%%%%%%%%%%%%%%%%%%%%%%%%%%%%%%%%%%%%%%%%%%%%%%%%%%%%%%%%%%%%%%%%%%%%%%%%%
close all
clear all
begin_time=clock
%%%%%%%%%%%%%%%%%%%%%%%%%%%%%%%%%%%%%%%%%%%%%%%%%%%%%%%%%%%%%%%%%%%%%%%%%
%Edit data below to import measured data
%This data has been centered and had the radius fixed in Quindos to
agree
%with the following data sets
%2005: 200511111530CO .5 mm/s, COF=5 Hz r=152.3410, x=.0012, y=.0001
%2006: 200603021032 1 mm/s, COF=3 Hz r=152.2291, x=0, y=.0001
year='2006';
month='03';
day='02';
time='0836';
side=' Inside ';
speed=4.5; %mm/s
filter='CO'; %CO or NCO
cof=10; %Hz

%Select correct year for experimental data set
%fit fast data to slow center and radius

meas_radius=152.3410/2; %mm 2005 .5 mm/s
meas_radius=152.2291/2; %mm 2006 1mm/s
cal_radius=meas_radius;
%%%%%%%%%%%%%%%%%%%%%%%%%%%%%%%%%%%%%%%%%%%%%%%%%%%%%%%%%%%%%%%%%%%%%%%%%
date=strcat(year,month,day,time);
file=strcat(date,filter);
fprintf(1,'Loading measured data...\n');
path=strcat('c:\MATLAB701\work\ring\',file,'_ITCONT.txt'); %work
%path=strcat('C:\Program
Files\MATLAB_SV71\work\ring\',file,'_ITCONT.txt'); %home
M=importdata(path);
%meas_theta=M(:,1)+2.363;
%ori_meas_theta=M(:,1)+2.363;
meas_theta=M(:,2)+2.363;
ori_meas_theta=M(:,2)+2.363;
%meas_dev=M(:,2);
meas_dev=M(:,3);
meas_N=length(meas_dev);

fprintf(1,'Converting measured data...\n');
%calculate total radii by adding back in LSBF radius
```

```

for i=1:meas_N
    scaled_meas_r(i)=meas_radius+meas_dev(i); %surface data
end

%Import calibration data
fprintf(1,'Loading calibration data...\n');
D=importdata('c:\MATLAB701\work\nistcalbyy12method.txt'); %work
%D=importdata('C:\Program
Files\MATLAB_SV71\work\ring\nistcalbyy12method.txt'); %home
cal_theta=D(:,1); %this data has already been rotated by 180 degrees to
line up with internal cal data
cal_dev=D(:,2);
cal_N=length(cal_dev);
%cal_radius=76.116036; %mm %using slow speed radius instead
%calculate total radii by adding back in LSBF radius
fprintf(1,'Converting calibration data...\n');
for i=1:cal_N
    cal_r(i)=cal_radius+cal_dev(i); %surface points
end

n_samples=50; %number of sampled points between each two cal points
order=5; %polynomial order
%for each measured point, find 6 nearest neighbors
fprintf(1,'Processing...\n');
for i=1:meas_N %for each measured point
    rot_angle=90-meas_theta(i);
    meas_theta=meas_theta+rot_angle;
    cal_theta=cal_theta+rot_angle;
    [meas_x,meas_y] = pol2cart(meas_theta*pi/180,scaled_meas_r);
    [cal_x,cal_y] = pol2cart(cal_theta*pi/180,cal_r);
    if mod(i,500)==0
        fprintf(1,'Evaluating measured point %i of %i... \n',i,meas_N)
    end
    for j=1:cal_N %calculate the distance from the measured point to
each calibrated point
        delta_x=meas_x(i)-cal_x(j);
        delta_y=meas_y(i)-cal_y(j);
        dist(j)=sqrt(delta_x^2+delta_y^2);
    end
    %find 6 closest calibrated points
    [sorted_dist,k] = sort(dist); %sorts in ascending order
    for m=1:6
        p=k(m);
        nearest_thetas(m)=cal_theta(p);
        nearest_devs(m)=cal_r(p);
        % Find closest XY cal points
        nearest_cal_x(m)=cal_x(p);
        nearest_cal_y(m)=cal_y(p);
    end
    % Find X span of closest cal points
    min_cal_x=min(nearest_cal_x);
    max_cal_x=max(nearest_cal_x);

    min_theta=min(nearest_thetas);

```



```

max_theta=max(nearest_thetas);
sorted_thetas = sort(nearest_thetas);

% Calculate polynomial through nearest calibrated XY points
[p_xy,s_xy,mu_xy] = polyfit(nearest_cal_x,nearest_cal_y,order);
% Generate points along the range of nearest calibrated X points
x_samples = min_cal_x:(max_cal_x-min_cal_x)/5000:max_cal_x; % MAY
NEED TO CHANGE TO A CONSTANT NUMBER OF X SAMPLES
% Compute polynomial points for each of the above
f_samples = polyval(p_xy,x_samples,[],mu_xy);
%f_samples = spline(nearest_cal_x,nearest_cal_y,x_samples);
% Compute distances between the measured point
% and each polynomial point
for q=1:length(x_samples)
    dist_xy(q)=sqrt((x_samples(q)-meas_x(i))^2 + (f_samples(q)-
meas_y(i))^2);
end
% Find the index of the smallest distance
[sorted_dist_xy, index] = sort(dist_xy);
error_xy(i) = sorted_dist_xy(1);
    if i==5800
%         % Plot all cal and measured data with shortest distance to
one
%         point drawn as line
        figure(1)
        % Plot measured data
        plot(meas_x(i),meas_y(i), 'ro');hold on;
        plot(meas_x,meas_y, 'r. ');hold on;
        % Plot calibrated data
        plot(cal_x,cal_y, 'b. ');hold on;
        plot(nearest_cal_x,nearest_cal_y, 'bo');hold on;
        % Plot polynomial
        plot(x_samples,f_samples, 'g.- ');hold on;
        %plot a line to the nearest point
        line_x = [meas_x(i) x_samples(index(1))];
        line_y = [meas_y(i) f_samples(index(1))];
        plot(line_x, line_y, 'r- ');hold on;
%         % Plot a line to the next nearest point
%         line_x = [meas_x(i) x_samples(index(2))];
%         line_y = [meas_y(i) f_samples(index(2))];
%         plot(line_x, line_y, 'm- ');hold on;
        topline=strcat(side, ' Calibrated and Scanned data: Speed=
',num2str(speed), 'mm/s and COF= ',num2str(cof), 'Hz');
        title({topline;file})
        xlabel('x (mm)')
        ylabel('y (mm)')
    end
    hold off

end %end main loop

%plot normal distance to each measured point
figure(2)
for ii=1:meas_N

```

```

    if ori_meas_theta(ii)>360
        ori_meas_theta(ii)=ori_meas_theta(ii)-360;
    end
    plot(ori_meas_theta(ii),error_xy(ii),'.')
    hold on
end
topline=strcat(side , ' Normal distance from measured point to
polynomial: Speed= ',num2str(speed), 'mm/s and COF=
',num2str(cof), 'Hz');
    title({topline;file})
    xlabel('angle (degrees)')
    ylabel('Normal distance (mm)')
    hold off

% for i=1:length(error_xy)
%     if error_xy(i)>.001
%         i
%     end
% end

%plot histogram off all data
figure(3)
hist(error_xy,250)
[H,bin_center]=hist(error_xy,250);
[sorted_bins,bin_key]=sort(H, 'descend');
total_bias=bin_center(bin_key(1)) %mm
total_st_dev=std(error_xy,1) %mm
topline=strcat(' Histogram of error between ',side,' calibrated and
scanned data: Speed= ',num2str(speed), 'mm/s and COF=
',num2str(cof), 'Hz');
title({topline;file})
xlabel('error (mm)')
ylabel('number of points')
hold off

%Plot circle with errors greater than x plotted in red
figure(4)
error_divider=.0092;
for i=1:length(error_xy)
    if (error_xy(i) > error_divider)
        plot(meas_x(i),meas_y(i), 'r. ');hold on;
    else
        plot(meas_x(i),meas_y(i), 'k. ');hold on;
    end
end

end
topline=strcat(side , ' Location of errors
over',num2str(error_divider), ' mm for Speed=' ,num2str(speed), 'mm/s
and COF= ',num2str(cof), 'Hz');
title({topline;file})
xlabel('x (mm)')
ylabel('y (mm)')

```

```

%plot(cal_x,cal_y,'b. ');hold on;
hold off;

%unc calculation
k=2;
cal_unc=.000382; %mm
U=k*sqrt(cal_unc^2+total_st_dev^2)+abs(total_bias) %mm

%%%%%%%%%%%%%%%%%%%%%%%%%%%%%%%%%%%%%%%%%%%%%%%%%%%%%%%%%%%%%%%%%%%%%%%%
%unc bands
%theta dividers that divide waveform into bands based on wavelengths
%Band 1 (2+mm): 0-20, 160-180, 180-200, 340-360
%Band 2 (1-2mm): 20-40, 140-160, 200-220, 320-340
%Band 3 (.75-1mm): 40-60, 120-140, 220-240, 300-320
%Band 4 (.5-.75mm): 60-120, 240-300

bb1 = [0 20 160 180 180 200 340 360];
bb2 = [20 40 240 160 200 220 320 340];
bb3 = [40 60 120 140 220 240 300 320];
bb4 = [60 120 240 300];

%parse errors into correct uncertainty band by angle=wavelength
error1=0;
error2=0;
error3=0;
error4=0;

bloop=1; %band 1
for bi = 1:2:length(bb1)-1
    for ii = 1:meas_N
        if (bb1(bi)<=ori_meas_theta(ii)) &&
(ori_meas_theta(ii)<bb1(bi+1))
            error1=[error1 error_xy(ii)];
        end
    end
end
error1=error1(2:length(error1));
st_dev(bloop)=std(error1,1); %mm
[H,bin_center]=hist(error1,50);
[sorted_bins,bin_key]=sort(H, 'descend');
bias(bloop)=bin_center(bin_key(1)); %mm
Unc(bloop)=k*sqrt(cal_unc^2+st_dev(bloop)^2)+abs(bias(bloop));
bloop=2; %band 2
for bi = 1:2:length(bb2)-1
    for ii = 1:meas_N
        if (bb2(bi)<=ori_meas_theta(ii)) &&
(ori_meas_theta(ii)<bb2(bi+1))
            error2=[error2 error_xy(ii)];
        end
    end
end
end
end

```

```

error2=error2(2:length(error2));
st_dev(bloop)=std(error2,1); %mm
[H,bin_center]=hist(error2,50);
[sorted_bins,bin_key]=sort(H,'descend');
bias(bloop)=bin_center(bin_key(1)); %mm
Unc(bloop)=k*sqrt(cal_unc^2+st_dev(bloop)^2)+abs(bias(bloop));
bloop=3;%band 3
for bi = 1:2:length(bb3)-1
    for ii = 1:meas_N
        if (bb3(bi)<=ori_meas_theta(ii)) &&
(ori_meas_theta(ii)<bb3(bi+1))
            error3=[error3 error_xy(ii)];
        end
    end
end
error3=error3(2:length(error3));
st_dev(bloop)=std(error3,1); %mm
[H,bin_center]=hist(error3,50);
[sorted_bins,bin_key]=sort(H,'descend');
bias(bloop)=bin_center(bin_key(1)); %mm
Unc(bloop)=k*sqrt(cal_unc^2+st_dev(bloop)^2)+abs(bias(bloop));
bloop=4;%band 4
for bi = 1:2:length(bb4)-1
    for ii = 1:meas_N
        if (bb4(bi)<=ori_meas_theta(ii)) &&
(ori_meas_theta(ii)<bb4(bi+1))
            error4=[error4 error_xy(ii)];
        end
    end
end
error4=error4(2:length(error4));
st_dev(bloop)=std(error4,1); %mm
[H,bin_center]=hist(error4,50);
[sorted_bins,bin_key]=sort(H,'descend');
bias(bloop)=bin_center(bin_key(1)); %mm
% including bias
Unc(bloop)=k*sqrt(cal_unc^2+st_dev(bloop)^2)+abs(bias(bloop));

%plot unc bands
figure(5)
uncx=[6 2 1 .75 .5];
for j=1:1:length(uncx)-1
    x=[uncx(j) uncx(j+1)];
    y=[Unc(j) Unc(j)];
    plot(x,y)
    hold on
end
topline=strcat(side , ' Unc bands versus wavelength: Speed=
',num2str(speed) , ' mm/s and COF= ',num2str(cof) , 'Hz');
    title({topline;file})
    xlabel('wavelength (mm)')
    ylabel('Uncertainty (mm)')
hold off
%%%%%%%%%%%%%%%%%%%%%%%%%%%%%%%%%%%%%%%%%%%%%%%%%%%%%%%%%%%%%%%%%%%%%%%%
%save data to file

```

```
%savepath=strcat('c:\MATLAB701\work\ring\',file,'_ITCONT.txt'); %work
savepath=strcat('C:\Program
Files\MATLAB_SV71\work\ring\',file,'_processed.txt'); %home
fid = fopen(savepath,'wt');
fprintf(fid,'%f %f %2.8f\n',[ori_meas_theta;scaled_meas_r;error_xy]);
fclose(fid);
end_time=clock
```

```
%Note unc_plot2.m was used to calculate uncertainties without biases
%and plot those uncertainty bands in 2-D and 3-D
```

Vita

Pamela Murray Moor was born in 1978 in Knoxville, Tennessee. She attended The University of Tennessee and received her Bachelor's degree in Mechanical Engineering summa cum laude in May 2000 and her Master's degree in December 2001. During her undergraduate years she worked at Atom Sciences, Oak Ridge National Laboratory, and Woods Hole Oceanographic Institution. Her master's work was focused in robotics, dynamics, and controls. She received a National Science Foundation Graduate Research Fellowship and has focused her doctoral research on dimensional metrology. She is currently employed as a technical project manager at the Y-12 National Security Complex.